CHARGE CARRIER DYNAMICS OF LEAD HALIDE PEROVSKITES PROBED WITH ULTRAFAST SPECTROSCOPY

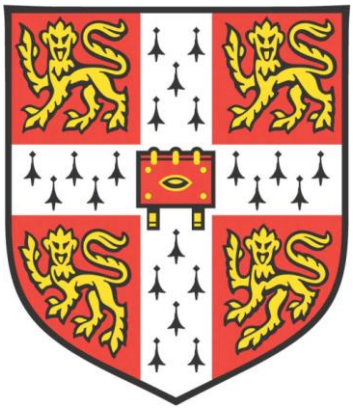

Jasmine P. H. Rivett

Churchill College

University of Cambridge

This dissertation is submitted for the degree of

Doctor of Philosophy

December 2017

CHARGE CARRIER DYNAMICS OF LEAD HALIDE PEROVSKITES PROBED WITH ULTRAFAST SPECTROSCOPY

In this thesis, we investigate the nature of charge carrier generation, relaxation and recombination in a range of lead halide perovskites. We focus on understanding whether the photophysical behaviour of these perovskite materials is like that of highly-ordered inorganic crystalline semiconductors (exhibiting ballistic charge transport) or disordered molecular semiconductors (exhibiting strong electron-phonon coupling and highly localised excited states) and how we can tune these photophysical properties with inorganic and organic additives. We find that the fundamental photophysical properties of lead halide perovskites, such as charge carrier relaxation and recombination, arise from the lead halide lattice rather than the choice of A-site cation. We show that while the choice of A-site cation does not affect these photophysical properties directly, it can have a significant impact on the structure of the lead halide lattice and therefore affect these photophysical properties indirectly. We demonstrate that lead halide perovskites fabricated from particular inorganic and organic A-site cation combinations exhibit low parasitic trap densities and enhanced carrier interactions. Furthering our understanding of how the photophysical properties of these materials can be controlled through chemical composition is extremely important for the future design of highly efficient solar cells and light emitting diodes.

Jasmine P. H. Rivett

For my friends and family

It is impossible to live without failing at something, unless you live so cautiously that you might as well not have lived at all - in which case, you fail by default.

J.K. Rowling

DECLARATION

This dissertation is the result of my own work and includes nothing which is the outcome of work done in collaboration except as specified in the text. It is not substantially the same as any that I have submitted, or, is being concurrently submitted for a degree or diploma or other qualification at the University of Cambridge or any other University or similar institution except as specified in the text. I further state that no substantial part of my dissertation has already been submitted, or, is being concurrently submitted for any such degree, diploma or other qualification at the University of Cambridge or any other University or similar institution except as specified in the text. This thesis is does not exceed 60000 words.

ACKNOWLEDGEMENTS

I am extremely grateful to the huge number of people who have made my PhD such an interesting journey.

I am particularly thankful to Dan Credgington, for taking me on as his first student and providing continual support, advice and time throughout my PhD. I am extremely thankful to Felix Deschler for the 'quick and simple' measurement ideas, which have kept me occupied during my entire PhD. I am very thankful to Richard Friend, Henning Sirringhaus, Neil Greenham, Erika Eiser, Artem Bakulin, Akshay Rao and Siân Dutton for scientific advice and guidance. I am very grateful to Alex Crook, Richard Gymer, Roger Beadle, Alison Barker, Gilly Walker, Zina Maneikiene and the Kapitza Hub staff for their support.

I am hugely grateful to Andreas Jakowetz, Nick Paul and Andrew Musser for teaching me how to align a NOPA during the day and night on weekdays and weekends; without this knowledge I would have not collected any of the data in this thesis. I am very grateful to Michael Price for helping me understand the photophysics of lead halide perovskites, even when he was writing up his thesis; I did not understand what this meant at the time, but I do now. I am grateful to my co-workers Tudor Thomas, Alexander Gillett, Vincent Kim, Karl Gödel, Marcus Böhm, Giorgio Divitini, Edward Booker, Nathaniel Davis and Tim Van De Goor. I am thankful to Matt Menke and Ture Hinrichsen for very helpful and interesting coding discussions.

I am very grateful to the Armourers & Brasiers Gauntlet Trust, Cambridge Philosophical Society, the Institute of Physics and Churchill College for the travel grants that have enabled me to present my work all over the world.

I am very grateful to Kayla Friedman and Malcolm Morgan of the Centre for Sustainable Development, University of Cambridge, UK for producing the Microsoft Word thesis template used to produce this document. It has worked fantastically. I highly recommend this template, and Microsoft Word in general, to anyone who wants to write a thesis that will not have a compiling error that you cannot seem to fix no matter how hard you try on the day of your deadline.

I am very thankful to the NanoDTC for funding and support. I am thankful to Tom and Luis for encouraging me to join OE and everyone from the cohort of 2013 – Chess,

Paul, Jean, Matt, Alex, Rox, Hadi, Carmen, Greg, Ed, Rozi and Julian – for a fantastically fun first year and continued support over the past few years.

I am thankful to Jane in the CAPE café for the friendly conversations, restaurant recommendations and for always making me smile.

I am very grateful to the women in OE – Leah, Arya, Lissa, Hope, Angela, Heather, Zhongyang, Bodan, Chloe, Elsa, Xinyu, Shrui, Mejd, Zahra, Darshana, Arfa, May Ling, Limeng, Sarah, Chanakarn, Camille and Olga – for their continual support and encouragement.

I am very thankful to Hannah and Jesse for the extremely fun and friendly welcome to New Zealand.

I am extremely thankful to Saul for always supporting me with cups of tea and food, as well as for the multiple times he has helped me by driving me around in his car.

I am extremely grateful to Latika and Alex for their constant support, for making me laugh, for listening to me even when I am complaining, for motivating me and convincing me that everything is going to be okay, for being amazing travel companions, dinner hosts and guests, and escape room experts.

I am very grateful to Josh and the Bailey family for all their love and support through some of the most difficult times in my life.

I am very thankful to Madeline, Sam and Adam, who I know I can always call when I am feeling down.

I am very grateful to Johannes for always lifting me up when I am down, for always giving me something to look forward to, and for always reminding me what is important in life. I would not have finished this thesis on time if I had not been so excited about our plans for the future.

I am extremely thankful to my family – in particular my mum, sisters and grandparents – for your continued support and insistence that physics is not the most important thing in the universe. Dad, I did it! I wish you were still here to see me finish this, I hope you would be proud.

CONTENTS

1 INTRODUCTION 17

2 BACKGROUND 20

2.1 Lead halide perovskites 20

2.1.1 Chemical composition of lead halide perovskites 20

2.1.2 Mixed lead halide perovskites 22

2.1.3 Two-dimensional, one-dimensional and zero-dimensional lead halide perovskites 24

2.1.4 Commercialisation of lead halide perovskites 26

2.2 Properties of semiconductors 28

2.2.1 Origin of the bandgap 28

2.2.2 Interaction of semiconductors with light 32

2.2.2.1 Refraction 34

2.2.2.2 Scattering 34

2.2.2.3 Absorption 34

2.2.2.3.1 Decoherence regime (first few tens of femtoseconds) 36

2.2.2.3.2 Thermalisation regime (~0-500 fs) 36

2.2.2.3.3 Cooling regime (~0.2-500 ps) 37

2.2.2.3.4 Recombination regime (> 1 ps) 38

2.2.2.4 Luminescence 45

2.2.3 Interaction of semiconductors with linearly polarised light 47

2.2.3.1 Intrinsic anisotropy 47

2.2.3.2 Induced anisotropy 52

2.3 Solar cells and light-emitting diodes 55

2.3.1 Internal quantum efficiency (IQE) 56

2.3.2 Incoupling and outcoupling efficiencies 56

2.3.3 External quantum efficiency (EQE) 56

2.3.4 Power conversion efficiency (PCE) 58

3 EXPERIMENTAL METHOD 59

3.1 Materials studied 59

3.1.1 Standard lead halide perovskite films 59

3.1.1.1 $CH_3NH_3PbI_3$ and $CH_3NH_3PbBr_3$ bulk films 60

3.1.1.2 $CsPbI_3$ and $CsPbBr_3$ nanocrystal films 60

3.1.2 Mixed cation lead halide perovskites 60
3.1.3 Additive-controlled lead halide perovskites 62
3.2 Steady state material characterisation techniques 63
3.2.1 Scanning electron microscopy (SEM) 63
3.2.1.1 Principles 63
3.2.1.2 Procedure 63
3.2.2 Raman spectroscopy 63
3.2.2.1 Principles 64
3.2.2.2 Procedure 65
3.2.3 X-ray diffraction (XRD) 65
3.2.3.1 Principles 65
3.2.3.2 Procedure 68
3.2.4 Steady-state absorption spectroscopy 68
3.2.4.1 Principles 68
3.2.4.2 Standard procedure 69
3.2.4.3 Linear polarisation selective procedure 69
3.2.5 Photoluminescence quantum efficiency (PLQE) 69
3.2.5.1 Principles 69
3.2.5.2 Procedure 72
3.3 Transient characterisation techniques 72
3.3.1 Sample encapsulation 72
3.3.2 Transient photoluminescence (TPL) spectroscopy 73
3.3.2.1 Time-correlated single photon counting (TCSPC) 73
3.3.2.1.1 Principles 73
3.3.2.1.2 Procedure 74
3.3.2.2 Intensified charge-coupled device (ICCD) 75
3.3.2.2.1 Principles 75
3.3.2.2.2 Procedure 75
3.3.3 Transient absorption (TA) spectroscopy 76
3.3.3.1 Principles 76
3.3.3.2 Procedure 79
4 POLARISATION ANISOTROPY IN LEAD HALIDE PEROVSKITES 83
4.1 Background and motivation 84

4.2 Preparation of lead halide perovskite films 85
4.3 Linear polarisation selective steady-state absorption of lead halide perovskite films 87
4.4 Linear polarisation selective transient absorption (LPTA) of lead halide perovskite films 88
4.4.1 Femtosecond LPTA of lead halide perovskite films 89
4.4.2 Picosecond LPTA of lead halide perovskite films 92
4.4.3 Effect of crystallite size and crystallite packing on the polarisation anisotropy 95
4.4.4 Effect of pump energy on the polarisation anisotropy 100
4.4.5 Effect of excitation density on the polarisation anisotropy 104
4.4.6 First principles calculations of the polarisation anisotropy 106
4.5 Conclusions and future work 111
5 RECOMBINATION IN MIXED CATION LEAD HALIDE PEROVSKITES. 114
5.1 Background and Motivation 115
5.2 Preparation of mixed cation perovskites 116
5.3 Steady-state absorption of mixed cation perovskites 120
5.4 Photoluminescence quantum efficiency (PLQE) of mixed cation perovskites 121
5.5 Transient photoluminescence (TPL) of mixed cation perovskites 123
5.6 Transient absorption (TA) of mixed cation perovskites 130
5.7 X-ray diffraction (XRD) of mixed cation perovskites 138
5.8 Raman spectroscopy of mixed cation perovskites 140
5.9 Conclusions and future work 142
6 RECOMBINATION IN ADDITIVE-CONTROLLED LEAD HALIDE PEROVSKITES 144
6.1 Background and motivation 145
6.2 Preparation of additive-controlled perovskites 151
6.3 Steady-state absorption and steady-state photoluminescence of additive-controlled perovskites 151
6.4 Photoluminescence quantum efficiency (PLQE) of additive-controlled perovskites 153
6.5 Transient photoluminescence (TPL) of additive-controlled perovskites 155
6.6 Transient absorption (TA) of additive-controlled perovskites 161
6.7 Scanning electron microscopy (SEM), atomic force microscopy (AFM) and grazing incidence x-ray diffraction (GIXRD) of additive-controlled perovskites 168

6.8 Conclusions and future work 171
7 CONCLUSIONS AND FUTURE WORK 172

LIST OF TABLES

Table 3.1 Table of the abbreviations used in this thesis and the corresponding chemical formulae.. 61

Table 5.1 Table of the PLQEs of the mixed cation perovskite samples. 122

Table 5.2 Table of the first, second and third-order recombination rates extracted from TA and TPL measurements.....135

Table 6.1 Table of the highest efficiency perovskite LEDs reported in the literature since 2014, adapted from reference 8. 147

Table 6.2 Table of the PLQEs of the additive-controlled perovskites. 154

Table 6.3 Table of the first, second and third-order recombination rates extracted from TA and TPL measurements.....166

Table 6.4 Table of the average grain size of the additive-controlled perovskite samples. 170

LIST OF FIGURES

Figure 2.1 Diagram of tolerance factor and effective radius for mixtures of $CsPbI_3$ and $(NH_2)_2CHPbI_3$, taken from reference 56. 23

Figure 2.2 Diagram of a three-dimensional perovskite lattice being transformed into a two-dimensional Ruddlesden-Popper type perovskite lattice upon the addition of butylammonium cations, taken from reference 65. 25

Figure 2.3 Diagram demonstrating band formation in semiconductors, taken from reference 121. 30

Figure 2.4 Diagram demonstrating band formation in typical inorganic semiconductors such as Ge and GaAs, taken from reference 122. 31

Figure 2.5 Diagram of a direct and indirect semiconductor bandgap, taken from reference 122. 32

Figure 2.6 Summary of general linear optical processes, adapted from reference 122. . 33

Figure 2.7 Diagram of charge carrier interactions in semiconducting bulk materials and semiconducting nanomaterials. 40

Figure 2.8 Recombination rate as a function of photoexcitation density (A) and TA signal as a function of time (B) for $CH_3NH_3PbI_3$ films, both taken from reference 152. 44

Figure 2.9 Intrinsic anisotropy in wurtzite GaN, taken from reference 172. 49

Figure 2.10 Linear polarisation selective transient absorption measurements on aligned silicon nanowires and single-walled carbon nanotubes, taken from references 181 and 182 respectively. 51

Figure 2.11 Momentum distribution functions of electrons photoexcited with linearly polarised light. 54

Figure 3.1 Diagram of the elastic Rayleigh scattering and the inelastic Raman scattering processes (Stokes and anti-Stokes) taken from reference 218. 64

Figure 3.2 Diagram demonstrating Bragg's law taken from reference 221. 67

Figure 3.3 (A) Diagram of the measurements required to calculate the PLQE of a sample using the integrating-sphere method. (B) Example laser spectrum and PL

spectrum obtained from the measurements shown in (A). Both taken from reference 164. 71

Figure 3.4 Diagram of TCSPC, taken from reference 226. 74

Figure 3.5 Diagram of the ICCD setup. 75

Figure 3.6 Diagram of a typical transient absorption (TA) setup. 76

Figure 3.7 Normalised change in transmission as a function of probe wavelength and time after photoexcitation for a standard $CH_3NH_3PbI_3$ perovskite sample. 78

Figure 3.8 Diagram of a non-collinear optical parametric amplifier (NOPA), taken from reference 236, and a schematic of optical parametric amplification, taken from reference 231. 80

Figure 4.1 Scanning electron microscopy (SEM) images of standard lead halide perovskites. 86

Figure 4.2 Linear polarisation selective steady-state absorption of standard perovskite films. 87

Figure 4.3 Diagram of the linear polarisation selective transient absorption (LPTA) setup. 88

Figure 4.4 LPTA spectra for a $CH_3NH_3PbI_3$ bulk film within the first 200 fs after photoexcitation. 90

Figure 4.5 LPTA spectra for a $CH_3NH_3PbI_3$ bulk film and a $CsPbI_3$ nanocrystal film between 1-10 ps after photoexcitation. 92

Figure 4.6 LPTA anisotropy maps for a $CH_3NH_3PbI_3$ bulk film and a $CsPbI_3$ nanocrystal film within the first 10 ps after photoexcitation. 94

Figure 4.7 LPTA and population kinetics of standard lead halide perovskites. 97

Figure 4.8 LPTA maps of standard lead halide perovskites. 98

Figure 4.9 LPTA of a $CH_3NH_3PbI_3$ bulk film. 99

Figure 4.10 Pump energy dependent average anisotropy for all standard lead halide perovskites. 101

Figure 4.11 Pump energy dependent anisotropy kinetics for all standard lead halide perovskite samples. 103

Figure 4.12 Effect of excitation density on the anisotropy. 105

Figure 4.13 First-principles calculation of the transition dipole moments (TDMs) of $CH_3NH_3PbI_3$. 107

Figure 4.14 LPTA spectra and modelled spectra of $CH_3NH_3PbI_3$. 109

Figure 5.1 Tolerance factors of $APbI_3$ perovskites (where A is either Li, Na, K, Rb, Cs, methylammonium or formamidinium) and corresponding images of the films formed, both taken from reference 58. 117

Figure 5.2 X-ray diffraction (XRD) spectra of $RbPbI_3$, and RbCsMAFAPbIBr perovskite with varying Rb percentage x, taken from reference 58. 118

Figure 5.3 Scanning electron microscopy (SEM) images of RbCsMAFAPbIBr perovskites, taken from reference 58. 119

Figure 5.4 Steady-state absorption spectra of mixed cation perovskite samples. 120

Figure 5.5 Transient photoluminescence (TPL) spectra of mixed cation perovskite samples. 123

Figure 5.6 Transient photoluminescence (TPL) kinetics of mixed cation perovskite samples. 125

Figure 5.7 Estimated lifetimes of mixed cation perovskite samples from TPL measurements. 127

Figure 5.8 Initial TPL signal (PL_0) plotted against excitation density n for the mixed cation perovskite samples. 129

Figure 5.9 Transient absorption (TA) spectra and kinetics of mixed cation perovskite samples. 130

Figure 5.10 Recombination rate plotted against carrier density for all mixed cation perovskite samples. 132

Figure 5.11 Fits of log(recombination rate) plotted against log(carrier density) for all mixed cation perovskite samples. 134

Figure 5.12 Carrier cooling in mixed cation perovskite samples. 137

Figure 5.13 X-ray diffraction (XRD) of mixed cation perovskites samples. 139

Figure 5.14 Resonant-Raman spectra of mixed cation perovskites. 141

Figure 6.1 Additive-controlled lead halide perovskite LEDs, taken from reference 8. 148

Figure 6.2 Diagrams demonstrating how dimensional modulation of the lead halide perovskite lattice can alter the energy landscape and result in efficiency energy funnelling, all taken from reference 74. 150

Figure 6.3 Steady-state absorption and photoluminescence of $CsPbBr_3$ with PEABr and -O-C-O- additives, taken from reference 8. 152

Figure 6.4 Transient photoluminescence (TPL) spectra and kinetics of additive-controlled perovskite samples. 156

Figure 6.5 Transient photoluminescence (TPL) kinetics of additive-controlled perovskite samples. 157

Figure 6.6 Initial TPL signal (PL_0) plotted against excitation density (n) for the additive-controlled perovskite samples. 159

Figure 6.7 Initial TPL signal (PL_0) plotted against excitation density (n) for a film of $CsPbI_3$ nanocrystals. 160

Figure 6.8 Transient absorption (TA) spectra and kinetics of additive-controlled perovskite samples. 162

Figure 6.9 Recombination rate plotted against carrier density for all additive-controlled perovskite samples. 164

Figure 6.10 Fits of log(recombination rate) plotted against log(carrier density) for all additive-controlled perovskite samples. 165

Figure 6.11 Fits of log(recombination rate) plotted against log(carrier density) for all additive-controlled perovskite samples. 167

Figure 6.12 Structural characterisation of additive-controlled perovskites. 169

LIST OF ABBREVIATIONS AND ACRONYMS

DFT	Density functional theory
EQE	External quantum efficiency
FWHM	Full width half maximum
GIXRD	Grazing incidence x-ray diffraction
GSB	Ground state bleach
IQE	Internal quantum efficiency
NIR	Near infrared
PCE	Power conversion efficiency
PEA	Phenethylamine
PEABr	Phenethylamine bromide
SE	Stimulated emission
TA	Transient absorption
TDM	Transition dipole moment
TIR	Total internal reflection
TPL	Transient photoluminescence
XRD	X-Ray diffraction

1 Introduction

Despite the sun supplying enough energy every hour to meet global electricity needs for an entire year, only around 0.1% of worldwide demand is currently met by solar power[1]. Furthermore, more than 15% of this global electricity consumption is used for lighting[2]. This means that there is a huge opportunity to reduce worldwide greenhouse gas emissions and improve global air quality, as well as to help the 1.2 billion people who do not have access to modern energy services and therefore use hazardous energy sources such as kerosene[2], by developing efficient and low-cost distributable solar cells and light-emitting diodes.

Since the discovery of the photovoltaic effect by Alexandre Edmond Becquerel in 1839[3] and electroluminescence by Henry Joseph Round in 1907[4], a number of solar cell and light-emitting diode technologies have been developed, based on both organic and inorganic semiconducting materials.

In 2009, the first 'hybrid' methylammonium lead iodide perovskite solar cell was reported[5], with a power conversion efficiency of 3.8%. Now, less than ten years later, methylammonium lead iodide perovskite solar cells with power conversion efficiencies of over 22% have been reported[6], making lead halide perovskite the fastest advancing solar cell technology to date. Following this success, the first methylammonium lead iodide perovskite light emitting diode, with an external quantum efficiency of 0.76%, was reported in 2014[7]. Now, less than five years later, lead halide perovskite light-emitting diodes with external quantum efficiencies of over 15% have been reported[8].

As well as being used to fabricate highly efficient solar cells and light-emitting diodes, lead halide perovskites have also successfully been used in a number of other different optoelectronic devices including optically pumped lasers[9–12], transistors[13], water splitting cells[14], and photodetectors[15,16]. However, the fundamental photophysical properties of these materials are still not completely understood. Since a better understanding of these properties could lead to the development of optoelectronic devices with even higher efficiencies, these properties are the focus of this thesis.

In Chapter 2, we summarise the key theoretical concepts underlying our experimental results. In Chapter 3, we describe the experimental techniques used to obtain these experimental results.

In Chapter 4, we demonstrate how linear polarisation selective transient absorption measurements reveal the dynamic nature of the photoexcited electronic states in lead halide perovskites. We show that in general, lead halide perovskites are truly hybrid in nature, with photophysical properties different to those observed in traditional purely organic and inorganic semiconductors.

In Chapter 5, we demonstrate how a combination of transient absorption spectroscopy and transient photoluminescence spectroscopy measurements reveal that these photophysical properties may be tuned by incorporating a mixture of ions, such as formamidinium, caesium and rubidium into standard methylammonium lead halide perovskites. We show that this tuning leads to a reduction in undesirable non-radiative recombination pathways and therefore an enhancement in the performance of lead halide perovskite solar cells.

In Chapter 6, we demonstrate how a combination of transient absorption spectroscopy and transient photoluminescence spectroscopy measurements reveal that these photophysical properties may also be tuned by incorporating organic molecular additives into standard caesium lead halide perovskites. We show that this tuning modulates the dimensionality of the lattice, which leads to a reduction in undesirable non-radiative recombination pathways and therefore an enhancement in the performance of lead halide perovskite light-emitting diodes.

Finally, in Chapter 7, we review the key results presented in Chapters 4, 5 and 6 and briefly discuss potential future research directions. According to the chief executive officer of Oxford Photovoltaics, Frank Averdung[17], “Perovskite has the potential to

radically improve the efficiency of solar photovoltaics and meet the world's energy demand into the future". We hope that our results will contribute to the development of these highly efficient lead halide perovskite optoelectronic devices and bring them closer to meeting their future potential.

2 Background

In this chapter, we introduce the key concepts underlying the data presented in this thesis. This includes an introduction to lead halide perovskites, an overview of the electronic and photophysical properties of semiconductors and a discussion of how semiconducting materials may be used to fabricate highly efficient solar cells and light emitting diodes.

2.1 Lead halide perovskites

In this section, we introduce the lead halide perovskite crystal structure, discuss how the properties of lead halide perovskites may be tuned by varying chemical composition and review the key properties of lead halide perovskites.

2.1.1 Chemical composition of lead halide perovskites

Perovskites are a class of compounds which have the same crystal structure as $CaTiO_3$, a cubic crystal structure with the general formula ABX_3. They were studied in detail by Victor Goldschmidt in 1926[18], who calculated that stable perovskite crystal structures can only be formed from combinations of elements with particular sizes. The Goldschmidt tolerance factor (t_f) is a dimensionless number which is calculated using Equation 2.1 from the ionic radii of the A cations (r_A), B cations (r_B) and the X anions (r_X) used to form a compound.

$$t_f = \frac{(r_A + r_X)}{\sqrt{2}\,(r_B + r_X)} \qquad 2.1$$

While it is difficult to accurately determine the exact ionic radii, particularly for organic cations with non-spherical geometries that constantly rotate inside the crystal lattice, tolerance factor calculations may be used to predict whether stable perovskite crystal structures are likely to be formed. Typically, a stable, three-dimensional perovskite crystal structure is only formed when the tolerance factor is between 0.8 and 1. However, even with this limitation, the range in tolerance factor means that a number of different atomic and molecular combinations crystallise into stable, three-dimensional perovskite crystal structures. Therefore, depending on their composition, perovskites may be insulating[19], semiconducting[20] or metallic[21] and exhibit a range of interesting physical and magnetic properties, such as ferroelectricity, insulator-to-metal transitions, ferromagnetism, and superconductivity[22].

Lead halide perovskites are a class of compounds with general formula ABX_3, where typically A is methylammonium CH_3NH_3, formamidinium $(NH_2)_2CH$ or Cs, B is Pb and X is I, Br or Cl. They were first studied in 1893[23] and are semiconducting materials which are used in a number of different optoelectronic devices[24,25], including solar cells[5,6], light-emitting diodes[7,8], optically pumped lasers[9–12], tranisitors[13], water splitting cells[14], and photodetectors[15,16].

The excellent optoelectronic performance of lead halide perovskites arise from their large absorption coefficients[26], low Urbach energies that indicate low disorder and high crystallinity[27], low exciton (bound electron-hole pair[28,29]) binding energies that lead to the generation of free charge carriers at room temperature[30,31], high charge carrier mobilities and lifetimes[32], long carrier diffusion lengths[33,34] slow bimolecular charge recombination rates[9], low amplified spontaneous emission thresholds and the fact that they support photon recyling[35]. Lead halide perovskites also exhibit ferroelasticity[36], giant photostriction[37], piezoelectricity[38] and potentially ferroelectricity[39], although this is heavily debated[40,41]. It has also been suggested that the dynamic disorder[42–44] of the lead halide lattice, potentially arising from rotation of the organic A-site cation[45–47], may lead to a dynamic indirect bandgap with giant Rashba spin-orbit coupling[48–52] that hinders charge carrier recombination and enhances charge carrier lifetime[53].

In addition to having these interesting properties, lead halide perovskites are also solution-processable at room-temperature and are highly tuneable[54,55]. The range of possible tolerance factors mean that lead halide perovskites may be composed from a range of cations and anions. This means that the optical bandgap of these materials may be tuned to better match the solar spectrum – for example by shifting the bandgap from ~1.6 eV to ~1.5 eV by replacing methylammonium cations with larger formamidinium cations[56] – or to change their colour of emission – for example by shifting the bandgap from near-infrared to green by replacing iodide anions with bromide anions[7].

2.1.2 Mixed lead halide perovskites

The properties of lead halide perovskites may also be tuned further by using a mixture of cations and anions, which may or may not form stable three-dimensional perovskites when used individually. For example, $CsPbI_3$ and $(NH_2)_2CHPbI_3$ do not exist in stable perovskite structures at room temperature, because the Goldschmidt tolerance factor of $CsPbI_3$ is slightly below 0.8 and the Goldschmidt tolerance factor of $(NH_2)_2CHPbI_3$ is slightly above 1. However, when Cs and $(NH_2)_2CH$ are combined, such as in a material with a composition of $(NH_2)_2CH_{0.85}Cs_{0.15}PbI_3$, a stable perovskite phase is formed at room temperature, as shown in Figure 2.1[57,58]. Therefore, using mixtures of cations such as rubidium, caesium, methylammonium and formamidinium[57–62] or mixtures of anions such as iodide and bromide[63–65] can significantly improve the performance and stability of lead halide perovskite optoelectronic devices.

Image removed for copyright reasons.

Figure 2.1 Diagram of tolerance factor and effective radius for mixtures of $CsPbI_3$ and $(NH_2)_2CHPbI_3$, taken from reference 57. *Since $CsPbI_3$ has a tolerance factor slightly below 0.8, it exists in a yellow orthorhombic phase (δ_O-$CsPbI_3$) at room temperature. Since $(NH_2)_2CHPbI_3$ has a tolerance factor slightly above one, it exists in a yellow hexagonal phase (δ_H-$FAPbI_3$) at room temperature. By combining Cs and $(NH_2)_2CH$, the effective tolerance factor may be tuned and stable black perovskite phases may be formed.*

2.1.3 Two-dimensional, one-dimensional and zero-dimensional lead halide perovskites

The properties of lead halide perovskites may also be tuned further by modulating the dimensionality of the crystal lattice with bulky organic molecules. For example, when butylammonium cations are incorporated into standard three-dimensional methylammonium lead iodide perovskites, two-dimensional Ruddlesden-Popper perovskites are formed[66]. These perovskites consist of well-defined methylammonium lead iodide layers separated by organic butylammonium layers and have the chemical formula $(CH_3(CH_2)_3NH_3)_2(CH_3NH_3)_{n-1}Pb_nI_{3n+1}$, where n is equal to the number of layers in the methylammonium lead iodide stack[66].

The general formula of Ruddlesden-Popper perovskites is $A_{n-1}A'_2B_nX_{3n+1}$, where A, A', and B are cations, X is an anion and n is the number of octahedral layers in the well-defined perovskite stacks[67]. As with three-dimensional perovskites, two-dimensional Ruddlesden-Popper perovskites may be formed from a variety of different organic and inorganic cations and anions[66,68–72]. However, in contrast to three-dimensional perovskites, two-dimensional Ruddlesden-Popper perovskites are natural quantum wells with large exciton binding energies[67] and are relatively stable[73]. In lead halide perovskites composed of a variety of Ruddlesden-Popper phases with different numbers of layers in the well-defined perovskite stacks, it has been shown that these natural quantum wells efficiently funnel and concentrate charge carriers into localised low energy states, resulting in increased radiative recombination and enhanced light-emitting diode performance[74–77]. It is also possible to synthesise lead halide perovskite phases consisting of one-dimensional networks of octahedra separated by organic regions[78] or zero-dimensional polyhedra surrounded by organic regions[79,80]. Isolated colloidal ABX_3 lead halide perovskite quasi-two-dimensional nanoplatelets[81–83], quasi-one-dimensional nanowires[10,84–86] and quasi-zero-dimensional nanocrystals[87–91], have also been fabricated by controlling the growth direction during synthesis.

Image removed for copyright reasons.

Figure 2.2 Diagram of a three-dimensional perovskite lattice being transformed into a two-dimensional Ruddlesden-Popper type perovskite lattice upon the addition of butylammonium cations, taken from reference 66. *On the left side is a three-dimensional perovskite lattice. On the right side are two-dimensional Ruddlesden-Popper type perovskite lattices, with the number of layers in the perovskite stack (n) equal to n = 4, n = 3, n = 2 and n = 1 respectively.*

2.1.4 Commercialisation of lead halide perovskites

Given the excellent photophysical properties of lead halide perovskites, combined with their simple room-temperature solution-processability, lead halide perovskite optoelectronic devices sound like perfect candidates for commercialisation. However, as well as significant issues with stability, one of the major hurdles facing the commercialisation of lead halide perovskite optoelectronic devices is the fact that they contain lead.

According to Directive 2002/95/EC of the European Union, the use of lead and cadmium is prohibited in electrical and electronic equipment put on the market after 1st July 2006[92]. Therefore, in order to successfully commercialise lead halide perovskite optoelectronic devices, either effective environmental protection and recycling procedures must be developed, or the lead must be replaced with a less harmful material.

Simple and sustainable waste disposal and recycling procedures for lead based perovskites are already being developed[93]. These procedures suggest that every layer in the solar cell could be removed individually. This would effectively isolate the toxic lead compounds so that they could be handled in a way that would not harm the environment. It would also mean that the extracted lead compounds could be processed and reused again in new perovskite solar cells, so that lead waste is reduced.

A number of lead-free alternatives to lead halide perovskites are also being developed[94]. Currently, tin is the most common substitute for lead in these materials[95–100], partly because the optical band gap of $CH_3NH_3SnI_3$ (1.3 eV) is closer to the optimal bandgap for solar cells proposed by Shockley and Queisser (1.34 eV) than the optical band gap of $CH_3NH_3PbI_3$ (1.6 eV)[101,102]. However, the major problem with using tin in these materials is that it irreversibly oxidises from Sn^{2+} cations to Sn^{4+} cations when it is exposed to air[103]. This oxidation causes $CH_3NH_3SnI_3$ to become self-doped and change from a semiconducting material into a conductive material, which significantly reduces device performance[104]. This is one reason why, the current record pure tin halide perovskite and mixed lead-tin perovskite solar cell power conversion efficiencies are only 9%[105] and 15%[95] respectively. This is significantly lower than the current record pure lead halide perovskite solar cell power conversion efficiency of 22.7%[6].

Recent studies have shown that the oxidation of tin halide perovskites occurs through a cooperative mechanism in which multiple adjacent Sn^{2+} ions form SnO_2 and SnI_4[106]. Therefore, supressing this process could enhance the stability of these materials. Substituting a small fraction of tin with lead has been shown to fundamentally change the oxidation mechanism of tin based perovskites and increase their stability more than would be expected from a simple reduction in the tin content. This is because there is a higher probability that Sn^{2+} ions will be adjacent to Pb^{2+} ions which have a higher tolerance to oxidation than Sn^{2+} ions[106]. It has also been shown that adding SnI_2 dimethyl sulfoxide complexes during the crystallisation process[107] or additives, such as $SnCl_2$[108] or SnF_2[109], to tin halide perovskites can enhance stability. Low-dimensional tin halide perovskites, such as phenylethylammonium formamidinium tin iodide are also generally more stable than three-dimensional tin halide perovskites[110,111].

Another problem with using tin in these materials is that, for different reasons, exposure to SnI_2 is more lethal than exposure to the same nominal concentration of PbI_2[112]. In addition, exposure to either lead or tin can cause impaired embryonic development[112,113]. Water soluble salts, such as those used in lead and tin halide perovskites, are particularly harmful as they are easily taken up by living organisms[93]. In fact, a daily dose of only 1 mg can result in chronic lead poisoning symptoms, such as birth defects, in humans[93]. Despite this, it has been suggested that only a negligibly small risk of heavy metal intoxication could arise from defective perovskite solar cells[112].

Other proposed substitutes for lead, which are less toxic and more stable, include germanium[114] and bismuth[115–118]. Computational studies have also identified a number of other potential combinations of less toxic and more stable elements that could form semiconducting perovskites[119].

In this section, we have discussed the semiconducting properties of lead halide perovskites. In the next section, we discuss the fundamental origin of these semiconducting properties.

2.2 Properties of semiconductors

According to the Oxford English Dictionary[120], a semiconductor is a "solid substance that has a conductivity between that of an insulator and that of most metals". This conductivity arises from free electrons in the conduction band. Therefore, since the probability of exciting an electron from the valence band to the conduction band is related to the energy gap between the top of the valence band and the bottom of the conduction band – known as the bandgap – the electrical conductivity of a solid is related to the bandgap. Semiconductors used in optoelectronic applications typically have bandgaps with energies corresponding to the ultraviolet, visible or infrared regions of the electromagnetic spectrum.

2.2.1 Origin of the bandgap

The complete Hamiltonian which fully describes a perfect crystal lattice has five terms, a sum of the kinetic energy of each electron, sum of the kinetic energy of each nucleus, sum of coulomb interaction between each pair of nuclei, sum of coulomb interaction between each pair of electrons and sum of coulomb interaction between each electron with each nucleus[121]. This many-particle Hamiltonian is currently too complicated to solve without many simplifications. Therefore, two approximations are generally made. First, the electrons are categorised as either valence electrons (in incompletely filled shells) or core electrons (in completely filled shells). All the core electrons surrounding a single nucleus and that corresponding nucleus can be considered to be a single entity called an ion core, since the core electrons are mainly localised around the nuclei, this greatly reduces the number of electrons which must be considered in the calculations[121]. The second approximation, called the Born-Oppenheimer or adiabatic approximation, states that the frequency of electronic motion (on order of 10^{15}s $^{-1}$) is much faster than ionic vibrations (typically less than 10^{13} s $^{-1}$). This is because the mass of the ions in the lattice are much heavier than the mass of the electrons in the lattice. Therefore, to a good approximation the ions are stationary relative to the electrons, and the ions are subject to only a time-averaged adiabatic electronic potential[121].

With these approximations the Hamiltonian is simplified to[121],

$$H = \sum H_{ions}(\boldsymbol{R}_j) + \sum H_e(\boldsymbol{r}_i, \boldsymbol{R}_{j0}) + \sum H_{e-ion}(\boldsymbol{r}_i, \delta\boldsymbol{R}_j) \qquad 2.2$$

where, $H_{ions}(\boldsymbol{R}_j)$ is the Hamiltonian for the ionic motion in the environment of the ionic potentials and time-averaged adiabatic electronic potentials, $H_e(\boldsymbol{r}_i, \boldsymbol{R}_{j0})$ is the Hamiltonian of the electrons in the environment of stationary ions in their equilibrium positions $\boldsymbol{R}_{j0}$, $H_{e-ion}(\boldsymbol{r}_i, \delta\boldsymbol{R}_j)$ is the Hamiltonian originating from the change in the electronic energy resulting from displacements $\delta\boldsymbol{R}_j$ of the ions from their equilibrium positions (electron-phonon interaction), $\boldsymbol{r}_i$ is the position of the ith valence electron and $\boldsymbol{R}_j$ is the position of the jth ion core. The terms involving ionic motion, $H_{ions}(\boldsymbol{R}_j)$ and $H_{e-ion}(\boldsymbol{r}_i, \delta\boldsymbol{R}_j)$, are important for the vibrational and electron-phonon interactions in semiconductors but the Hamiltonian describing the electronic motion, $H_e(\boldsymbol{r}_i, \boldsymbol{R}_{j0})$, is most important for band structure calculations.

The Hamiltonian $H_e(\boldsymbol{r}_i, \boldsymbol{R}_{j0})$ can be simplified further by using the mean-field approximation, in which it is assumed that every electron of mass m experiences the same average periodic potential $V(\boldsymbol{r})$ or the potential energy of every electron is an average potential $V(\boldsymbol{r})$ which has the same periodicity as the crystal lattice. In this case, every electron has the same equation of motion[122],

$$H_{1e}\psi_k(\boldsymbol{r}) = \left(\frac{p^2}{2m} + V(\boldsymbol{r})\right)\psi_k(\boldsymbol{r}) = E_k\psi_k(\boldsymbol{r}), \qquad 2.3$$

where, H_{1e} is the one-electron Hamiltonian and E_k and $\psi_k(\boldsymbol{r})$ are the corresponding energy eigenvalues and wavefunctions respectively. The wavefunctions can be expressed as Bloch functions of the form[122],

$$\psi_k(\boldsymbol{r}) = u_k(\boldsymbol{r})\exp(i\boldsymbol{k}\cdot\boldsymbol{r}), \qquad 2.4$$

where $u_k(\boldsymbol{r})$ is a periodic function with the periodicity of the crystal lattice and $\exp(i\boldsymbol{k}\cdot\boldsymbol{r})$ is a plane wave with wavevector $\boldsymbol{k}$.

If the electrons are in free space, where $V(\boldsymbol{r})$ is a constant, the equation of motion is[122],

$$-\frac{\hbar^2\boldsymbol{\nabla}^2}{2m}\psi_k(\boldsymbol{r}) = \frac{\hbar^2k^2}{2m}\psi_k(\boldsymbol{r}) = E_k\psi_k(\boldsymbol{r}). \qquad 2.5$$

In this case, the electron energy eigenvalues scale quadratically with the wavevector, so the allowed energy states may be plotted as a parabola, as shown in Figure 2.3. If the electrons are in a crystal lattice, where $V(\boldsymbol{r})$ is periodic due to the regularly spaced atomic cores that are each a distance a apart, the plane waves at the Brillouin zone

boundaries $\pm\frac{\pi}{a}$ undergo Bragg reflection. This leads to the formation of standing waves with higher charge density either in between the positions of the atomic cores[122],

$$|\psi(-)|^2 \propto \sin^2\left(\frac{\pi x}{a}\right), \quad 2.6$$

or at the positions of the atomic cores[122],

$$|\psi(+)|^2 \propto \cos^2\left(\frac{\pi x}{a}\right), \quad 2.7$$

in one-dimension x. Therefore, electrons with the same wavevector can have different energies – depending on whether the higher charge density is at the positions of the atomic cores or in between the positions of the atomic cores – and a bandgap is formed.

Image removed for copyright reasons.

Figure 2.3 Diagram demonstrating band formation in semiconductors, taken from reference 122. *(A) Electron energy against wavevector for an electron in free space. (B) The formation of standing waves leads to regions of higher charge density either at the positions of the atomic cores or in between the positions of the atomic cores. This leads to the formation of a band gap (C) at the Brillouin zone boundaries.*

The origin of the bandgap can also be understood by considering the atomic orbitals of the atoms in the crystal lattice, as shown in Figure 2.4. In a typical inorganic semiconductor such as Si, Ge, or GaAs, each isolated atom has on average four valence electrons that occupy discrete atomic *s* and *p* states. In the presence of neighbouring

atoms, these discrete atomic *s* and *p* states hybridise and form bonding and antibonding molecular orbitals. In a crystal lattice, this leads to the formation of the valence band and conduction band – and a bandgap is formed[123]. In lead halide perovskites, the valence band maxima dominantly arise from the 6s and 5p orbitals of the lead and iodine atoms respectively and the conduction band minima dominantly arise from the 6p orbitals of lead atoms[52].

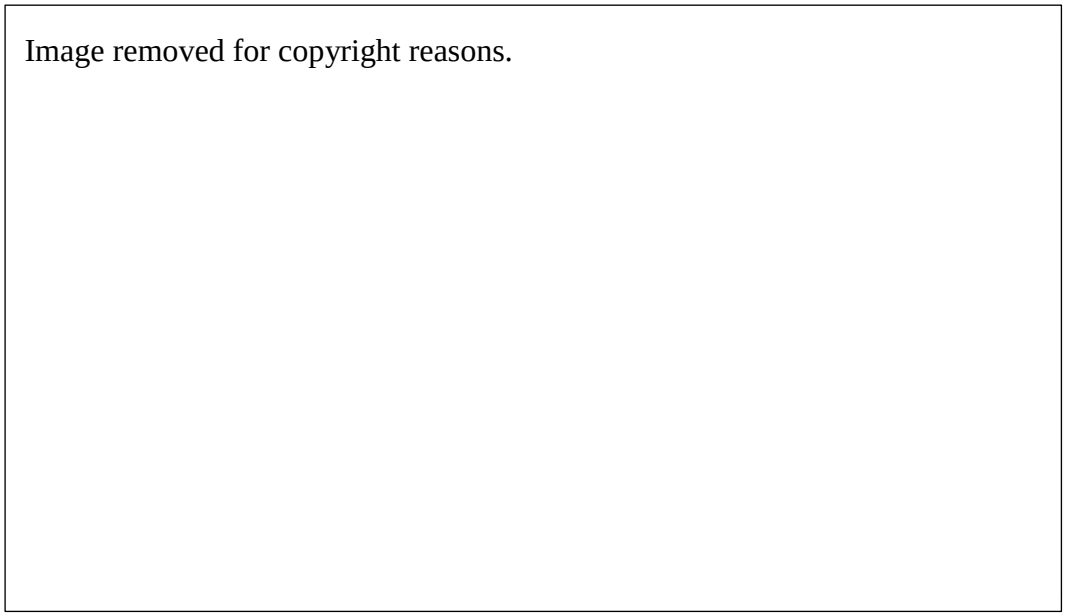

Figure 2.4 Diagram demonstrating band formation in typical inorganic semiconductors such as Ge and GaAs, taken from reference 123. *The discrete atomic s and p orbitals evolve into s and p bonding and antibonding molecular orbitals and then into bands.*

In general, the formed bandgap can be either direct – where the valence band maximum and conduction band minimum occur at the same wavevector – or indirect – where the valence band maximum and conduction band minimum occur at different wavevectors – as shown in Figure 2.5. This is an important distinction, because in order to conserve momentum, the wavevector of an electron is effectively unchanged after photon absorption (which is why photon absorption processes are always represented as vertical lines on diagrams of energy verses wavevector)[123]. Therefore, in semiconductors with an indirect bandgap, an additional phonon – quantised lattice vibration – must also be absorbed or emitted in order for the momentum to be conserved and photoexcitation to occur. It is currently heavily debated whether lead halide perovskites are direct bandgap or indirect bandgap semiconductors[44,124–126], as we will discuss in more detail in Chapter 4.

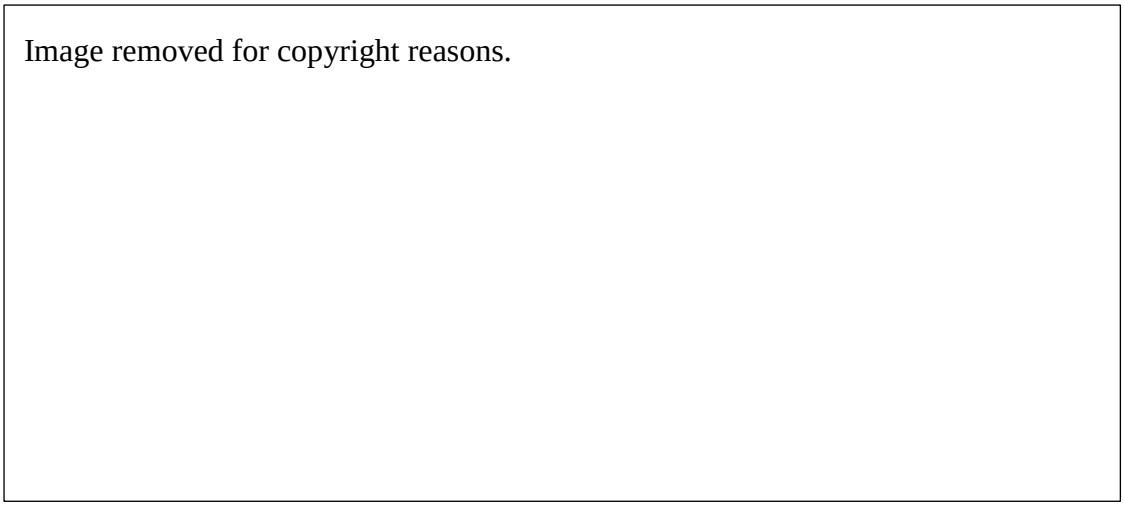

Figure 2.5 Diagram of a direct and indirect semiconductor bandgap, taken from reference 123. *(A) Direct bandgap. (B) Indirect bandgap. Both photon absorption (vertical arrow) and phonon absorption or emission (horizontal arrow) are required for photoexcitation in an indirect bandgap semiconductor such as Si.*

In this section, we have discussed the origin of the semiconductor bandgap. In the next section, we will discuss how this semiconductor bandgap is important for the interaction of semiconductors with light.

2.2.2 Interaction of semiconductors with light

In general, when light is incident on a semiconductor, it may be reflected from the semiconductor, interact with the semiconductor or be transmitted through the semiconductor, as summarised in Figure 2.6[123]. If the light interacts with the semiconductor, a number of simple linear processes and more complicated non-linear processes can occur. The simplest interactions that can occur are refraction, scattering, absorption and luminescence[123].

Image removed for copyright reasons.

Figure 2.6 Summary of general linear optical processes, adapted from reference 123. *Light incident on a material may be reflected from the front or back surfaces of the material, undergo refraction, scattering, or absorption and luminescence in the material, or be transmitted through the material. The narrowing of the arrows indicates attenuation of the light.*

2.2.2.1 Refraction

Refraction occurs when the incident light propagates with a smaller velocity through the semiconductor than in free space, but it does not change the intensity of the propagating light. The reduction in velocity is described by the refractive index of the material (n),

$$n = \frac{c}{v} \tag{2.8}$$

where v is the velocity of light in the material and c is the velocity of light in a vacuum[123]. The refractive index depends on the frequency of the light propagating through the material, but in materials with low dispersion over visible wavelengths, it is common to characterise the material with a single refractive index.

2.2.2.2 Scattering

Scattering causes the direction and in some cases the frequency of the incident light to change, but it does not change the overall number of photons. In elastic scattering processes, the frequency of the scattered light is the same as the frequency of the incident light and in inelastic scattering processes, the frequency of the scattered light is different to the frequency of the incident light. In inelastic scattering processes, if the frequency of the light increases, energy must be transferred from the material and if the frequency of the light decreases, energy must be transferred to the material.

2.2.2.3 Absorption

Absorption causes the incident beam to be attenuated as it passes through the semiconductor. It can be described classically (dipole oscillator model), semi-classically (Fermi's golden rule) and quantum mechanically (quantum optics). In the classical description, both the atoms and light are modelled classically. It is assumed that each pair of negatively charged bound electrons and positively charged nuclei in the semiconductor behave as classical electric dipoles, with electric dipole moments that are proportional to their separation. The alternating electric field of the incident light exerts a force on the negatively charged bound electrons and on the positively charged nuclei, driving oscillations. Since the masses of the nuclei are orders of magnitude higher than the masses of the electrons, only the electrons can respond to the rapidly oscillating electric field of the light. The electrons behave as classical Lorentz oscillators, undergoing high amplitude oscillations when the frequency of the incident light matches

their natural resonance frequency. Therefore, only these frequencies of incident light are absorbed by the semiconductor[123].

In the semi-classical description, the atoms are modelled using quantum mechanics and the light is modelled classically. It is assumed that the atoms consist of discrete energy levels that can be occupied by electrons. The transition rate ($W_{1\to2}$) between two discrete states 1 and 2 is described by Fermi's golden rule[123],

$$W_{1\to2} = \frac{2\pi}{\hbar}|M_{12}|^2\delta(E_2 - E_1 - h\nu), \tag{2.9}$$

where E_1 and E_2 are the energies of states 1and 2, $h\nu$ is the energy of the incident light with frequency ν, and M_{12} is the matrix element for the transition. The matrix element has the form[123],

$$M_{12} = \langle 2|H'(\boldsymbol{r})|1\rangle = \int \psi_2^*(\boldsymbol{r})H'(\boldsymbol{r})\psi_1(\boldsymbol{r})d^3\boldsymbol{r}, \tag{2.10}$$

where $\boldsymbol{r}$ is the position vector of each electron, $\psi_1(\boldsymbol{r})$ and $\psi_2(\boldsymbol{r})$ are the wavefunctions of states 1 and 2 and $H'(\boldsymbol{r})$ is the perturbation to the Hamiltonian of each electron due to the alternating electric field of the incident light. According to Equation 2.9, the transition rate is only non-zero when the frequency of the incident light exactly matches the energy difference between the two discrete states 1 and 2. In a semiconductor, transitions occur between continuous bands 1 and 2 rather than discrete states 1 and 2. In this case, the transition rate can be written as[123],

$$W_{1\to2} = \frac{2\pi}{\hbar}|M_{12}|^2 g(h\nu), \tag{2.11}$$

where $g(h\nu)$ is the weighted joint density of states of the two bands 1 and 2 – describing the number of states $g(h\nu)dE$ within the energy range E to $E + dE$ for an energy $h\nu$ – and $h\nu$ is the energy of the incident light with frequency ν. According to this equation, the transition rate is only non-zero when the density of states is non-zero. Therefore, only these frequencies of light are absorbed by the semiconductor[123]. A fully quantum mechanical description of absorption may be found in quantum optics literature[127–129].

The amount of incident light absorbed by a semiconductor can be quantified by the optical density (OD) – or absorbance – of the semiconductor, or the absorption coefficient (α) – or absorption cross-section – of the semiconductor. The OD or

absorbance of a semiconductor is defined as the logarithm of the ratio of the number of photons transmitted (n_{trans}) through the semiconductor to the number of photons incident (n_{incid}) on the semiconductor,

$$\mathrm{OD} = -log_{10}\left(\frac{n_{trans}}{n_{incid}}\right). \quad 2.12$$

The absorption coefficient or absorption cross-section of a semiconductor is defined as the logarithm of the ratio of the number of photons transmitted (n_{trans}) through the semiconductor to the number of photons incident (n_{incid}) on the semiconductor per unit length of the semiconductor. It can be calculated from the OD of the semiconductor by dividing by the thickness of the semiconductor (d),

$$\alpha = \frac{1}{d}\mathrm{OD} = -\frac{1}{d}log_{10}\left(\frac{n_{trans}}{n_{incid}}\right). \quad 2.13$$

As a semiconductor absorbs incident light, electrons in the valence band are photoexcited into the conduction band. These photoexcited charge carriers subsequently undergo relaxation. The relaxation dynamics may be described by four temporally overlapping regimes[130], the decoherence regime (first few tens of femtoseconds), the thermalisation regime (~0-500 fs), the cooling regime (~0.2-500 ps), and the recombination regime (> 1 ps).

2.2.2.3.1 Decoherence regime (first few tens of femtoseconds)

Immediately after room-temperature photoexcitation of an inorganic semiconductor such as GaAs, Si or lead halide perovskite, a coherent population of free carriers is generated. The system is defined as coherent when there is a well-defined relationship between the phase of the exciting electromagnetic field and the photoexcited free carrier distribution, as well as a well-defined phase relationship within the photoexcited free carrier distribution. Scattering processes rapidly destroy these coherences within a few tens of femtoseconds in inorganic semiconductors[131].

2.2.2.3.2 Thermalisation regime (~0-500 fs)

The photoexcited free carrier population following decoherence through dephasing is most likely to have a non-thermal distribution. This initial non-thermal energy distribution is determined by the incident light spectrum and cannot be characterised with a temperature. In inorganic semiconductors, relaxation of this non-thermal population to a hot thermalised population occurs within the first ~500 fs after

photoexcitation. Relaxation dominantly occurs through carrier-carrier scattering processes. This has been probed in GaAs using transient spectroscopy techniques such as transient absorption[132] and transient photoluminescence[133]. However, in these studies, only an upper limit could be placed on the thermalisation times, because thermalisation occurred within the time resolution of the experimental setup.

The difficulty in measuring thermalisation times with these techniques is that both high time and high energy resolution are required. High time resolution is required because the relaxation processes are extremely fast. High energy resolution is required in order to identify the transition from a spectrally narrow non-thermal energy distribution to a spectrally broad thermalised Fermi-Dirac distribution with a defined temperature.

High time and energy resolution are difficult to achieve in a simple transient absorption experiment because of the uncertainty principal in quantum mechanics that puts a fundamental limit on the precision with which complementary variables, such as time and energy, can be known. The time-energy uncertainty relation has the form,

$$\sigma_\tau \cdot \sigma_E \geq \frac{\hbar}{2}, \qquad 2.14$$

where σ_τ is the uncertainty in the time, σ_E is the uncertainty in the energy and $\hbar$ is the reduced Plank constant[134]. This means that it is not possible to create a temporally and energetically narrow excitation pulse, only a temporally narrow and spectrally broad pulse or a temporally broad and spectrally narrow pulse.

These restrictions can be overcome by using a more complex variety of transient absorption spectroscopy known as two-dimensional electronic spectroscopy. In these measurements two pump pulses are used instead of one and the data is extracted using a Fourier transform approach. Using this technique, thermalisation has been studied in lead halide perovskites by others in our research group. In their study[135], it was found that in $CH_3NH_3PbI_3$ perovskite the dominant process involved in thermalisation is carrier-carrier scattering and that thermalisation occurs on timescales of below 10 fs to 85 fs, depending on the carrier density and excess energy above the optical band gap.

2.2.2.3.3 Cooling regime (~0.2-500 ps)

The redistribution of energy within the free carrier population by carrier-carrier scattering processes results in a thermalised distribution. This quasi-equilibrium distribution can be described by a Fermi-Dirac distribution of the form,

$$n_i = \frac{1}{e^{(\epsilon_i - \mu)/k_B T} + 1} \quad 2.15$$

where, n_i is the average number of electrons and holes in state i, ϵ_i is the energy of state i, μ is the Fermi level, k_B is the Boltzmann constant and T is the average temperature of the electrons and holes[136].

The average temperature of the electrons and holes is initially much higher than the temperature of the lattice. Therefore, these carriers are referred to as hot carriers. During the cooling regime, these hot carriers undergo numerous scattering events with phonons – quantised lattice vibrations – which lower the temperature of the hot carrier distribution until it is in equilibrium with the lattice[136].

In lead halide perovskites, carrier cooling occurs in two stages[137,138]. During the first ~2 ps, hot carriers undergo rapid cooling by emitting longitudinal optical phonons[139,140]. The rate of this cooling is highly carrier density dependent[137], with decay rates ranging from 230 fs at 6×10^{17} cm^{-3} to 770 fs at 60×10^{17} cm^{-3}. This decrease in decay rate at higher carrier densities arises because carriers begin to undergo substantial reheating by reabsorbing a substantial number of longitudinal optical phonons – an effect known as the hot phonon bottleneck effect[137,141], which is commonly observed in inorganic semiconductors[142,143]. After ~2 ps, carriers continue to slowly cool by emitting either delayed longitudinal optical phonons or lower energy acoustic and optical phonons[137].

2.2.2.3.4 Recombination regime (> 1 ps)

Following decoherence, thermalisation and cooling, the majority of photoexcited charge carriers undergo recombination and relax back to the ground state[138]. A small fraction of charge carriers will already have undergone recombination during the thermalisation and cooling regimes, as observed in hot photoluminescence measurements[144,145]. In general, charge carrier recombination occurs through a number of different radiative and non-radiative mechanisms[146,147].

Band-to-band recombination

In band-to-band recombination, an electron in the conduction band recombines with a hole in the valence band. In direct semiconductors, since the bottom of the conduction band and the top of the valence band are aligned in k space, direct optical transitions are possible. This is not the case in indirect semiconductors, in which the bottom of the conduction band and the top of the valence band are offset in k space. In indirect

semiconductors, band-to-band recombination in only possible with the assistance of a phonon and is therefore much less likely.

In semiconducting bulk materials, free charge carriers can freely diffuse and interact throughout the entire material. Therefore, the band-to-band recombination rate $-\frac{dn(t)}{dt}$ at a given time t scales linearly with both the electron n_e and hole n_h density. Therefore, if $n_e = n_h = n$, the band-to-band recombination rate scales quadratically with charge carrier density n,

$$-\frac{dn(t)}{dt} \propto n_e n_h - n_{e,i} n_{h,i} \propto n(t)^2 - n_i(t)^2, \quad 2.16$$

where $n_{e,i}$ and $n_{h,i}$ are the intrinsic densities of thermally excited electrons and holes respectively. In an undoped semiconductor, $n_{e,i} = n_{h,i} = n_i$, where n_i is the intrinsic density of thermally excited charge carriers. The total charge carrier density is the sum of the intrinsic density of thermally excited charge carriers n_i plus the density of photoexcited charge carriers Δn,

$$n = n_i + \Delta n. \quad 2.17$$

In semiconducting nanomaterials, free charge carriers can freely diffuse and interact within individual nanoregions but do not freely diffuse and interact between different nanoregions. Therefore, when the total charge carrier density is lower than the nanoregion density the band-to-band recombination rate scales linearly with total charge carrier density,

$$-\frac{dn(t)}{dt} \propto n(t) - n_i(t), \quad 2.18$$

as shown in Figure 2.7.

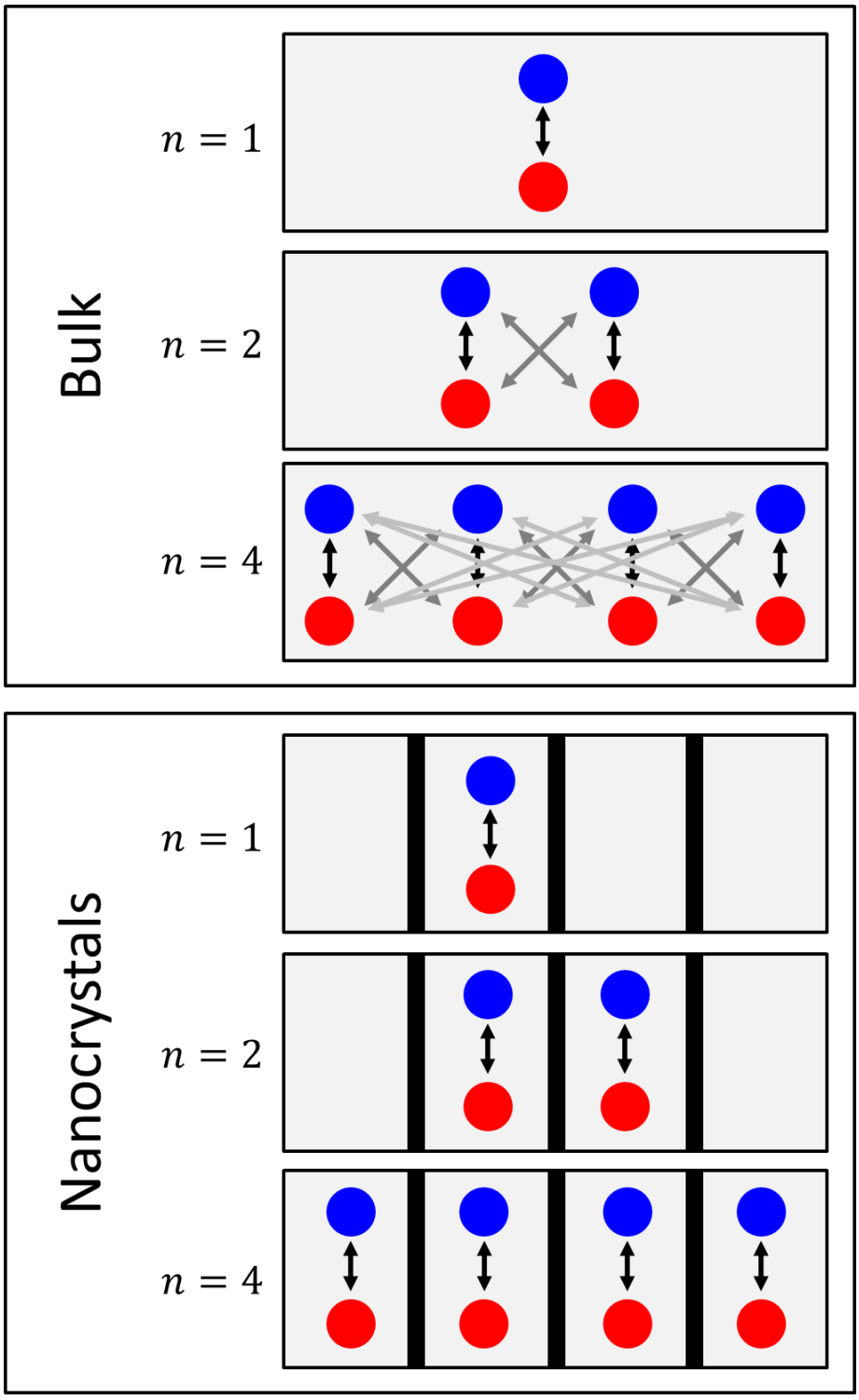

Figure 2.7 Diagram of charge carrier interactions in semiconducting bulk materials and semiconducting nanomaterials. *Assuming that the charge carrier density* ***n*** *is lower than the nanoregion density and that charge carriers in different nanoregions do not interact, the recombination rate in samples consisting of many nanoregions scales with the charge carrier density.*

In heavily doped semiconducting bulk materials, the intrinsic charge carrier densities can be significantly larger than the photoexcited charge carrier densities. In this case, the band-to-band recombination rate effectively scales linearly with the dominating intrinsic charge carrier density. In general, the band-to-band recombination rate expands as,

$$-\frac{dn(t)}{dt} \propto n_e n_h - n_{e,i} n_{h,i} \propto \left(n_{e,i} + \Delta n_e\right)\left(n_{h,i} + \Delta n_h\right) - n_{e,i} n_{h,i} \propto n_{e,i}\Delta n_h + \Delta n_e n_{h,i} + \Delta n_e \Delta n_h \quad 2.19$$

Therefore, for a heavily n-doped semiconductor, where $n_{e,i} \gg n_{h,i}, \Delta n_e, \Delta n_h$, the band-to-band recombination rate approximates to,

$$-\frac{dn(t)}{dt} \propto n_{e,i}\Delta n_h, \quad 2.20$$

and for heavily p-doped semiconductor, where $n_{h,i} \gg n_{e,i}, \Delta n_e, \Delta n_h$, the recombination rate is approximately,

$$-\frac{dn(t)}{dt} \propto \Delta n_e n_{h,i}. \quad 2.21$$

Shockley-Read-Hall recombination

In Shockley-Read-Hall recombination, free charge carriers recombine with trapped charge carriers. Free charge carriers can become trapped charge carriers due to crystal lattice defects such as dislocations, impurities and disorder. The Shockley-Read-Hall trap-assisted recombination rate is given by[148],

$$-\frac{dn(t)}{dt} = \frac{n_e n_h - n_{e,i} n_{h,i}}{\tau_e\left(n_h + n_{h,t}\right) + \tau_h\left(n_e + n_{e,t}\right)}, \quad 2.22$$

where τ_e and τ_h are the effective electron and hole lifetimes respectively and $n_{e,t}$ and $n_{h,t}$ are the electron and hole densities when their quasi-Fermi levels reach the trap energy level respectively.

Auger recombination

In Auger recombination, a recombining electron and hole transfer their energy to a third electron or hole that subsequently occupies a higher energy state in the semiconductor band structure. Therefore, the Auger recombination rate scales linearly with the density of each of the three involved charge carriers,

$$-\frac{dn(t)}{dt} \propto n^3. \quad 2.23$$

Auger recombination is the opposite of the impact ionization process, in which an energetic charge carrying species transfers excess energy to an electron in the valence band and excites it into the conduction band.

Surface and interface recombination

Surface and interface recombination are important in optoelectronic devices, however they are analytically complex and often specific to the optoelectronic device under consideration. Since the focus of this thesis is on understanding the fundamental photophysical properties of isolated materials rather than devices, we will not consider them further. More information about surface and interface recombination may be found in the literature[149].

General recombination rate equation

Since the intrinsic room-temperature carrier density in semiconductors such as GaAs and Si is only ~10^6cm^{-3} and ~10^9cm^{-3} respectively[150], under standard optoelectronic device operating conditions, $n_i \ll \Delta n$ and $n \approx \Delta n$. Therefore, from now on, we will always refer to the photoexcited carrier density Δn as n.

As we have discussed, charge carrier recombination can occur through a number of different radiative and non-radiative mechanisms[146,147], with different dependencies on photoexcited charge carrier density, $n(t)$. We can express the general rate of reduction in the carrier density $-\frac{dn(t)}{dt}$ due to charge carrier recombination as a sum of these competing recombination mechanisms[147,151–153],

$$-\frac{dn(t)}{dt} = k_1 \cdot n(t) + k_2 \cdot n(t)^2 + k_3 \cdot n(t)^3. \quad 2.24$$

In this general recombination rate equation, k_1 is the first-order recombination rate constant, k_2 is the second-order recombination rate constant and k_3 is the third-order recombination rate constant. First-order recombination is the dominant recombination mechanism in inorganic semiconductor materials that are heavily doped, have high trap densities[151], have bound excitons as the dominant photoexcited species[154], or consist of domains in which photoexcited charge carriers are dielectrically or spatially localised so that geminate recombination (recombination of the initially photoexcited electron-hole

pair) is significantly more likely than non-geminate recombination (recombination of an electron and hole from different photoexcitation events)[155–158]. Second-order recombination is the dominant recombination mechanism in inorganic semiconductor materials with free charge carriers as the dominant photoexcited species. Third-order recombination is the dominant recombination mechanism in inorganic semiconductors with high carrier densities[152,159], which can arise in semiconductors with a small bandgap[154], from heavy doping[154], or from high intensity photoexcitation[152,153].

The photoexcitation densities at which these first-order, second-order and third-order recombination processes dominate – and the corresponding recombination rate constants – can be investigated using transient absorption (TA) measurements. TA is a time-resolved spectroscopic technique, described in detail in Section 3.3.3, that can be used to probe the relaxation of electronic states in semiconductors. When first-order recombination dominates, the normalised kinetics obtained from TA are excitation density independent[9,160], because doubling the excitation density doubles the recombination rate. However, when second-order or third-order recombination dominates, the normalised kinetics obtained from TA are excitation density dependent[161], because doubling the excitation density either quadruples or octuples the recombination rate.

In bulk lead halide perovskite films[152], the dominant recombination regime is first-order at low photoexcitation densities below around 10^{16} cm^{-3}, second-order at medium photoexcitation densities between 10^{16}-10^{18} cm^{-3} and third-order at high photoexcitation densities above around 10^{18} cm^{-3}. These values are extracted from plots of recombination rate against photoexcited carrier density obtained from excitation density dependent TA measurements, as shown in Figure 2.8.

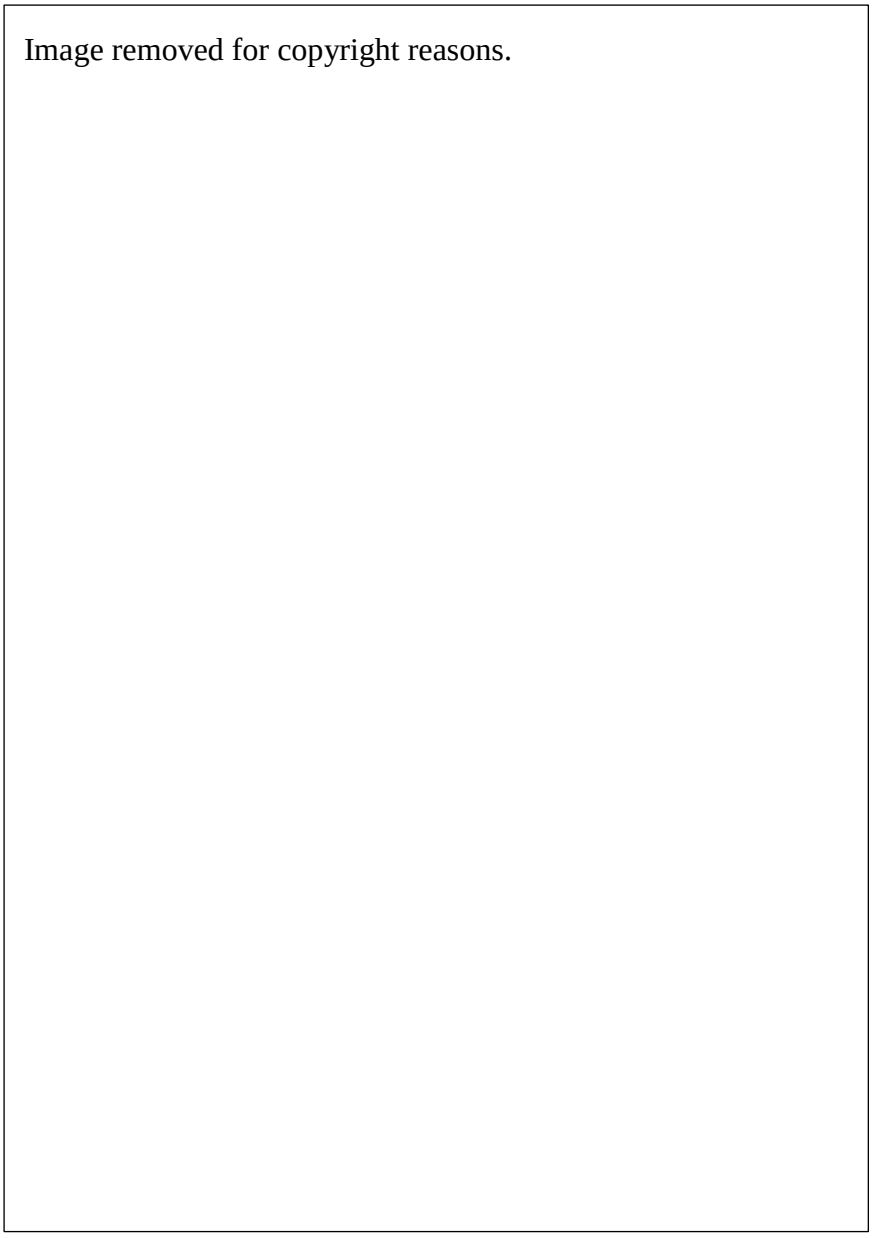

Figure 2.8 Recombination rate as a function of photoexcitation density (A) and TA signal as a function of time (B) for $CH_3NH_3PbI_3$ films, both taken from reference 152. *The dominant recombination regime changes from first-order (red), to second-order (blue) and then to third-order (black) as the photoexcitation density increases. The overlapping TA kinetics confirm that the recombination rate is only dependent on carrier density.*

In these measurements, a value proportional to the photoexcited carrier density as a function of time t is obtained by spectrally integrating over the ground state bleach (GSB) signal – which arises from phase-space filling by photoexcited carriers[137,138,154,162,163] – as a function of time t. This is converted into the actual photoexcited carrier density $n(t)$ as a function of time t by normalising the spectral integral immediately after photoexcitation to the initial photoexcited carrier density. The initial photoexcited carrier density is calculated from the experimental parameters used in the measurement using,

$$n\ (cm^{-3}) = \frac{OD * P\ (W) * \lambda\ (m)}{d\ (m) * f_{rep}(s^{-1}) * h\ (m^2\ kg\ s^{-1}) * c\ (m\ s^{-1}) * \pi * r^2(m^2) * 1e6} \quad 2.25$$

where, OD is the optical density of the sample, P is the excitation power, λ is the excitation wavelength, d is the thickness of the sample, f_{rep} is the excitation pulse repetition rate, h is the Plank constant, c is the speed of light and r is the radius of the excitation spot.

The spectral integral of the GSB is known to be a good measure of the carrier density, because the spectral integral of the GSB immediately after photoexcitation scales linearly with excitation power[152]. In addition, the spectral integral of the GSB decays smoothly over several orders of magnitude, confirming that the recombination rate is only dependent on carrier density and does not have any memory of previous measurements[152], as shown in Figure 2.8. This is important for the interpretation of the results presented in Chapters 4, 5 and 6.

2.2.2.4 Luminescence

If a photon is emitted during a recombination event, the recombination is known as radiative recombination. Radiative recombination is extremely important for optoelectronic device performance. In a light-emitting diode, efficient radiative recombination is required for efficient light emission and therefore high external quantum efficiencies. In a solar cell, efficient radiative recombination is required for high open-circuit voltage and therefore high power conversion efficiency.

The efficiency of radiative recombination in a semiconductor can be quantified by the photoluminescence quantum efficiency (PLQE) of the semiconductor[164],

$$\mathrm{PLQE} = \frac{\left(-\frac{dn(t)}{dt}\right)_{rad}}{\left(-\frac{dn(t)}{dt}\right)_{rad} + \left(-\frac{dn(t)}{dt}\right)_{non-rad}} \quad 2.26$$

where $\left(-\frac{dn(t)}{dt}\right)_{rad}$ is the radiative recombination rate and $\left(-\frac{dn(t)}{dt}\right)_{non-rad}$ is the non-radiative recombination rate. It can be measured accurately using the integrating sphere method described in detail in Section 3.2.5. When the PLQE of a semiconductor is less than unity, the open-circuit voltage V_{OC} is reduced to[165],

$$V_{OC} = V_{OC,SQ} - \frac{\mathrm{k}_B T}{q} ln\left(\frac{1}{\mathrm{PLQE}}\right) \quad 2.27$$

where $V_{OC,SQ}$ is the open-circuit voltage predicted by Shockley and Queisser[102] for an ideal solar cell, k_B is the Boltzmann constant, T is the temperature and q is the electronic charge. Therefore, semiconductors with higher PLQEs generally perform better in optoelectronic devices than semiconductors with lower PLQEs.

The recombination rates extracted from TA arise from both radiative – light emitting – and non-radiative processes. In order to distinguish between these radiative and non-radiative processes, TA measurements are combined with TPL measurements. The TPL signal $\mathrm{TPL}(t)$ as a function of time t is proportional to the radiative recombination rate $\left(\frac{\mathrm{d}n(t)}{\mathrm{d}t}\right)_{rad}$ as a function of time t.

$$\mathrm{TPL}(t) \sim \left(-\frac{\mathrm{d}n(t)}{\mathrm{d}t}\right)_{rad} \quad 2.28$$

However, since the radiative recombination rate is a function of carrier density, the TPL signal is dependent on both the radiative and non-radiative recombination processes occurring in the material. Therefore, a first-order or third-order non-radiative recombination process may dominate the carrier density decay – and therefore also the TPL signal decay – despite radiative recombination only occurring through a second-order process. This is the case in typical lead halide perovskite films[152].

In order to identify whether radiative recombination occurs through a first-order, second-order, or third-order process, either the initial TPL signal immediately after photoexcitation may be plotted as a function of the initial excitation density[152], or the TPL signal as a function of time can be plotted against the TA signal measured at the

same times[152]. Therefore, by combining the data from TA and TPL measurements, it is possible to identify both the radiative and non-radiative recombination regimes occurring in a material, as we will discuss in more detail in Chapters 4, 5 and 6.

In this section, we have discussed the general interaction of semiconductors with light. In the next section, we will consider the interaction of semiconductors with linearly polarised light.

2.2.3 Interaction of semiconductors with linearly polarised light

Linearly polarised light may be used to investigate intrinsic (steady-state) and induced (transient) anisotropy in a material. It is important to study these properties as both intrinsic and induced anisotropies provide information about the interaction between polarised light and matter in optoelectronic devices. This is particularly important for devices such as LEDs and laser cavities, where the intensity and wavelength of radiative emission from these devices will depend strongly on anisotropies in the material.

2.2.3.1 Intrinsic anisotropy

Materials with intrinsic polarisation anisotropy exhibit anisotropic absorption for different polarisations of light. This anisotropy will be evident both under pulsed and continuous optical excitation, and does not vary with time. The most common example of such a system is an absorbing linear polariser, of which there are many types. Wire grid polarisers, consisting of an array of equally spaced parallel metallic wires sandwiched between a glass substrate, are the most common. Incident light with an electric field oscillating parallel to the wires causes the electrons in the wire to move along the wires, leading to Joule heating and preferential absorption of the light polarised parallel to the wire[166]. Other examples are polaroid polarisers, consisting of many microscopic crystals of iodoquinine sulphate (herapathite) embedded in a polymer film, which preferentially absorb light polarised along a particular direction of the crystal structure[167] and nanoparticle film polarisers, consisting of spherical ellipsoid nanoparticles embedded in a glass substrate, which again preferentially absorb light polarised perpendicular to a particular axis of transmission[168].

Since excitation of an intrinsically anisotropic material leads to a population of polarized excited states, if these decay radiatively, a corresponding intrinsic anisotropic photoluminescence may be observed. One example is aligned films of poly(2-methoxy, 5-(2'-ethyl-hexoxy)-p-phenylenevinylene) in polyethylene[169]. In these films, the large

anisotropy observed in absorption and photoluminescence arises from the highly ordered alignment of the polymer chains, achieved by tensile drawing of the material while it was a polymer gel. Another example is aligned films of arylenevinylene polymers[170], liquid crystal polymers used in liquid crystal displays. In these films, the large anisotropy observed in absorption and photoluminescence again arises from the highly ordered alignment of the polymer chains, but alignment was achieved by spin coating on top of a rubbed polyimide alignment substrate rather than by tensile drawing. Many more examples of aligned polymer films with intrinsic polarisation anisotropy giving rise to anisotropic photoluminescence and electroluminescence may be found in the literature[171].

Such intrinsic anisotropic absorption and photoluminescence has also been observed in inorganic single crystals. One example is GaN[172], a highly luminescent semiconductor material used to make blue LEDs[173,174]. GaN has two common crystal structures, a cubic zinc-blende structure and a hexagonal wurtzite structure[175]. In the zinc-blende structure, since every crystal axis is equivalent, absorption and photoluminescence are isotropic. However, in the wurtzite structure, because of the crystal field along the long c axis, absorption and photoluminescence are anisotropic.

The anisotropy observed in these single crystal wurtzite films[172], grown with the c axis parallel to the growth plane (1100) using metalorganic vapour phase epitaxy, arises from differences in the dipoles of the wavefunctions of the valence bands. GaN can be approximated to have one conduction band and three valence bands, labelled the heavy hole band, light hole band and split off band, as shown in Figure 2.9. The dipole of the wavefunction of the split off band is parallel to the c axis, which means that it strongly interacts with light polarised parallel to the c axis. In contrast, the dipole of the wavefunctions of the heavy hole and light hole bands are perpendicular to the c axis, which means that they interact strongly with light polarised perpendicular to the c axis. Since the band gap is smaller for the light hole and heavy hole bands than the split off band, the emission perpendicular to the c axis is lower in energy than the emission parallel to the c axis[172]. The photoluminescence intensity is larger for emission perpendicular to the c axis simply because there is a larger thermal distribution of carriers in the light hole and heavy hole bands[172].

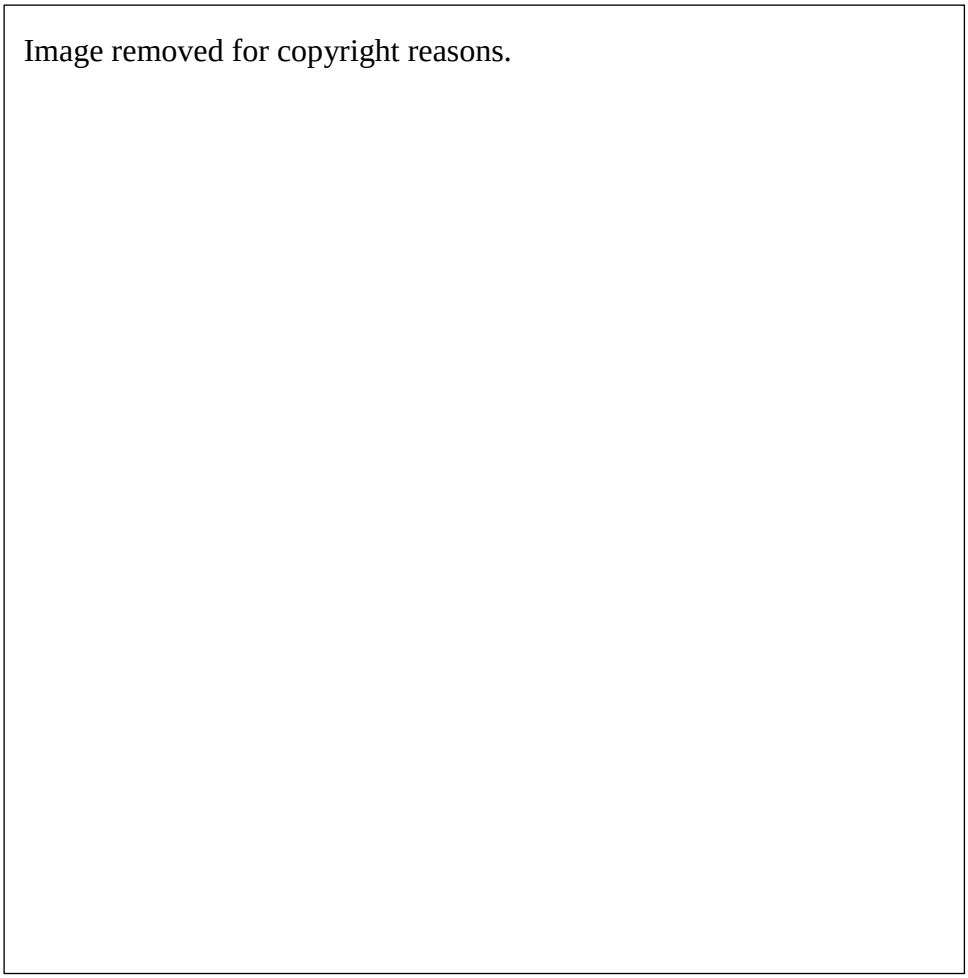

Figure 2.9 Intrinsic anisotropy in wurtzite GaN, taken from reference 172. *(A) Polarisation selective photoluminescence spectra of a GaN (1100) single crystal and the simplified band structure of GaN indicating the conduction band, heavy hole band, light hole band and split-off band. The photoluminescence (B) wavelength and (C) intensity shift with polarisation angle only when the c axis is parallel to the growth plane (1100).*

Even if the relaxed crystal structure is isotropic, intrinsic anisotropy may also be induced by strain. This can be observed in inorganic layered structures, for example in GaAs layers grown on Si substrates using atmospheric-pressure metal organic chemical vapour deposition[176]. In this case, the tensile stress which arises during postgrowth cooling, because of the difference in the thermal expansion coefficients of GaAs and Si, leads to the formation of numerous microcracks in the (110) direction. Preferential absorption along these parallel cracks gives rise to intrinsic anisotropic absorption and photoluminescence[176]. Another instance is an $In_{0.1}Ga_{0.9}N$/GaN multiple quantum well structure grown on γ-$LiAlO_2$ using molecular beam epitaxy[177]. In this case, high compressive strain in these wells gives rise to intrinsic anisotropic absorption and photoluminescence.

Intrinsic anisotropy may also be observed in materials that are optically isotropic in their bulk form, when they are fabricated into anisotropic microstructures or nanostructures, for example in an isolated nanowire or carbon nanotube. Such intrinsic anisotropies have been observed in many samples including Ge nanowires[178], core/shell GaAs/AlGaAs nanowires[179] and Ag nanowires[180]. In such samples, the transition dipole moment is highly correlated with the physical structure. This has been demonstrated in linear polarisation selective transient absorption measurements on individual Si nanowires[181] and aligned bundles of single walled carbon nanotubes[182]. In these measurements, the ground state bleach signal, arising from phase-space filling by photoexcited carriers, is largest when the linear polarisation of the excitation pulse and the probe pulse are aligned parallel to the long axis of the sample. This suggests that the transition dipole moment is largest along the long axis of these materials. As shown in Figure 2.10, after correcting the transient absorption signal intensity for the differences in the transition dipole moment, no further differences are observed in the signals collected with linear polarisation of the pump and probe aligned parallel and perpendicular to the long axis of the samples. This indicates that the fundamental charge carrier relaxation and recombination processes occurring in these materials are independent of alignment within the sample.

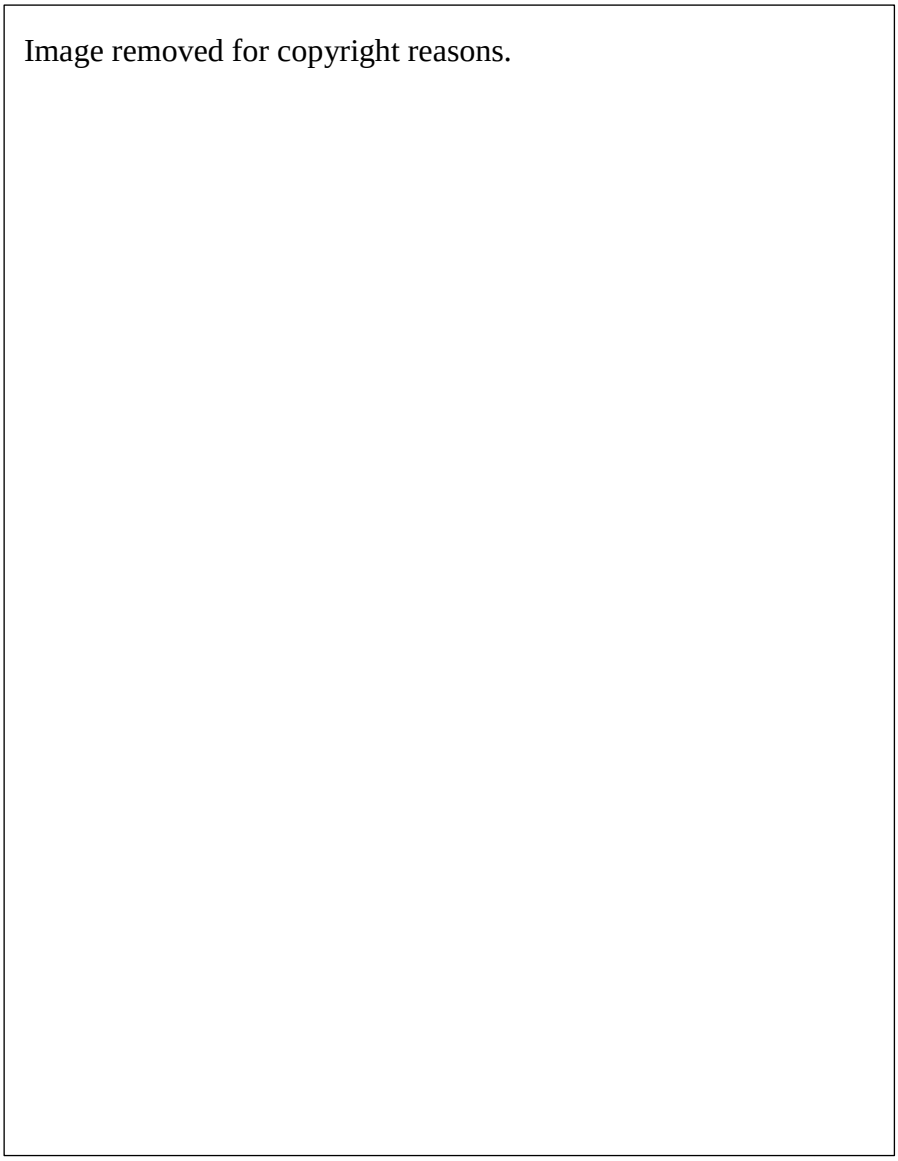

Figure 2.10 Linear polarisation selective transient absorption measurements on aligned silicon nanowires and single-walled carbon nanotubes, taken from references [181] and [182] respectively. *(A) The intensity of the ground state bleach signal changes when the excitation (E) and probe (P) pulses are polarised parallel (∥) or perpendicular (⊥) to the long axis of the silicon nanowires. However, when the signals are normalised, there is no difference in the kinetics. (B) The intensity of the ground state bleach signal changes when the polarisations of the excitation and probe pulses are parallel or crossed, while the excitation pulse remains polarised along the long axis of the single-walled carbon nanotubes. However, as in the silicon nanowires, when the signals are normalised, no differences in the kinetics are observed.*

2.2.3.2 Induced anisotropy

Even materials without intrinsic polarisation anisotropy may become anisotropic when perturbed with polarised light. This may occur, for example, in a material comprised of an isotropic distribution of individually absorbing species. In this case, photoexcitation with linearly polarised light preferentially excites an anisotropic subset of the available species. In other words, the polarised photoexcitation has induced an anisotropy in the system. Since the anisotropy is induced, it will strongly depend on the properties of the external perturbation and is likely to decay after the external perturbation has been removed. Usually this occurs because of randomisation in the orientations of the individual transition dipole moments through diffusion or reorganisation[183–187].

The most common definitions of the induced anisotropy $A(t)$ used in linear polarisation selective transient photoluminescence measurements and linear polarisation selective transient absorption measurements are given in Equations 2.29 and 2.30 respectively.

$$A(t) = \frac{I_{\parallel}(t) + I_{\perp}(t)}{I_{\parallel}(t) - 2I_{\perp}(t)} \tag{2.29}$$

$$A(t) = \frac{\left(\frac{\Delta T}{T}\right)_{\parallel}(t) - \left(\frac{\Delta T}{T}\right)_{\perp}(t)}{\left(\frac{\Delta T}{T}\right)_{\parallel}(t) + 2\left(\frac{\Delta T}{T}\right)_{\perp}(t)} \tag{2.30}$$

In the first equation, $I_{\parallel}(t)$ and $I_{\perp}(t)$ are the photoluminescence intensities detected with polarisation parallel and perpendicular to the polarisation of the excitation respectively. In the second equation, $\left(\frac{\Delta T}{T}\right)_{\parallel}(t)$ and $\left(\frac{\Delta T}{T}\right)_{\perp}(t)$ are the transient absorption intensities detected with the polarisation of the excitation and probe pulses aligned parallel and perpendicular to one another respectively.

As with intrinsic polarisation anisotropy, many different systems exhibit light-induced polarisation anisotropy. Commonly, linear polarisation selective transient photoluminescence and transient absorption measurements are used to study exciton diffusion in organic systems. In solutions of π-conjugated butadiyne-linked porphyrin nanorings[183], it was found that photoexcited excitons convert into relaxed or self-localized excitons within the first ~200 fs after photoexcitation. These excitons diffuse from their initial nanoring positions within ~20 ps and full randomisation of the transition dipole moments occurs when the nanorings rotationally diffuse in the

solution[183]. Similar measurements have also been done to measure the rotational dephasing time of symmetric molecules[184] and the rate of exciton diffusion between neighbouring polymer chains in amorphous polymer films with randomly aligned transition dipole moments[185–187].

Linear polarisation selective transient photoluminescence and absorption have also been carried out on inorganic semiconductors, in order to investigate charge carrier relaxation and induced birefringence in these materials. In Pr^{3+}-doped AsGaGeS glasses, photoexcitation with linearly polarised light leads to the formation of anisotropic metastable defect states[188]. Since photoexcited carriers are localised in these states, thermalisation does not lead to reorientation of the transition dipole moments. Instead, reorientation only occurs as the photoexcited carriers transfer into Pr^{3+} dopants or glass defects.

In standard cubic inorganic semiconductors, such as Si, GaAs and CaF_2, photoexcitation with linearly polarised light can induce birefringence. Depending on how strongly excitonic the system is, this birefringence occurs either because of a variation in dielectric constant with excitation wavevector (in the case of Si[189] and GaAs[190]) or from exciton dispersion (in the case of CaF_2[191]). However, this effect is tiny, giving rise to anisotropies on the order of $\sim 10^{-6}$ or $\sim 10^{-7}$, and can therefore not be detected in standard linear polarisation selective transient absorption measurements.

Significantly larger anisotropies have also been detected in GaAs, arising from the optical alignment of photoexcited electron momentum distributions. The momentum distribution functions for electrons photoexcited from the heavy and light hole bands to the conduction band are shown in Figure 2.11. These anisotropic momentum distributions arise in GaAs because the optical transition dipole moment varies with the angular momentum of the electronic wave functions[144,145,192–196]. Carrier-carrier scattering processes randomise these momentum distributions, which subsequently become isotropic within a few femtoseconds after photoexcitation[194].

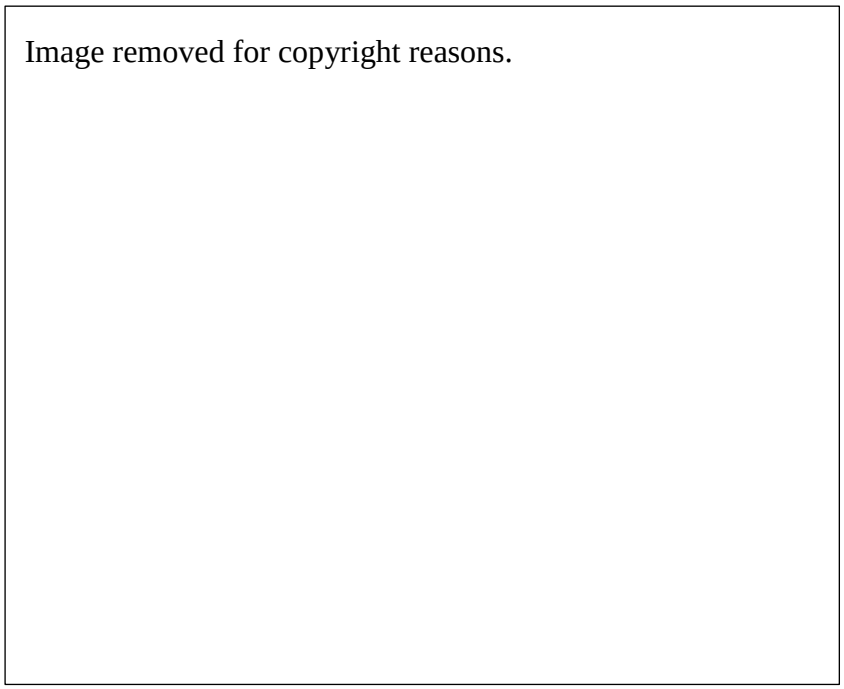

Figure 2.11 Momentum distribution functions of electrons photoexcited with linearly polarised light, taken from reference 192. *The symmetry axis of the photoexcited distribution is aligned along the polarisation vector of the excitation pulse ($\boldsymbol{e}_{exc}$) in both the (A) heavy hole to conduction band and (B) light hole to conduction band transitions. The spatial momentum alignment is obtained by rotating these distributions around the polarisation vector of the excitation pulse ($\boldsymbol{e}_{exc}$).*

In lead halide perovskites, anisotropy measurements have been used to measure spin-relaxation[197] and exciton diffusion[198,199]. We will discuss these measurements and the applications of these measurements in more detail in Chapter 4.

In this section, we have shown that intrinsic and induced anisotropies can significantly affect the interaction of semiconductors with light and should therefore be considered when fabricating optoelectronic devices such as solar cells and light-emitting diodes. In the next section, we will briefly discuss the key properties of solar cells and light-emitting diodes.

2.3 Solar cells and light-emitting diodes

Solar cells are optoelectronic devices that convert light energy into electrical energy and light-emitting diodes are optoelectronic devices that convert electrical energy into light energy.

Solar cells operate through the photovoltaic effect – the generation of electric current or voltage in a system upon illumination – which was first discovered in 1839 by Alexandre Edmond Becquerel[3]. Since the discovery of the photovoltaic effect, a number of different solar cell technologies have been developed[3,149,200,201] from both inorganic and organic materials with a number of different architectures such as p-n junctions[202] and heterojunctions[149].

Light-emitting diodes operate through electroluminescence – the emission of light from a material powered by an electrical power source – which was first discovered in SiC in 1907 by Henry Joseph Round[4]. Since the discovery of electroluminescence, a number of different light-emitting diode technologies have been developed[203,204] from both inorganic and organic materials with a number of different architectures such as p-n junctions[203,205] and heterojunctions[7].

The first lead halide perovskite solar cell was demonstrated in 2009, with a power conversion efficiency of only 3.8%[5]. Now, less than ten years later, lead halide perovskite solar cells have been demonstrated with over 22% power conversion efficiency[6].

The first lead halide perovskite light-emitting diode was demonstrated in 2014, with an external quantum efficiency of only 0.76%[7]. Now, less than five years later, lead halide

perovskite light-emitting diodes have been demonstrated with over 11% external quantum efficiency[76].

In the next section, we will discuss the definitions of a number of key performance indicators used to compare the performance of solar cells and light-emitting diodes in Chapters 4, 5 and 6.

2.3.1 Internal quantum efficiency (IQE)

The IQE of an optoelectronic device describes how efficiently the device converts between photons and charge carriers within the device. For solar cells, the IQE can be defined as the ratio of the number of photoexcited charge carriers collected from the photoactive layer to the number of photons absorbed by the photoactive layer[203]. For light-emitting diodes, the IQE is defined as the ratio of the number of photons emitted from the active region to the number of charge carriers injected into the active region[203]. Therefore, materials with higher IQEs generally perform better in optoelectronic devices.

2.3.2 Incoupling and outcoupling efficiencies

The incoupling and outcoupling efficiencies of an optoelectronic device describe how efficiently photons couple to the optoelectronic device. The incoupling efficiency is most important for solar cells and can be defined as the ratio of the number of photons incident on the device to the number of photons absorbed by the photoactive layer. The outcoupling efficiency is most important for light-emitting diodes and can defined as the ratio of the number of photons emitted from the device to the number of photons emitted from the active region. Both incoupling and outcoupling efficiencies are affected by the absorption of photons by the device substrate or metal contacts, the polarisation and energy of the photons, and refractive index effects such as total internal reflection and waveguiding.

2.3.3 External quantum efficiency (EQE)

The EQE of an optoelectronic device describes how efficiently the device converts between photons outside the device and charge carriers within the device. For solar cells, the EQE can be defined as the IQE multiplied by the incoupling efficiency[203]. For light-emitting diodes the EQE can be defined as the IQE multiplied by the outcoupling efficiency[203]. Therefore, materials with higher EQEs generally perform better in

optoelectronic devices. In order to improve the EQE of a material, either the IQE or the incoupling and outcoupling efficiencies must be improved. The IQE can be enhanced by engineering materials with fewer non-radiative recombination pathways and traps. Whereas, the incoupling and outcoupling efficiencies can be enhanced by reducing parasitic absorption, optimising the device to the photon energies of interest, and by reducing undesirable refractive index effects.

Since the refractive indices of inorganic semiconductors are very high (between ~2-5[206]) compared to the refractive index of air (~1), the probability that a photon will escape an inorganic semiconducting material is reduced by total internal refection (TIR) at the semiconductor-air interface. This means that only photons which approach the semiconductor-air interface at an angle within the escape cone – a small range of incidence angles at which light does not undergo TIR – will escape.

Therefore, in order to reduce TIR and improve the EQE of optoelectronic devices, textured surfaces[207], textured substrates[152], or optical coatings[208] may be used. For example, it has been shown[208] that coating organic light-emitting diodes with thin light scattering layers fabricated from low refractive index scattering centres in high refractive index matrices improves EQEs by up to 65%. It has also been shown[152] that the EQEs of $CH_3NH_3PbI_3$ films can be improved by up to 185% by simply fabricating them on textured substrates rather than planar substrates.

Another approach is to exploit a phenomenon known as photon recycling, the self-absorption and reemission of emitted photons. In this case, a planar film is sufficient as the continual reabsorption and emission of photons has the desired effect of randomising the angles at which photons approach the semiconductor-air interface. Photon recycling occurs in semiconductors, such as GaAs[165,209] and lead halide perovksites[35], with spectrally overlapping sharp absorption onsets and homogeneously phonon-broadened photoluminescence that facilitate the self-absorption and reemission processes[210]. Such semiconductors have high IQEs, exhibiting long carrier lifetimes and low non-radiative losses[35]. These long carrier lifetimes (and therefore long diffusion lengths) are possible despite the high recombination rates observed in these materials because the charge-carrier diffusion length does not limit the average distance a charge carrier travels. Instead, pairs of charge carriers can be reemitted as photons and then reabsorbed again multiple times while propagating over large distances.

The disadvantage of exploiting photon recycling rather than using a textured surface, textured substrate, or optical coating to enhance the EQE is that, unless the semiconducting material has 100% IQE, every time a photon is reabsorbed there is a chance that the photoexcited carriers will interact with a trap or undergo non-radiative recombination. If this happens, the EQE will be reduced. Therefore, materials with over 90% IQE are required[165]. With such materials, it has been shown that the exploitation of photon recycling is an effective strategy for the fabrication of both highly efficient solar cells[35,165] and light-emitting diodes[209].

2.3.4 Power conversion efficiency (PCE)

The PCE of an optoelectronic device describes how efficiently the device converts between optical and electrical power.

For solar cells, the PCE can be defined as the ratio of optical power incident on the device to the electrical power generated by the device. It is typically calculated at the maximum power point of the device using the equation,

$$\mathrm{PCE} = \frac{J_{SC} \cdot V_{OC} \cdot FF}{P_{in}} \qquad 2.31$$

where, J_{SC} is current flowing through the device under short circuit conditions, V_{OC} is the voltage across the device under open circuit conditions, FF is the fill factor of the device (defined as the ratio of the maximum power supplied by the device to the product of the short-circuit current and the open-circuit voltage) and P_{in} is the optical power incident on the device.

For light-emitting diodes, the PCE can be defined as the ratio of the optical power generated by the device to the electrical power supplied to the device. It is typically calculated at the desired brightness of the device using the equation,

$$\mathrm{PCE} = \frac{\Phi_v}{I \cdot V} \qquad 2.32$$

where, Φ_v is the luminous flux emitted by the device (defined as the optical power emitted by the device multiplied by a luminosity function describing the sensitivity of the human eye to different wavelengths of light), I is the current supplied to the device and V is the voltage applied across the device.

3 Experimental Method

In this chapter, we describe the experimental details of the methods used to obtain the data presented in this thesis. This includes all sample fabrication processes, steady state material characterisation techniques and transient material characterisation techniques.

3.1 Materials studied

In this section, we describe all the sample fabrication processes used to collect the data in this thesis. The lead halide perovskite nanocrystals were fabricated by Tom Jellicoe or Nathaniel Davis. The mixed cation lead halide perovskites were fabricated by the group of Michael Grätzel (École Polytechnique Fédérale de Lausanne). The lead halide perovskites containing molecular additives were prepared by the group of Baoquan Sun (Soochow University).

3.1.1 Standard lead halide perovskite films

Standard lead halide perovskite films (bulk $CH_3NH_3PbI_3$, bulk $CH_3NH_3PbBr_3$, and $CsPbI_3$ nanocrystals) were prepared on either fused-silica substrates (Foctek Photonics) or standard microscope cover slips (Academy Science). Substrates were cleaned by sonicating in acetone (Sigma-Aldrich) and then isopropanol (Sigma-Aldrich) for 15 minutes, before being rinsed with isopropanol and then dried with nitrogen. The substrates were further cleaned in an oxygen plasma (Diener electronic) for 10 mins, before immediately being transferred into a nitrogen-filled glovebox for film deposition.

3.1.1.1 $CH_3NH_3PbI_3$ and $CH_3NH_3PbBr_3$ bulk films

$CH_3NH_3PbI_3$ and $CH_3NH_3PbBr_3$ bulk films were prepared using standard procedures[211,212], from either lead chloride or lead acetate precursors (Sigma-Aldrich). All preparation and deposition was carried out in a nitrogen-filled glovebox. Solutions were prepared with final concentrations of ~40 weight percent, by dissolving a 3:1 molar ratio of CH_3NH_3I (Sigma-Aldrich) and either $PbCl_2$ or $Pb(CH_3CO_2)_2$ in anhydrous N,N-Dimethylformamide. Perovskite films were deposited from these solutions by spincoating at 2000 rpm. After spincoating, the deposited films were annealed at 100°C for either 10 minutes if the $Pb(CH_3CO_2)_2$ precursor was used, or 2 hours if the $PbCl_2$ precursor was used.

3.1.1.2 $CsPbI_3$ and $CsPbBr_3$ nanocrystal films

All $CsPbI_3$ and $CsPbBr_3$ perovskite nanocrystals were synthesised by Tom Jellicoe or Nathaniel Davis[213,214] using previously reported procedures[91]. In summary, octadecene and either PbI_2 or $PbBr_2$ (for $CsPbI_3$ and $CsPbBr_3$ perovskite nanocrystals respectively) were placed in a flask and then dried under vacuum. Dried oleylamine and dried oleic acid were injected at 120°C under N_2. Once the PbX_2 salt had completely solubilized, the temperature was raised to between 140-200°C (for smaller or larger nanocrystals respectively). A Cs-oleate solution was rapidly injected and then after a few seconds the reaction mixture was cooled in an ice-water bath. In an argon atmosphere, the nanocrystals were precipitated from solution with anhydrous butanol and centrifuged. The supernatant was discarded and then the nanocrystals were redispersed in anhydrous hexane.

Films were prepared from these $CsPbI_3$ and $CsPbBr_3$ perovskite nanocrystals by either spincoating or drop casting. Spincoated samples were spincoated from a 10 mg/ml nanocrystal solution at 2000 rpm. Dropcasted samples were dropcasted from 40 uL of a 50 mg/mL nanocrystal solution and then after 2 minutes the films were spun at 1500 rpm for 20 s to remove excess solvent.

3.1.2 Mixed cation lead halide perovskites

All mixed cation lead halide perovskites ($APbX_3$ with A = mixtures of CH_3NH_3, $(NH_2)_2CH$, Cs, and Rb and X = a mixture of I and Br) were prepared by the group of Michael Grätzel, at the École Polytechnique Fédérale de Lausanne[59]. All samples were prepared on standard microscope slide (Menzel-Gläser) substrates. The substrates were

first cleaned by sonicating in 2% Hellmanex water solution for 30 minutes, before being rinsed with deionised water and ethanol. Then the substrates were further cleaned with UV ozone treatment for 15 minutes. After cleaning, the substrates were immediately transferred into a glovebox with a nitrogen atmosphere for perovskite deposition.

We use the nomenclature MAPbI, MAPbIBr, MAFAPbIBr, CsMAFAPbIBr and RbCsMAFAPbIBr to refer to the complete perovskite compounds shown in Table 3.1.

Abbreviation	Chemical formula
MAPbI	$MAPbI_3$
MAPbIBr	$MAPb(I_{0.83}Br_{0.17})_3$
MAFAPbIBr	$MAFAPb(I_{0.83}Br_{0.17})_3$
CsMAFAPbIBr	$Cs_{0.05}MAFAPb(I_{0.83}Br_{0.17})_3$
RbCsMAFAPbIBr	$Rb_{0.05}(Cs_{0.05}MAFA)_{0.95}Pb(I_{0.83}Br_{0.17})_3$

Table 3.1 Table of the abbreviations used in this thesis and the corresponding chemical formulae. All mixed cation lead halide perovskite samples were prepared by the group of Michael Grätzel, at the École Polytechnique Fédérale de Lausanne.

These perovskite compounds were prepared from organic cation iodide salts (Dyesol), lead compounds (TCI) and CsI and RbI (abcr) from the following precursor solutions:

- MAPbI and MAPbIBr films were deposited from standard precursor solutions reported in the literature[59,62].
- MAFAPbIBr films were deposited from a precursor solution containing FAI (1 M), PbI_2 (1.1 M), MABr (0.2 M) and $PbBr_2$ (0.22 M) in anhydrous DMF:DMSO 4:1 (v:v).
- CsMAFAPbIBr films were deposited from a precursor solution prepared by first creating a 1.5 M stock solution of CsI in DMF:DMSO 4:1 (v:v) and then by adding this to the MAFAPbIBr precursor solution.
- RbCsMAFAPbIBr films were deposited from a precursor solution prepared by first creating a 1.5 M stock solution of RbI in DMF:DMSO 4:1 (v:v) and then by adding this to the CsMAFAPbIBr precursor solution.

Perovskite films were deposited onto the standard microscope slide substrates from these precursor solutions by spincoating. A two-step program was used, spinning at

1000 rpm for 10 s and then 4000 rpm for 30 s. During the second step, 200 μL of chlorobenzene was dropped onto the spinning substrate 20 s before the end of the program. Then the films were annealed at 100°C for 1 hour in a nitrogen-filled glovebox.

Although the stoichiometric ratios of the solutions are known, the stoichiometric ratios of the fabricated films may not match those of the solutions. Extracting the stoichiometric ratios of the films is challenging and may be attempted using synchrotron-based photoelectron spectroscopy[215].

3.1.3 Additive-controlled lead halide perovskites

All additive-controlled lead halide perovskites ($CsPbBr_3$, $CsPbBr_3$ with phenethylamine bromide, $CsPbBr_3$ with phenethylamine bromide and a -O-C-O- molecule, and $CsPbBr_3$ with phenethylamine bromide, a -O-C-O- molecule, and potassium bromide) were prepared by Muyang Ban under the supervision of Baoquan Sun at Soochow University[8]. The nomenclature PEA, PEABr and -O-C-O- represent phenethylamine, phenethylamine bromide, and a -O-C-O- chemical additive with an electron rich -O-C-O- chemical bond respectively.

PEABr was prepared by adding 6.71 g hydrobromic acid (48 wt% in water, Alfa Aesar) to a solution of phenethylamine (39.8 mmol, Acros) in ethanol (anhydrous, 25 ml, Innochem) while vigorously stirring at 0°C for 2 hours. The PEABr precipitate was obtained by evaporating at 50°C, washing with ethanol three times and then drying under vacuum at 40°C for 24 hours. Solutions were prepared by first dissolving a 1:1 molar ratio of lead bromide ($PbBr_2$) and caesium bromide (CsBr) in dimethyl sulfoxide (Innochem). Then, the required amount of PEABr with or without -O-C-O- was added to the solution at 80°C and stirred continuously for 2 hours. The nomenclature x% indicates the used molar ratio of PEABr to $PbBr_2$ in percent.

Perovskite films were deposited through a two-step spincoating procedure after filtering the prepared solutions through a polytetrafluoroethylene filter (0.45 μm). Spincoating was carried out at 1000 rpm for 5 s and then at 3000 rpm for 55 s. Finally, the films were annealed at 100°C for 1 minute in order to accelerate crystallisation.

3.2 Steady state material characterisation techniques

In this section, we describe all the steady state material characterisation techniques used to collect the data in this thesis. This includes scanning electron microscopy, Raman spectroscopy, x-ray diffraction, steady-state absorption, and photoluminescence quantum efficiency measurements. The scanning electron microscopy measurements were carried out by either Giorgio Divitini or Karl Gödel. The Raman spectroscopy measurements were carried out by Tudor Thomas. The x-ray diffraction measurements were carried out by Tudor Thomas, Tim van de Goor and Edward Booker. The photoluminescence quantum efficiency measurements were carried out by Johannes Richter and Edward Booker.

3.2.1 Scanning electron microscopy (SEM)

Scanning electron microscopy (SEM) is a technique used to image the surface topography of a sample, with around 10 nm resolution.

3.2.1.1 Principles

In order to build up an image, a fine beam of electrons is focused onto the surface of the sample and then scanned across it in a pattern of parallel lines. Typically, these electrons have energies between a few hundred eV to tens of keV. Spatial resolution is achieved because the electrons interact locally with the sample. Within this interaction volume, the incoming electron beam is elastically and inelastically scattered by the sample. These scattered electrons are detected and used to build up an image of the surface topography of the sample. Further details about this technique may be found in the literature[216,217].

3.2.1.2 Procedure

All SEM measurements were carried out by either Giorgio Divitini on a JEOL 5800 LV SEM or by Karl Gödel on a LEO GEMINI 1530VP FEG-SEM. Samples were mounted on conductive carbon tape in order to reduce charging effects and low voltages were used in order to minimise sample degradation.

3.2.2 Raman spectroscopy

Raman spectroscopy is a technique used to probe the vibrational, rotational and other low-frequency modes of a sample.

3.2.2.1 Principles

In order to probe the vibrational, rotational and other low-frequency modes of a system, a laser beam of a single frequency is directed onto a sample. Unlike absorption spectroscopy, where the frequency of the laser beam must match the energy of the particular electronic or vibrational transition of interest, in Raman spectroscopy the frequency of the laser beam does not need to match the energy of any electronic or vibrational transitions. Instead, Raman spectroscopy detects the change in energy of a photon that has undergone Raman scattering with the sample, as shown in Figure 3.1.

Image removed for copyright reasons.

Figure 3.1 Diagram of the elastic Rayleigh scattering and the inelastic Raman scattering processes (Stokes and anti-Stokes) taken from reference 218. *The upward arrows indicate incident photons and the downward arrows indicate scattered photons. The lowest energy vibrational state m and a higher energy vibrational state n are indicated. The energies of the incident photons are significantly larger than the energies of the vibrational states.*

When the laser beam interacts with the sample, it distorts (polarises) the electron cloud around the nuclei, forming an unstable short-lived state known as a virtual state. If only the electron cloud is distorted, the frequency of the scattered photons will be almost identical to the frequency of the incident photons, since only very small amounts of energy are required to displace the comparatively light electrons. This is an elastic scattering process known as Rayleigh scattering. However, if nuclear motion is induced too, a significant and specific amount of energy may be transferred from the incident

photon to the sample (Stokes scattering) or from the sample to the scattered photon (anti-Stokes scattering). These are inelastic scattering processes known as Raman scattering. Raman scattering events are much less likely than Rayleigh scattering events, with only one in 10^6-10^8 incident photons undergoing Raman scattering. For this reason, measurements are carried out with a laser and microscope, in order to achieve the high power densities required.

A spectrum of these specific energies is typically obtained from the Stokes scattering signal, because at room temperature, Stokes scattering events are significantly more likely to occur than anti-Stokes scattering events. This is because the occupation of the vibrational states follows a Boltzmann distribution, with the occupation of lower energy states being more probable than the occupation of higher energy states, and the probability of a particular scattering event depends on the occupation of the initial vibrational state. Further details about these scattering mechanisms and experimental considerations can be found in the literature[218,219].

3.2.2.2 Procedure

All Raman spectroscopy measurements were carried out by Tudor Thomas using previously reported procedures[220]. Stokes Raman spectra were collected using a HORIBA T64000 Raman spectrometer attached to a confocal microscope with a 100× objective. Excitation was performed with 532-nm laser, with the laser power minimized to reduce the possibility of sample degradation. Therefore, several accumulations were required in order to achieve a good signal-to-noise ratio. The spectra were recorded from 50 to 300 cm^{-1}.

3.2.3 X-ray diffraction (XRD)

X-ray diffraction (XRD) is a technique used to extract information about the crystal structure and chemical composition of a sample.

3.2.3.1 Principles

In order to probe the crystal structure and chemical composition of a sample, a monochromatic x-ray beam is directed onto the sample. This x-ray beam interacts with the atoms in the sample and is scattered. Scattering by the nuclei is negligible because the nuclei are too heavy to respond to the rapidly oscillating electromagnetic field. However, it is possible for the rapidly oscillating electromagnetic field to accelerate the

electrons surrounding the nuclei. As the electrons oscillate with the incident x-rays, they isotropically reemit x-rays with the same wavelength and frequency as the incident x-rays. This scattering process is known as Thomson scattering. It is elastic, because the incident and scattered radiation have the same wavelength. It is also coherent, because there is a well-defined phase relationship between the incident and scattered radiation.

For a free electron, the intensity of scattered radiation, $I_{2\theta}$, defined as the power per unit solid angle scattered through a scattering angle of 2θ, is given by Equation 3.1[221].

$$I_{2\theta} = \frac{1}{2}\left(\frac{e^2}{4\pi\epsilon_0 c^2 m}\right)^2 (1 + \cos^2 2\theta) I_0 \qquad 3.1$$

Where e is the charge of an electron, ϵ_0 is the permittivity of free space, c is the speed of light, m is the mass of an electron, 2θ is the scattering angle and I_0 is the intensity of the incident radiation. The intensity of an x-ray beam scattered by an individual atom is extremely small. However, the intensity of several constructively interfering x-ray beams scattered from multiple neighbouring atoms is significant enough to be detected.

The constructive interference of x-rays from neighbouring planes of atoms only occurs under certain conditions. These conditions are specified by Bragg's law (Equation 3.2)[221].

$$2d\sin\theta = \lambda \qquad 3.2$$

Where, d is the distance between two neighbouring planes of atoms, 2θ is the scattering angle and λ is the wavelength of the incident x-ray beam (Figure 3.2). Since constructive interference, and therefore the scattering intensity, is a function of the distance between neighbouring planes of atoms, structural information may be extracted by keeping λ constant and sweeping 2θ. Compositional information may also be extracted, because the scattered intensity from a particular atom is dependent on the electron density and therefore atomic number of that atom. For a scattering angle of zero (2θ = 0), the intensity of an x-ray scattered by an atom with Z electrons is Z times larger than the intensity of an x-ray scattered by a single electron.

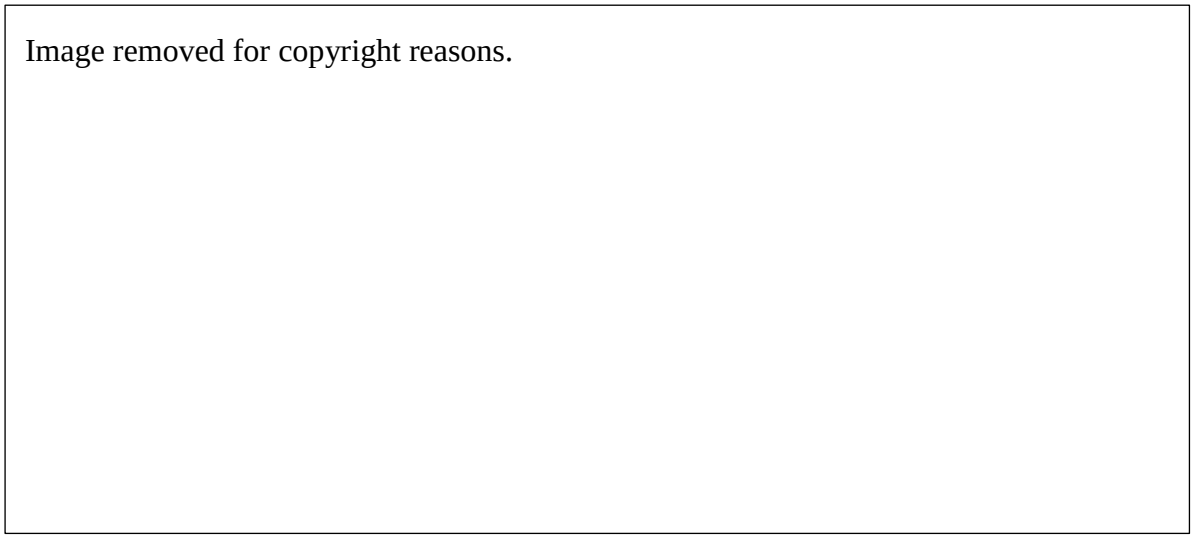

Figure 3.2 Diagram demonstrating Bragg's law taken from reference 221. *Bragg's law is only obeyed when the x-rays reflecting off neighbouring planes of atoms interfere constructively.*

Another type of scattering, known as Compton scattering, may occur when x-rays are incident on a sample. Compton scattering is analogous to a classical hard-sphere collision, in which energy is transferred from an incident x-ray photon to a loosely bound or free electron as kinetic energy. This is an inelastic scattering process, because the scattered x-rays have a longer wavelength (lower energy) than the incident x-rays. It is also an incoherent scattering process, because there is no well-defined phase relationship between the incident and scattered x-rays. For this reason, Compton scattering does not contribute to the diffraction pattern, but does increase the background noise. Further information about the scattering processes involved in XRD and the methods of extracting data from XRD may be found in the literature[221–223].

3.2.3.2 Procedure

All XRD measurements were carried out by Tudor Thomas, Tim van de Goor and Edward Booker using a D8 Advance x-ray diffractometer (Bruker AXS) with a Cu Kα source (0.5418 Å). The incident beam slit width was 0.1 mm. Data was collected in a 1D locked coupled mode for 2θ between 10 and 60 degrees using a step size of 0.0102 degrees with a Bruker Lynx-Eye detector.

3.2.4 Steady-state absorption spectroscopy

Steady state absorption spectroscopy is a technique used to determine the optical density and optical bandgap of a sample.

3.2.4.1 Principles

As discussed in Section 2.2.1, inorganic semiconductors are very useful for a number of different optoelectronic applications because they have optical bandgaps in the UV, visible or NIR part of the electromagnetic spectrum. The energy of this bandgap is obtained using a broadband beam of photons emitted from either a deuterium-discharge lamp (UV) or a tungsten lamp (visible and NIR). First, a background spectrum is collected by collecting the photons transmitted through a blank substrate. Then, a sample spectrum is collected by collecting the photons transmitted through the sample. Photons with an energy equal to or larger than the optical bandgap of the sample may excite an electron from the valence band into the conduction band, reducing the number of photons with these energies being transmitted through the sample. Since the number of photons incident on and transmitted through the sample are known quantitatively for

each photon energy, the OD (as defined in Section 2.2.2.3) can be obtained for each photon energy. Further details may be found in the literature[224,225].

3.2.4.2 Standard procedure

Steady-state absorption spectra were obtained using a Hewlett Packard 8453 ultraviolet-visible spectrometer. Additional counts due to photon scattering were subtracted from the measured spectra.

3.2.4.3 Linear polarisation selective procedure

All steady-state linear polarisation selective absorption measurements were carried out by Roxanne Middleton, using a custom-modified Zeiss Axio A1 optical microscope equipped with a digital CCD camera (IDS UI-3580LE). Each sample was illuminated in transmission from a halogen lamp (Zeiss HAL100). A linear polariser (Zeiss A1 polariser D 427706) in the illumination beam path defined the orientation of the incident polarisation. The incident light was focused through a condenser onto the sample (Zeiss 424225-9001). The transmitted light was coupled into a ×05, NA 0.13 objective (Zeiss EC Epiplan-Neofluar 1156-514). The reflected signal from the sample was filtered by a broadband wire grid linear polariser (Thorlabs WP25M-UB). The polariser was mounted on a motorised rotation stage on the optical path and rotated between the orientation parallel to the incident beam polariser, and perpendicular to it. The central area of ~300um reflected from the illuminated area was coupled into a 600-μm core optical fiber (Avantes FC-UV600) mounted in confocal configuration and measured in a spectrometer (Avantes Avaspec HS2048). Measurement consistency was confirmed by repeating the measurements with the sample manually rotated by 90 degrees.

3.2.5 Photoluminescence quantum efficiency (PLQE)

Photoluminescence quantum efficiency measurements are used to determine the photoluminescence quantum efficiency of a material (as defined in Section 2.2.2.4).

3.2.5.1 Principles

The PLQE of a material is defined as the number of photons emitted by a material to the number of photons absorbed by a material[164]. Therefore, the simplest way to measure the PLQE of a material is in a linear configuration, where the excitation laser is directed into the detector. The PLQE is calculated by measuring the number of photons emitted from the material and diving this by the difference in the number of photons collected

from the excitation laser before and after the sample is placed in the beam path. In non-scattering samples, the difference in the number of photons collected from the excitation laser before and after the sample is placed in the beam path, is a good estimate for the number of photons absorbed by the material. However, in highly scattering samples, an integrating sphere must be used to accurately determine PLQE[164].

An integrating sphere is a hollow sphere with an inside surface coated with a material that reflects light diffusively (typically barium sulphate). Therefore, in an ideal integrating sphere any light emitted or scattered from within the sphere is isotropically redistributed around the sphere. In order to calculate the PLQE of a material using an integrating sphere, three measurements are required (Figure 3.3). First, the excitation laser is directed into the empty integrating sphere. In this measurement, experiment a, the signal from the excitation laser is detected by the spectrometer located at the top of the sphere. Then the excitation laser is directed into the integrating sphere containing the sample, but the excitation laser is directed onto the inside of the integrating sphere and not on the sample. In this measurement, experiment b, the signal from the excitation laser and from the photoluminescence of the sample (arising from the absorption of the excitation laser light scattered around the integrating sphere) is detected. Finally, the excitation laser is directed into the integrating sphere containing the sample, and the excitation laser is directed onto the sample. In this measurement, experiment c, signal is detected again from the excitation laser and from the photoluminescence of the sample, but now the photoluminescence arises from both the absorption of the direct excitation laser light and absorption of the excitation laser light scattered around the integrating sphere. In experiments a, b and c, the signal from the excitation laser becomes increasingly smaller and the signal from the sample photoluminescence becomes increasingly larger.

Image removed for copyright reasons.

Figure 3.3 (A) Diagram of the measurements required to calculate the PLQE of a sample using the integrating-sphere method. (B) Example laser spectrum and PL spectrum obtained from the measurements shown in (A). Both taken from reference 164. *In experiment (a), the excitation laser is directed into the empty integrating sphere. In experiment (b), the excitation laser is directed into the integrating sphere containing the sample, but the excitation laser is directed onto the inside of the integrating sphere and not on the sample. In experiment (c), the excitation laser is directed into the integrating sphere containing the sample, and the laser is directed onto the sample.*

The PLQE (η) is calculated from these measurements using Equation 3.3[164],

$$\eta = \frac{P_c - (1 - A)P_b}{L_a A} \quad 3.3$$

where L_a, L_b and $L_c$are the integrated areas of the laser profiles (which are proportional to the amount of unabsorbed light) and P_a, P_b and P_c are the integrated areas of the emission profiles (which are proportional to the number of emitted photons) in experiments a, b and c respectively. A is the absorption coefficient and is calculated using Equation 3.4.

$$A = \left(1 - \frac{L_c}{L_b}\right) \quad 3.4$$

Using this method, it is possible to measure the PLQEs of solutions and films on different substrates. Further details about calculating PLQE using this integrating-sphere method may be found in the literature[164].

3.2.5.2 Procedure

All PLQE measurements were carried out either by Johannes Richter or Edward Booker, using the integrating-sphere method described above[164]. All samples were excited with a continuous wave MGL-III 532 nm diode-pumped solid-state laser and the corresponding emission was detected using an Andor iDus DU490A InGaAs detector.

3.3 Transient characterisation techniques

In this section, we describe all transient material characterisation techniques used to collect the data in this thesis. This includes transient photoluminescence, collected using time-correlated single photon counting (TCSPC) or an intensified charge-coupled device (ICCD), and transient absorption (TA).

3.3.1 Sample encapsulation

Before carrying out these transient characterisation techniques, all samples were encapsulated in a nitrogen-filled glovebox, in order to reduce the possibility of degradation resulting from oxygen and moisture exposure. A thin-glass cover slip (Academy Science) was placed over each sample and then the edges were sealed with epoxy (Double Bubble, Loctite). In order to reduce interference effects, it was found to

be important to leave a small air gap between the sample and the cover slip. Therefore, small pieces of carbon tape were placed between the sample and the coverslip, just inside the edges of the cover slip, before placing the cover slip onto the sample. After encapsulation, it was possible to characterise the samples in air.

3.3.2 Transient photoluminescence (TPL) spectroscopy

TPL spectroscopy measurements are used to detect the number and wavelength of photons emitted from a material at a given time after photoexcitation. Depending on the lifetime of the emission from the material, measurements are carried out with either time-correlated single photon counting (TCSPC) or an intensified charge-coupled device (ICCD).

3.3.2.1 Time-correlated single photon counting (TCSPC)

TCSPC measurements are used to detect the TPL from materials with photoluminescence lifetimes of between ~100 ps and ~100 ns.

3.3.2.1.1 Principles

TCSPC works on the assumption that the probability distribution of single photon emission following a photoexcitation event, is equal to the total intensity of all photons emitted at different times after the photoexcitation event[226,227]. Therefore, by repeatedly recording the time taken for a single photon to be emitted after a large number of excitation events, photoluminescent lifetimes can be extracted. Data is collected using a trigger, which generates an electrical pulse that is perfectly correlated in time with an optical pulse. At the time of this trigger, a capacitor starts charging and the sample begins to emit photons. These photons pass through a small aperture, which is adjusted so that a maximum of only one photon from each photoexcitation event passes through. As soon as this photon is detected, the capacitor stops charging. The charge on the capacitor, which is proportional to the time delay, is recorded. This is repeated for multiple photoexcitation events in order to build up a histogram of counts in different time bins. The width of these time bins is chosen so that the photoluminescent lifetime of the sample can be measured accurately and efficiently. The measurement is continued until the noise is sufficiently low and a lifetime can be extracted. Since this technique only detects photons of a single wavelength, measurements must be repeated at multiple different wavelengths to build up a map of the photoluminescence against

wavelength and time. Further details about this technique may be found in the literature[226,227].

Image removed for copyright reasons.

Figure 3.4 Diagram of TCSPC, taken from reference 226. *(A) The time between the excitation of the sample with the laser pulse and the emission of a photon is recorded. The experiment is arranged such that less than one emitted photon is detected per laser pulse. (B) This is repeated multiple times in order to build up a histogram.*

3.3.2.1.2 Procedure

All TCSPC measurements were carried out using a monochromator to select the desired photon wavelength and a photomultiplier detector (Hamamatsu R3809U-50). A colour filter and a neutral density filter were placed before the detector to remove pump scatter and reduce the intensity so that no more than a single photon was detected from every ~400 pump pulses respectively. Photoexcitation was performed using ~100 ps pulses centred at ~470 nm with a repetition rate 2.5 MHz (PicoQuant LDH470).

3.3.2.2 Intensified charge-coupled device (ICCD)

ICCD measurements are used to detect the TPL from materials with photoluminescence lifetimes of between ~5 ns and 1 ms.

3.3.2.2.1 Principles

In order to detect the TPL from a material, an ICCD camera is used to detect the number and energy of the photons emitted from the material at a given time after a photoexcitation event. These photons are focused into a spectrometer and then dispersed onto a photocathode, where the incident photons are converted into photoelectrons. These photoelectrons are accelerated towards a microchannel plate - a thin disk consisting of a honeycomb of glass channels with a resistive coating - by applying a high voltage across the microchannel plate. If the applied voltage is large enough, the photoelectrons will have enough energy to dislodge secondary electrons from the microchannel plate. The resulting cloud of electrons continues to be accelerated by the high voltage onto a phosphor screen which is coupled to the CCD. Time-resolved measurements are achieved by rapidly changing the voltage applied across the microchannel plate, so that the photoelectrons are generally prevented from passing through the ICCD except at a given time after photoexcitation when the photoelectrons are rapidly accelerated towards the microchannel plate. During these times, a photoluminescence spectrum is detected. Further details about this technique may be found in the literature[228–230].

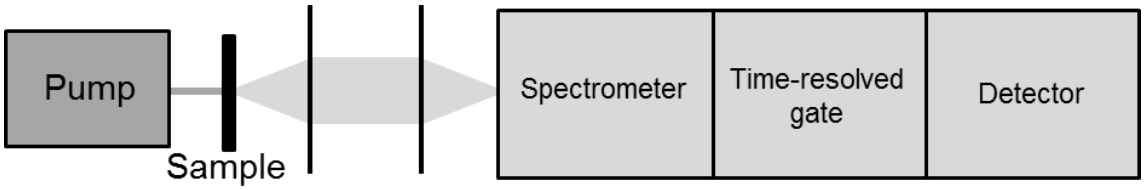

Figure 3.5 Diagram of the ICCD setup. *After photoexcitation with the pump beam, the TPL from the sample is focused into a spectrometer, gated and intensified in an image intensifier tube and then detected.*

3.3.2.2.2 Procedure

All ICCD measurements were carried out using a gated intensified CCD camera system (Andor iStar DH740 CCI-010) connected to a grating spectrometer (Andor SR303i). Photoexcitation was performed using ~90 fs pulses centred at ~400 nm with a repetition rate of ~1 kHz, generated by frequency doubling the output of a Ti:sapphire laser

(Spectra-Physics, Solstice) with a beta barium borate (BBO) crystal. TPL was measured by electronically stepping the gate delay through specified times after photoexcitation. The gate width was 1.5 ns.

3.3.3 Transient absorption (TA) spectroscopy

TA measurements are used to detect the changes in the transmission of a material at a given time after photoexcitation.

3.3.3.1 Principles

In order to measure the changes in the transmission of a material at a given time after photoexcitation, the transmission of the material must be measured before and at a given time after photoexcitation. This is typically achieved using an experimental setup similar shown to the experimental setup shown in Figure 3.6.

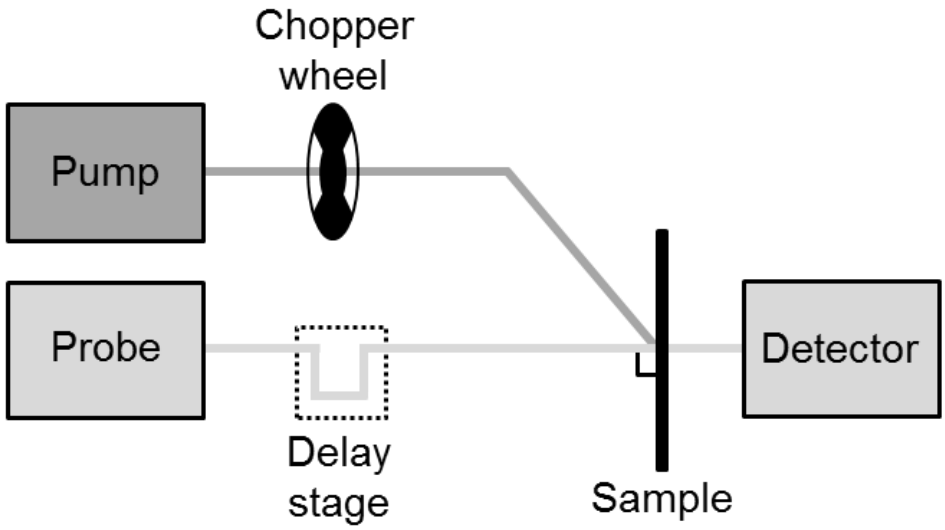

Figure 3.6 Diagram of a typical transient absorption (TA) setup. *The transmission of the probe beam through the sample is detected first with the pump beam blocked by the chopper wheel (**$T_{pump\ off}$**) and then at a given time after photoexcitation (**$T_{pump\ on}$**) with the pump beam passing through the chopper wheel. The time delay between the pump and probe beams is controlled using either a mechanical delay stage or an electronic delay generator.*

First, the transmission of a laser beam – known as the probe beam – through the material before photoexcitation is detected ($T_{pump\ off}$). Then, the transmission of the same laser beam through the material at a given time after photoexcitation with another

laser beam – known as the pump beam – is detected ($T_{pump\ on}$). The time delay between the pump and probe beams is generally generated using a mechanical delay stage for time delays between 10 fs – 2 ns and with an electrical delay generator for time delays longer than 2 ns. From these measurements, the normalised change in transmission $\left(\frac{\Delta T}{T}\right)$ is calculated at a given time after photoexcitation,

$$\frac{\Delta T}{T} = \frac{T_{pump\ on} - T_{pump\ off}}{T_{pump\ off}}. \qquad 3.5$$

A typical example of the TA signal obtained from a standard lead halide perovskite sample is shown in Figure 3.7. Three distinct features are generally observed. The positive feature labelled as A is a ground state bleach (GSB) signal, which arises from phase-space filling by photoexcited carriers[137,138,154,162,163]. The signal is positive because the phase-space filling reduces the absorption and therefore increases the transmission of the probe beam through the sample. Immediately after photoexcitation, the photoexcited charge carrier distribution is centred around the energy of the pump beam. Therefore, the GSB signal is also centred at the energy of the pump beam. Then, rapid carrier scattering processes cause the photoexcited carrier distribution to relax to lower energy states at the band edge. Therefore, the GSB signal also shifts to lower energies, as indicated by the red arrow in Figure 3.7. Finally, the photoexcited charge carrier distribution, and therefore the GSB signal, decay as charge carriers undergo band-to-band recombination. The negative feature labelled as B arises from many-body effects which lead to bandgap renormalisation[137,154] and the negative feature labelled as C arises from photo-induced refractive index changes[137,154].

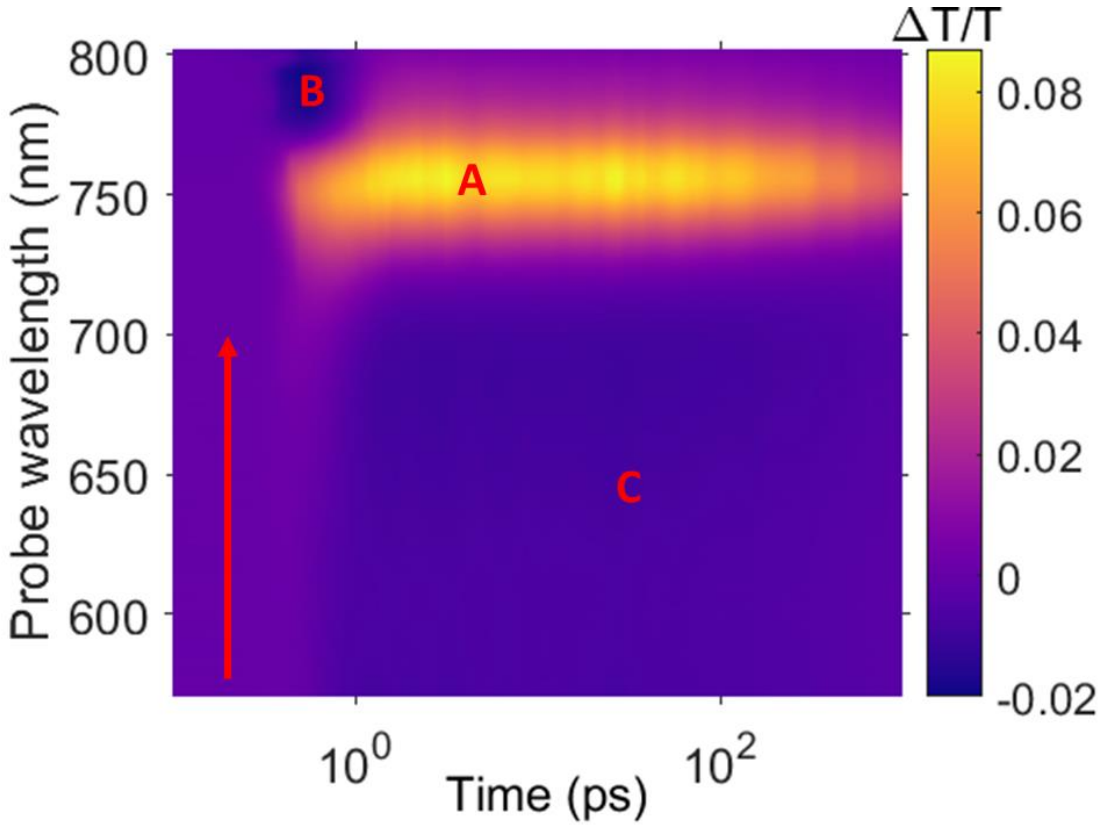

Figure 3.7 Normalised change in transmission as a function of probe wavelength and time after photoexcitation for a standard $CH_3NH_3PbI_3$ perovskite sample. *Signals A, B and C arise from ground state bleaching (GSB), bandgap renormalisation and photo-induced changes in refractive index respectively. Immediately after photoexcitation, the GSB signal shifts from higher to lower energies, as indicated by the red arrow. The sample was excited with a 532 nm laser (500 Hz repetition rate, ~90 fs pulse duration, ~25 meV FWHM) with excitation density ~10^{18} cm^{-3}.*

3.3.3.2 Procedure

All TA measurements were carried out using probe beams generated from a Ti:sapphire laser (Spectra-Physics, Solstice) which produces ~90 fs pulses centred at ~780 nm with a repetition rate of ~1 kHz and an output power of ~3.5 W. The probe beams were generated in a non-collinear optical parametric amplifier (NOPA)[231–233], as shown in Figure 3.8, by taking a fraction of the main laser output (~350 mW) and then splitting it into high power beam (~300 mW) and a low power beam (~500 μW). The low power beam was tightly focused onto a 2 mm thick sapphire plate (UQG Optics, WSR-252), in order to generate an ultrabroadband seed pulse through supercontinuum generation[234,235]. Meanwhile, the high power beam was frequency doubled to 400 nm in a beta barium borate (BBO) crystal (INGCRYS Laser Systems, thickness = 0.2 mm, θ = 29.2°). Both the low and high power beams were then focussed onto another beta barium borate (BBO) crystal (INGCRYS Laser Systems, thickness = 2 mm, θ = 29.9°) in a non-collinear geometry, with an angle between the beams of 3.7°. When the beams are spatially and temporally overlapped, the ultrabroadband seed is amplified over a broad wavelength range (typically ~500-700 nm). In order to increase the spectral broadness of the probe, only reflective optics were used in the low power beam paths and the high power beams were temporally stretched by passing them through a 10 cm fused quartz rod (UQG Optics, QRL-110).

Image removed for copyright reasons.

Figure 3.8 Diagram of a non-collinear optical parametric amplifier (NOPA), taken from reference 236, and a schematic of optical parametric amplification, taken from reference 231. *(A) Amplified broadband pulses are generated from the monochromatic output of a Ti:sapphire laser. (B) In a non-linear crystal, typically beta barium borate (BBO), power is transferred from a high energy and high intensity pump beam into a lower energy and lower intensity signal beam. (C) The signal beam is amplified through the stimulated emission of signal photons from a virtual level excited by the pump photons. In order to obey energy conservation, a third beam (known as the idler) is also generated.*

The problem with generating probe beams using a NOPA, is that the intensity of the beams can have shot-to-shot variations of up to 10% under normal operating conditions[237]. This is a problem because the normalised change in transmission $\left(\frac{\Delta T}{T}\right)$ signals (which are typically less than 0.1%) are calculated from sequential measurements before and at a given time after photoexcitation. Therefore, correcting for these large variations in probe intensity can significantly improve the signal to noise ratio of the measured TA signal and speed up data collection. This is achieved by splitting the probe into two identical beams, known as the probe and reference beams. The transmission of both the probe and reference beams through the sample is detected, but only the probe beam is spatially and temporally overlapped with the pump beam. The reference beam is simply used to correct for the shot-to-shot variations in the intensity of the probe beam.

All measurements were carried out using probe and reference beams, which were focused into a spectrometer (PI Acton Spectrapro 2150i) and then dispersed onto a pair of spatially separated 256-pixel photodiode arrays (Hamamatsu S3901256Q). The signal from these arrays was read out using a Hamamatsu C7844 card, digitised with a National Instruments PXI-6122 analogue-to-digital conversion card, and then acquired (National Instruments PXI-1002). All data collection was controlled with LabVIEW and the normalised change in transmission $\left(\frac{\Delta T}{T}\right)$ was calculated from the probe and reference signals before and at a given time after photoexcitation using Equation 3.6.

$$\frac{\Delta T}{T} = \frac{\frac{T_{on\,(probe)}}{T_{on\,(reference)}} - \frac{T_{off\,(probe)}}{T_{off\,(reference)}}}{\frac{T_{off\,(probe)}}{T_{off\,(reference)}}} \qquad 3.6$$

The pump beams were generated in a NOPA – for measurements requiring < 50 fs time resolution – or a commercial travelling-wave optical parametric amplifier of superfluorescence (Light Conversion, TOPAS) – for measurements requiring ~150 fs time resolution – when the normalised change in transmission was collected within the first ~2 ns after photoexcitation. In this case, the time delay was generated with a mechanical delay stage (Newport, controller: XPS-C8, stage: M-IMS300CCHA). The stage was aligned using a beam profiler (Thorlabs, BC106N-VIS/M) so that the position of the probe beam at the sample deviated by < 10 μm, which was significantly smaller

than the typical probe beam spot sizes of 100-200 μm and the typical pump beam spot sizes of 500-1000 μm. The pump beam spot size was always chosen to be larger than the probe beam spot size to minimise artefacts due to delay stage misalignment and to achieve a uniform excitation density. The T_{on} and T_{off} signals were distinguished by modulating the 1 kHz pump beam to 500 Hz by blocking alternate pulses with an optical chopper (ThorLabs, MC1000A).

When the normalised change in transmission was collected after the first ~2 ns after photoexcitation, it was no longer feasible to use a mechanical delay stage, so the pump beams were generated from the frequency doubled (532 nm) or tripled (355 nm) emission from a 1064 nm q-switched pulsed laser (Advanced Optical Technologies AOT-YVO-25QSPX). In this case, the time delay was generated using an electronic delay generator (Stanford Research Systems DG535) and the T_{on} and T_{off} signals were distinguished by triggering the laser with a 500 Hz signal generated by frequency dividing the 1 kHz clock pulse from the Ti:sapphire laser.

In both cases, the linear polarisations of the pump and probe beams were aligned at the magic angle (54.7°) to reduce optical orientation effects, except when these optical orientation effects were studied using the linear polarisation selective transient absorption measurements described in detail in the next chapter.

4 Polarisation anisotropy in lead halide perovskites

In this chapter, we use linear polarisation selective transient absorption spectroscopy (LPTA) to probe changes in the electronic properties of $CH_3NH_3PbI_3$, $CH_3NH_3PbBr_3$ and $CsPbI_3$ lead halide perovskites arising from dynamic fluctuations in the crystal lattice. We find that lead halide perovskites maintain a pump induced anisotropy for several picoseconds after photoexcitation, which is independent of crystal size and A-site cation. The lifetime of this anisotropy is significantly longer than reported carrier scattering timescales in these materials. First-principles calculations suggest that this anisotropy arises from an intrinsic anisotropy in the transition dipole moment, which depends on the orientation of light polarisation and polar distortion of the crystal. The anisotropy seems to decay because of dynamic variations in the optical transitions, which occur on the time-scales of structural motion. These observations suggest that the photophysics of lead halide perovskites are a hybrid of organic photophysics and inorganic photophysics, requiring a new interpretation of recombination and transport mechanisms. The first-principles calculations in this chapter were carried out by Liang Tan in the group of Andrew Rappe at the University of Pennsylvania and the $CsPbI_3$ lead halide perovskite nanocrystals were synthesised by Tom Jellicoe and Nathaniel Davis. All SEM images were obtained by Karl Gödel and Giorgio Divitini.

4.1 Background and motivation

Since the first lead halide perovskite solar cell was fabricated in 2009, with a power conversion efficiency of only 3.8%[5], intense research on these materials has led to them becoming the fastest-advancing solar technology in the world. Now the record lead halide perovskite devices have certified power conversion efficiencies exceeding 22%[6].

It has been suggested in the literature that the excellent photovoltaic performance of lead halide perovskites originates from the hybrid nature of the crystal structure[53,238–240], where the band structure and carrier-lattice coupling give rise to a range of novel photophysical properties. These studies suggest that lead halide perovskites seem to lie between the extremes of highly-ordered, crystalline semiconductors – which can exhibit ballistic charge transport – and disordered, molecular semiconductors – where strong electron-phonon coupling leads to highly localised excited states.

However, research into the role of lattice distortion and the coupling between charge carriers and lattice phonons, which is key to understanding the physics of these materials, is only now beginning[42,135,241]. It has been suggested that the formation of large polarons, arising from the deformation of the lead halide lattice, could be one explanation for the excellent optoelectronic properties of these materials[240,242]. Another suggestion is that the combined effects of the strong spin-orbit coupling and the local electric fields generated in the non-centrosymmetric crystal lattice[52,243,244] give rise to Rashba-type symmetry breaking in carrier momentum space[48,50,51,53,197]. Such Rashba-type symmetry breaking has been observed at low temperatures, but a large range of splitting energies have been reported (4-240 meV)[245,50]. It is believed that this Rashba-type splitting could be the origin of the low recombination rates observed in lead halide perovskites, because of the formation of an indirect bandgap and spin-forbidden transitions[53,126,246]. Other studies suggest that the low recombination rates arise from the spatial separation of the electron and hole over different regions of the perovskite unit cell[32], trapping and detrapping from a reservoir of dark states[124], or from molecular rotations, which cause dynamical changes in the perovskite band structure[238].

Gaining further insight into how these processes affect the optoelectronic properties of standard $CH_3NH_3PbI_3$, $CH_3NH_3PbBr_3$ and $CsPbI_3$ lead halide perovskites, by using linear polarisation selective transient absorption (LPTA), is important for further improvements in device performance and will therefore be the focus of this chapter.

4.2 Preparation of lead halide perovskite films

Standard $CH_3NH_3PbI_3$ and $CH_3NH_3PbBr_3$ bulk films were prepared using the procedure described in detail in Section 3.1.1.1. The $CH_3NH_3PbI_3$ films were prepared from either a lead acetate ($Pb(CH_3CO_2)_2$) or a lead chloride ($PbCl_2$) precursor, but in both cases the resulting films have the chemical formula $CH_3NH_3PbI_3$, as no traces of acetate or chloride can be detected in the annealed films[212,247]. Using different precursors simply changes the film morphology. Throughout this chapter we use the nomenclature $CH_3NH_3PbI_3$ (acetate) and $CH_3NH_3PbI_3$ (Cl) to refer to $CH_3NH_3PbI_3$ bulk films prepared from lead acetate and lead chloride precursors respectively. Standard $CsPbI_3$ nanocrystal films were prepared by Tom Jellicoe and Nathaniel Davis using the procedure described in detail in Section 3.1.1.2. Images of the films obtained using scanning electron microscopy (SEM) are shown in Figure 4.1. All samples were encapsulated in a nitrogen atmosphere, using the method described in detail in Section 3.3.1, before transient absorption measurements were carried out.

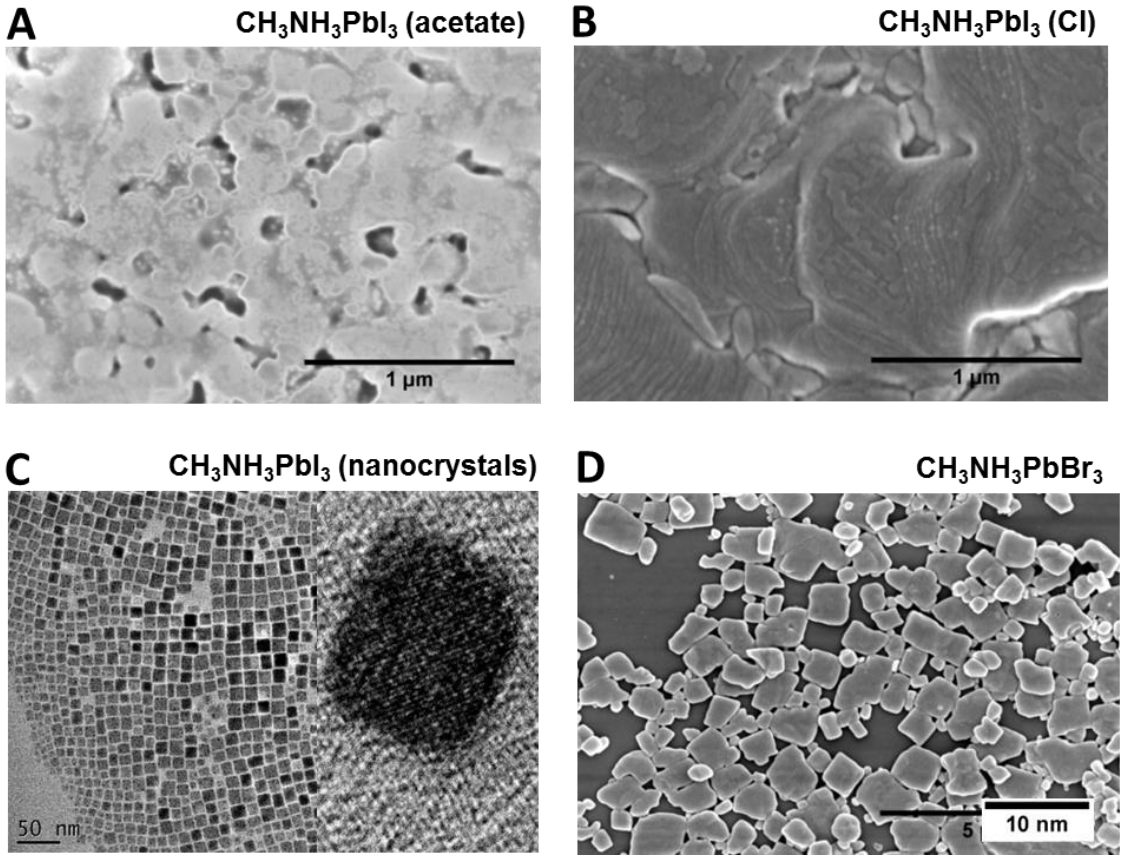

Figure 4.1 Scanning electron microscopy (SEM) images of standard lead halide perovskites. *The (A) $CH_3NH_3PbI_3$ (acetate) and (B) $CH_3NH_3PbI_3$ (Cl) bulk films are continuous, with polycrystalline domain sizes of a few 100 nm and a few micrometres respectively. The (C) $CsPbI_3$ nanocrystal film consists of cubic nanocrystals with an average size of ~14 nm. The (D) $CH_3NH_3PbBr_3$ bulk film consists of grains with an average size of a few 100 nm. All SEM images were obtained by Karl Gödel and Giorgio Divitini.*

4.3 Linear polarisation selective steady-state absorption of lead halide perovskite films

In order to confirm that the prepared samples were representative of those investigated in previous literature and to ensure that the samples had no intrinsic anisotropy, linear polarisation selective steady-state absorption was carried out using the method described in detail in Section 3.2.4. Absorption spectra of the $CH_3NH_3PbI_3$, $CH_3NH_3PbBr_3$ bulk films and $CsPbI_3$ nanocrystal films obtained through parallel and crossed polarisers are shown in Figure 4.2. The absorption spectra are comparable to those found in the literature[125,91] and no intrinsic anisotropy is observed. The $CH_3NH_3PbI_3$, $CH_3NH_3PbBr_3$ bulk films and the $CsPbI_3$ nanocrystal film have optical bandgaps of 1.6 eV, 2.3 eV and 1.8 eV respectively.

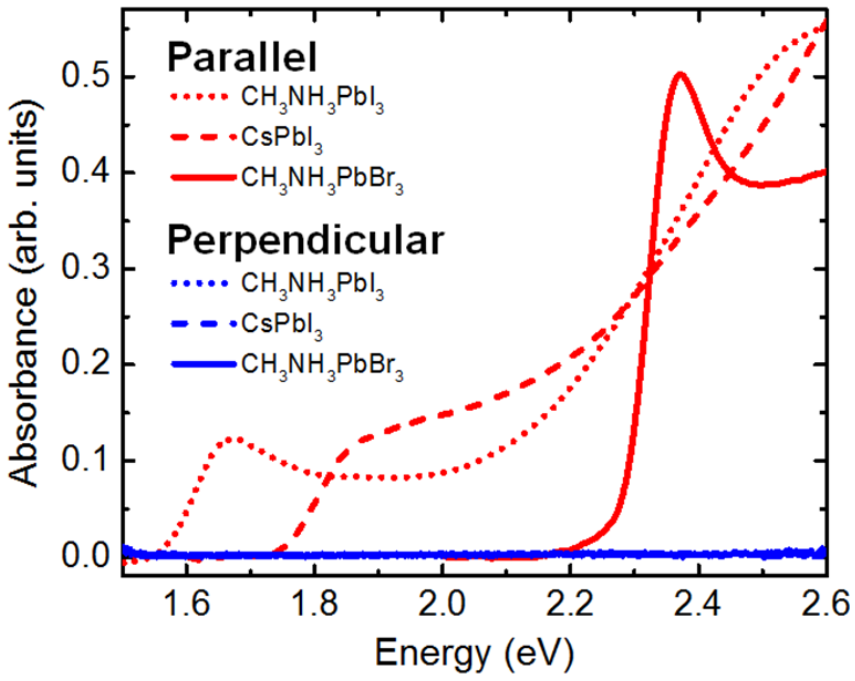

Figure 4.2 Linear polarisation selective steady-state absorption of standard perovskite films. *The absorption spectra obtained through parallel polarisers (red) are comparable to those found in the literature*[125,91]*. The absorption spectra obtained through crossed polarisers (blue) are zero, indicating that the samples have no intrinsic anisotropy.*

4.4 Linear polarisation selective transient absorption (LPTA) of lead halide perovskite films

In order to determine whether lead halide perovskites exhibit a dynamic anisotropy and to investigate the properties of this dynamic anisotropy, we carried out LPTA on standard $CH_3NH_3PbI_3$, $CH_3NH_3PbBr_3$ bulk films and $CsPbI_3$ nanocrystal films. LPTA is very similar to standard TA, which is described in detail in Section 3.3.3, but is carried out with four additional polarisers (Thorlabs, LPVISE2X2 and WP50L-UB) and two half-wave plates (Thorlabs, AHWP10M-600). A diagram of the LPTA setup is shown in Figure 4.3. This arrangement avoids artefacts arising from changes in the probed sample position and changes in the excitation density[248].

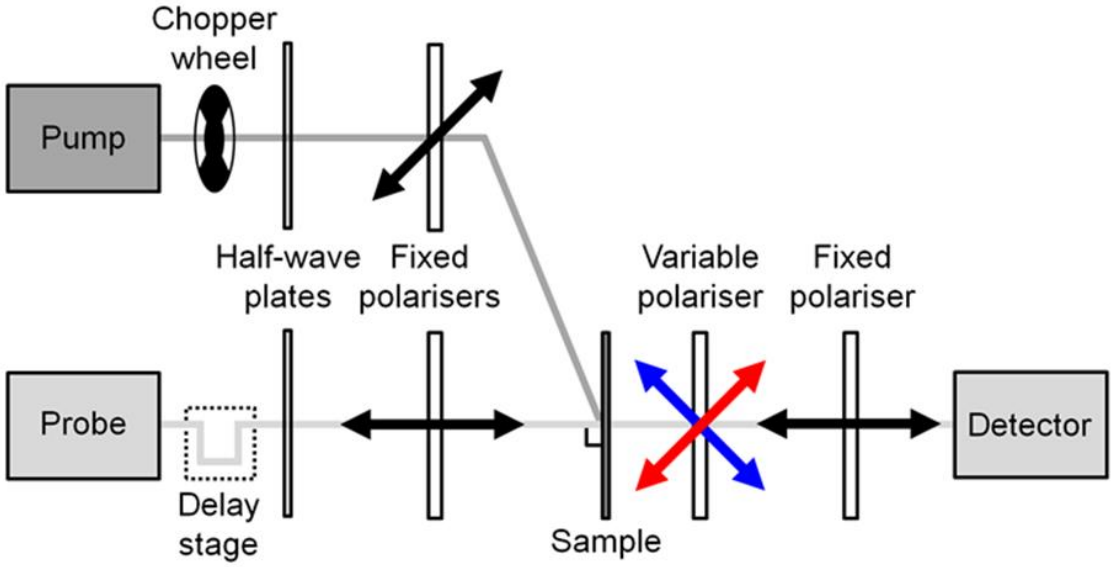

Figure 4.3 Diagram of the linear polarisation selective transient absorption (LPTA) setup. *The linear polarisation of the pump beam is set at an angle of 45° to the linear polarisation of the probe beam before the sample. A second set of polarisers after the sample detect the linear polarisation component of the probe beam either parallel or perpendicular to the pump beam polarisation direction.*

Samples were excited with narrowband linearly polarised pump pulses (~25 meV FWHM, pulse duration <50 fs) at energies between 10 and 200 meV above the optical bandgap, and probed after a variable time delay with broadband linearly polarised probe pulses (1.55-2.55 eV, pulse duration ~100 fs). The relative polarisation between the pump and probe pulses was varied by changing the variable polariser directly after the sample. For each relative polarisation, the transmission of the probe pulse through the

sample was measured with (T_{on}) and without the pump pulse (T_{off}) and the relative change in transmission was calculated using Equation 4.1.

$$\frac{\Delta T}{T} = \frac{T_{on} - T_{off}}{T_{off}} \qquad 4.1$$

4.4.1 Femtosecond LPTA of lead halide perovskite films

Typical LPTA spectra obtained within the first 200 fs after photoexcitation are shown in Figure 4.4, for a $CH_3NH_3PbI_3$ bulk film photoexcited with a 1.72 eV pump pulse.

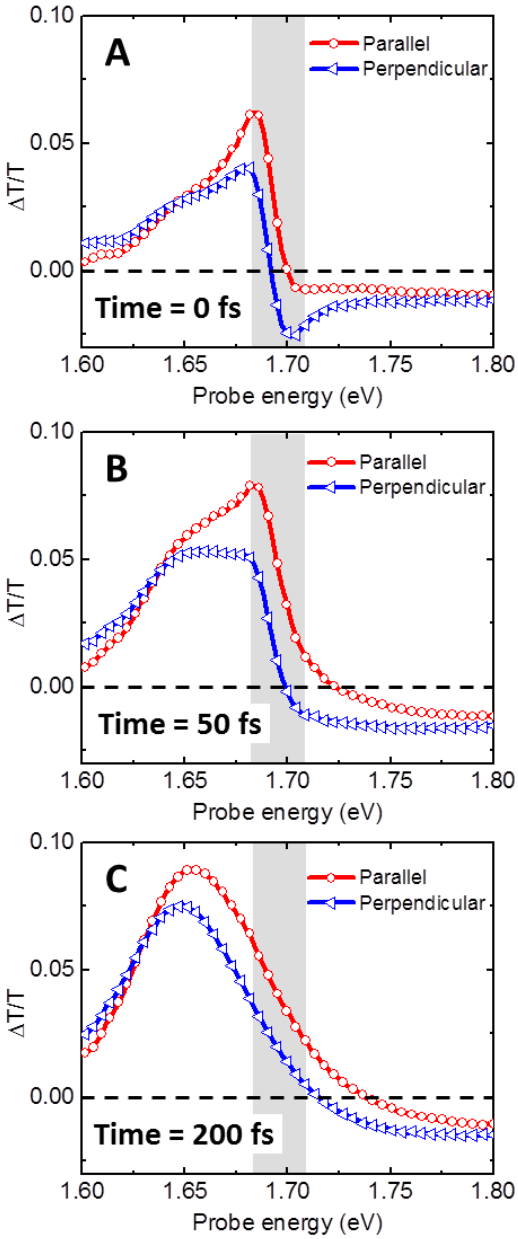

Figure 4.4 LPTA spectra for a $CH_3NH_3PbI_3$ bulk film within the first 200 fs after photoexcitation. *The change in the transmission of the probe was measured at (A) 0 fs (B) 50 fs and (C) 200 fs after photoexcitation with the linear polarisation of the probe pulse aligned either parallel (red) or perpendicular (blue) to the linear polarisation of the pump pulse. We observe a stronger increase in the transmission when the pump and probe pulse polarisations are aligned parallel. The differences observed in the transient spectral dynamics indicate that the carrier populations probed in parallel and perpendicular configurations undergo different relaxation processes. The sample was excited with a 1.72 eV laser (1 kHz repetition rate, ~50 fs pulse duration, ~25 meV FWHM indicated by shaded area) with an intensity of ~20 μJ cm^{-2}.*

Immediately after photoexcitation (0 fs), we observe a strong positive signal close to the excitation energy in both polarisation configurations. This is a positive ground state bleach (GSB) signal, which arises from phase-space filling by photoexcited carriers [137,138,162,163]. The weak tail of this GSB extends towards the band edge at 1.64 eV. This indicates that only small fraction of carriers have started to thermalise. Most carriers are still non-thermal and have not yet scattered with other carriers and phonons. The signal in the parallel configuration is stronger than the signal in the perpendicular configuration, indicating that the parallel probe interacts with either a larger carrier population, or the excited carrier population exhibits different transition dipole matrix elements (TDMEs) for different linear polarisation directions. This is the first indication that the symmetry in the optical properties is broken by the linear polarisation of the pump pulse.

At later time delays (50 fs), the signal in the perpendicular configuration is strongly broadened towards the band edge, indicating that these carriers have thermalised further and started to cool. Unexpectedly, the signal in parallel configuration remains rather localised at energies close to the excitation energy (indicated by shaded area). This suggests that the carrier population probed in parallel configuration undergoes slower relaxation than the carrier population probed in perpendicular configuration. The signal in the parallel configuration is still stronger than the signal in the perpendicular configuration and neither the parallel nor the perpendicular carrier distributions have fully thermalised.

At even later time delays (200 fs), the LPTA spectra indicate that the carrier distributions probed in both the parallel and perpendicular configurations have evolved into fully thermalised Fermi-Dirac distributions. However, the signal probed in perpendicular configuration maintains a different spectral shape and a 30% lower signal intensity than the signal probed in the parallel configuration. These persistent differences in signal intensity and shape suggest that the initial anisotropy is preserved through thermalisation and cooling processes, such as carrier-carrier and carrier-lattice scattering.

4.4.2 Picosecond LPTA of lead halide perovskite films

Typical LPTA spectra obtained between 1-10 ps after photoexcitation are shown in Figure 4.5, for a $CH_3NH_3PbI_3$ bulk film photoexcited with a 1.72 eV pump pulse and a $CsPbI_3$ nanocrystal film photoexcited with a 1.90 eV pump pulse.

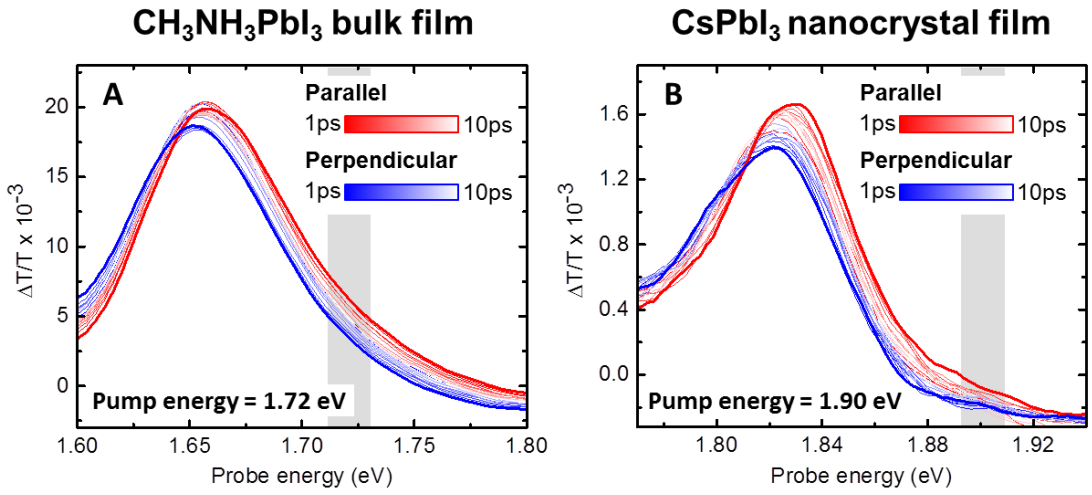

Figure 4.5 LPTA spectra for a $CH_3NH_3PbI_3$ bulk film and a $CsPbI_3$ nanocrystal film between 1-10 ps after photoexcitation. *The change in transmission of the probe through the (A) $CH_3NH_3PbI_3$ bulk film and the (B) $CsPbI_3$ nanocrystal film was measured at the indicated time delays with the linear polarisation of the probe pulse aligned parallel (red) or perpendicular (blue) to the linear polarisation of the pump pulse. The initially polarisation-dependent spectra converge within the first ~10 ps after photoexcitation. The $CH_3NH_3PbI_3$ sample was excited with a 1.72 eV laser with an intensity of ~15 μJ cm^{-2}. The $CsPbI_3$ sample was excited with a 1.90 eV laser with an intensity of ~4 μJ cm^{-2}. Both lasers had a 1 kHz repetition rate, ~50 fs pulse duration and ~25 meV FWHM indicated by the shaded areas.*

In both the $CH_3NH_3PbI_3$ bulk film and the $CsPbI_3$ nanocrystal film, the GSB signal is higher in the parallel configuration than in the perpendicular configuration and the spectral shapes are different. In the parallel configuration, the GSB signal is higher at high energies and lower at low energies than the GSB signal observed in the perpendicular configuration. These differences in spectral shape and intensity reduce over time, converging to an intermediate spectrum within ~10 ps after photoexcitation.

In order to understand how the differences in the parallel and perpendicular signals evolve in probe energy and delay time t, we define an anisotropy $A(t)$ as shown in Equation 4.2.

$$A(t) = \frac{\left(\frac{\Delta T}{T}\right)_{\parallel}(t) - \left(\frac{\Delta T}{T}\right)_{\perp}(t)}{\left(\frac{\Delta T}{T}\right)_{\parallel}(t) + 2\left(\frac{\Delta T}{T}\right)_{\perp}(t)} \qquad 4.2$$

Maps of the anisotropy for the $CH_3NH_3PbI_3$ bulk film photoexcited with the 1.72 eV pump pulse and the $CsPbI_3$ nanocrystal film photoexcited with the 1.90 eV pump pulse are shown in Figure 4.6.

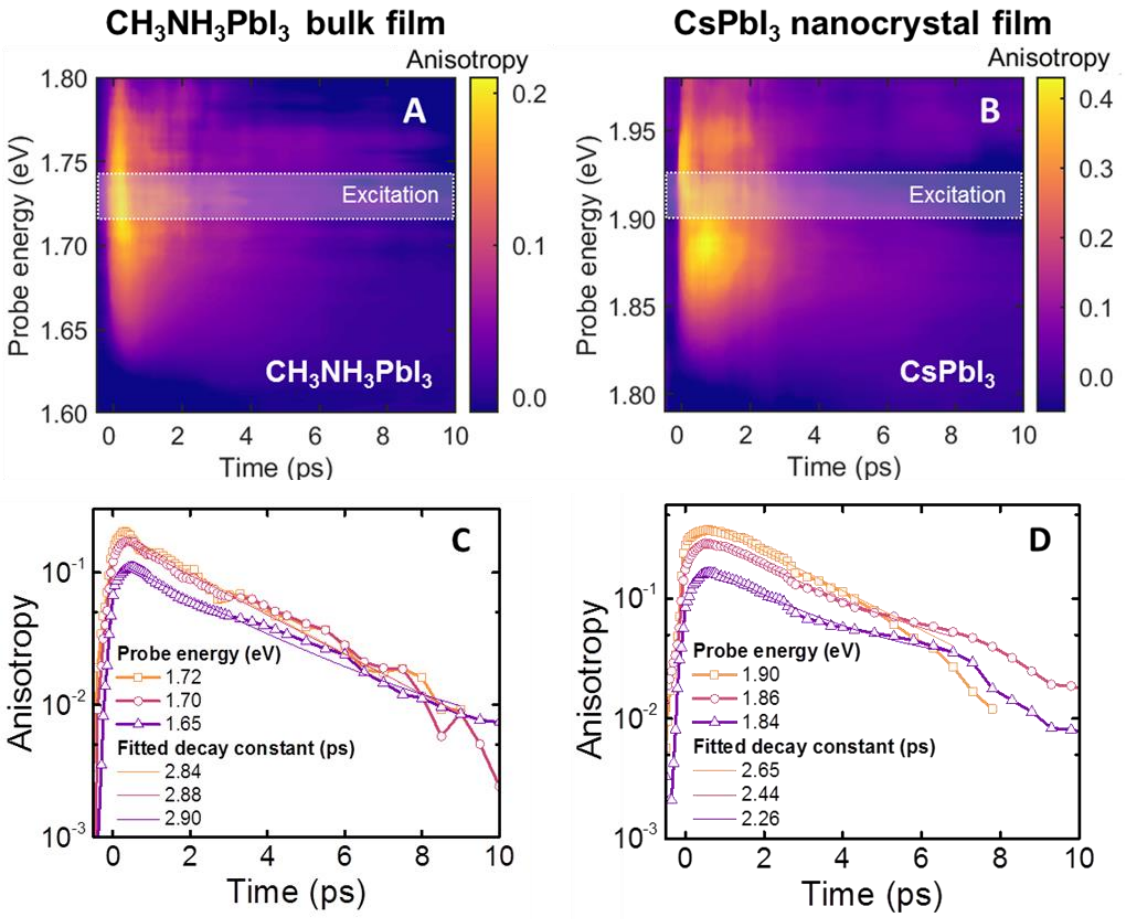

Figure 4.6 LPTA anisotropy maps for a $CH_3NH_3PbI_3$ bulk film and a $CsPbI_3$ nanocrystal film within the first 10 ps after photoexcitation. *During the first 10 ps after photoexcitation, the anisotropy in (A) $CH_3NH_3PbI_3$ and (B) $CsPbI_3$ shifts to lower energy states closer to the band minima. After an initial relaxation, the anisotropy kinetics of (C) $CH_3NH_3PbI_3$ and (D) $CsPbI_3$ decay with time constants of 2.85 ± 0.1 ps and 2.45 ± 0.2 ps respectively. No significant variation in this decay time is found for different probe energies.*

Immediately after photoexcitation, the anisotropy is largest near the pump energy in both the $CH_3NH_3PbI_3$ bulk and $CsPbI_3$ nanocrystal films. Within the first picosecond after excitation, the anisotropy maximum relaxes towards lower energy states at the band edge. The following decay of the anisotropy after thermalisation can be fitted with a single-exponential decay with a lifetime of 2.85 ± 0.1 ps in the $CH_3NH_3PbI_3$ bulk film and 2.45 ± 0.2 ps in the $CsPbI_3$ nanocrystal film. No significant variation in these decay time is found for other probe energies, which suggests that the loss of the photoexcited anisotropy occurs through a common process for all states. These timescales are much longer than typical phonon emission[249–251] and carrier cooling times[137,141,163], but are in agreement with reported timescales for dynamic fluctuations of the crystal lattice[241,47]. This indicates that the origin of the anisotropy is connected with the crystal conformation, rather than a particular carrier-phonon interaction. The similarity of the timescales, independent of crystallite size, suggests that the observed anisotropy is not lost through grain boundary scattering or diffusion between crystallites[198,199], but originates on considerably smaller length-scales.

4.4.3 Effect of crystallite size and crystallite packing on the polarisation anisotropy

In order to further investigate whether the lifetime of the anisotropy was dependent on the crystal size and packing, we extracted the LPTA kinetics of the GSB signal measured in the $CH_3NH_3PbI_3$ (acetate) bulk film, the $CH_3NH_3PbI_3$ (Cl) bulk film and the $CsPbI_3$ nanocrystal film. We also reconstructed the population kinetics $n(t)$ as a function of delay time t from the LPTA kinetics obtained in the parallel $\left(\frac{\Delta T}{T}\right)_{\parallel}$ and perpendicular $\left(\frac{\Delta T}{T}\right)_{\perp}$ configurations using Equation 4.3, by assuming that the charge carriers move freely in three-dimensional space.

$$n(t) = \frac{\left(\frac{\Delta T}{T}\right)_{\parallel}(t) + 2\left(\frac{\Delta T}{T}\right)_{\perp}(t)}{3} \qquad 4.3$$

The LPTA and population kinetics and shown in Figure 4.7. In all samples, the LPTA kinetics converge over timescales of around ~10 ps after photoexcitation. Since the population kinetics do not decay on these timescales, recombination is negligible, as expected at these excitation densities[153], and therefore cannot be the origin of the anisotropy decay. It is also unlikely that interactions between carriers cause the

anisotropy decay, since the excitation density in the nanocrystal film was lower than the density of nanocrystals, such that each nanocrystal contained no more than a single photoexcited charge carrier pair. We can also rule out the possibility that the anisotropy originates from rotation of the organic cation[45–47,56,238], since we also observe an anisotropy in $CsPbI_3$ films.

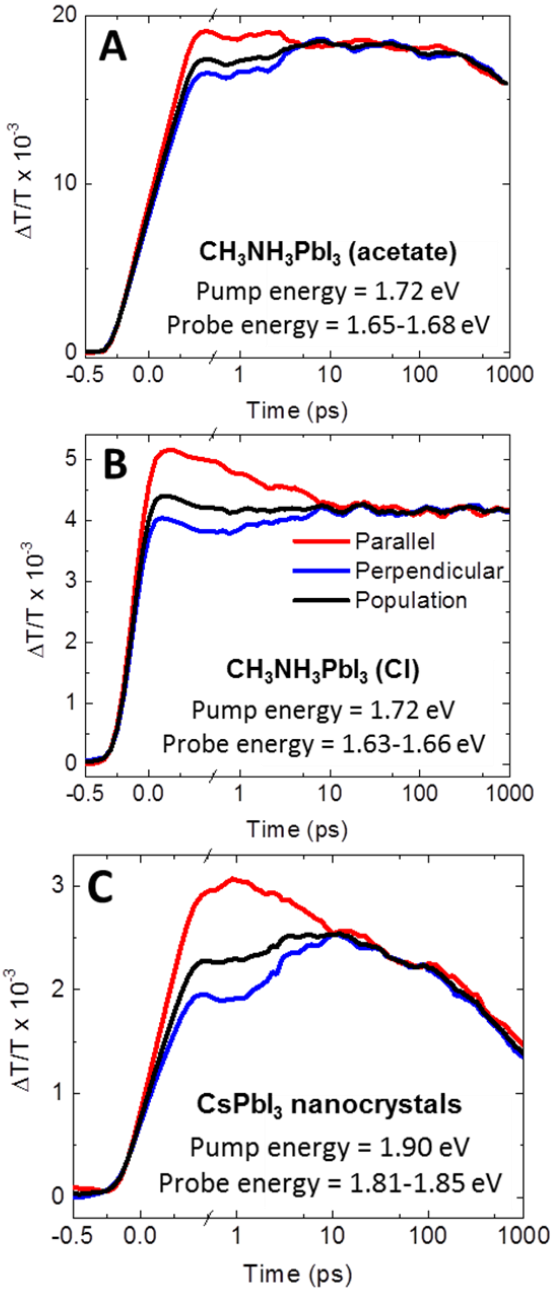

Figure 4.7 LPTA and population kinetics of standard lead halide perovskites. *LPTA kinetics of (A) $CH_3NH_3PbI_3$ (acetate) bulk film, (B) $CH_3NH_3PbI_3$ (Cl) bulk film and (C) $CsPbI_3$ nanocrystal film excited with lasers of in intensity ~16 μJ cm^{-2}, ~2 μJ cm^{-2}, ~3 μJ cm^{-2} respectively. LPTA kinetics were measured with the linear polarisation of the probe pulse aligned either parallel (red) or perpendicular (blue) to the linear polarisation of the pump pulse. The population kinetics (black) were calculated from the parallel* $\left(\frac{\Delta T}{T}\right)_{\parallel}$ *and perpendicular* $\left(\frac{\Delta T}{T}\right)_{\perp}$ *data using Equation 4.3. The initially polarisation-dependent kinetics converge within the first 10 ps after photoexcitation.*

The fact that the LPTA kinetics converge on the same timescales in the $CH_3NH_3PbI_3$ (acetate) bulk film, the $CH_3NH_3PbI_3$ (Cl) bulk film and the $CsPbI_3$ nanocrystal film, which have very different crystallite sizes and crystallite packing, indicate that the observed anisotropy has a fundamental origin beyond the macroscopic crystal structure and does not decay by diffusion between crystallites. Further evidence for this is that the anisotropy maps of the $CH_3NH_3PbI_3$ (acetate) bulk film, the $CH_3NH_3PbI_3$ (Cl) bulk film and the $CsPbI_3$ nanocrystal film are qualitatively the same, as shown in Figure 4.8, and that a similar effect is also observed in $CH_3NH_3PbBr_3$ bulk films[252], as shown in Figure 4.9.

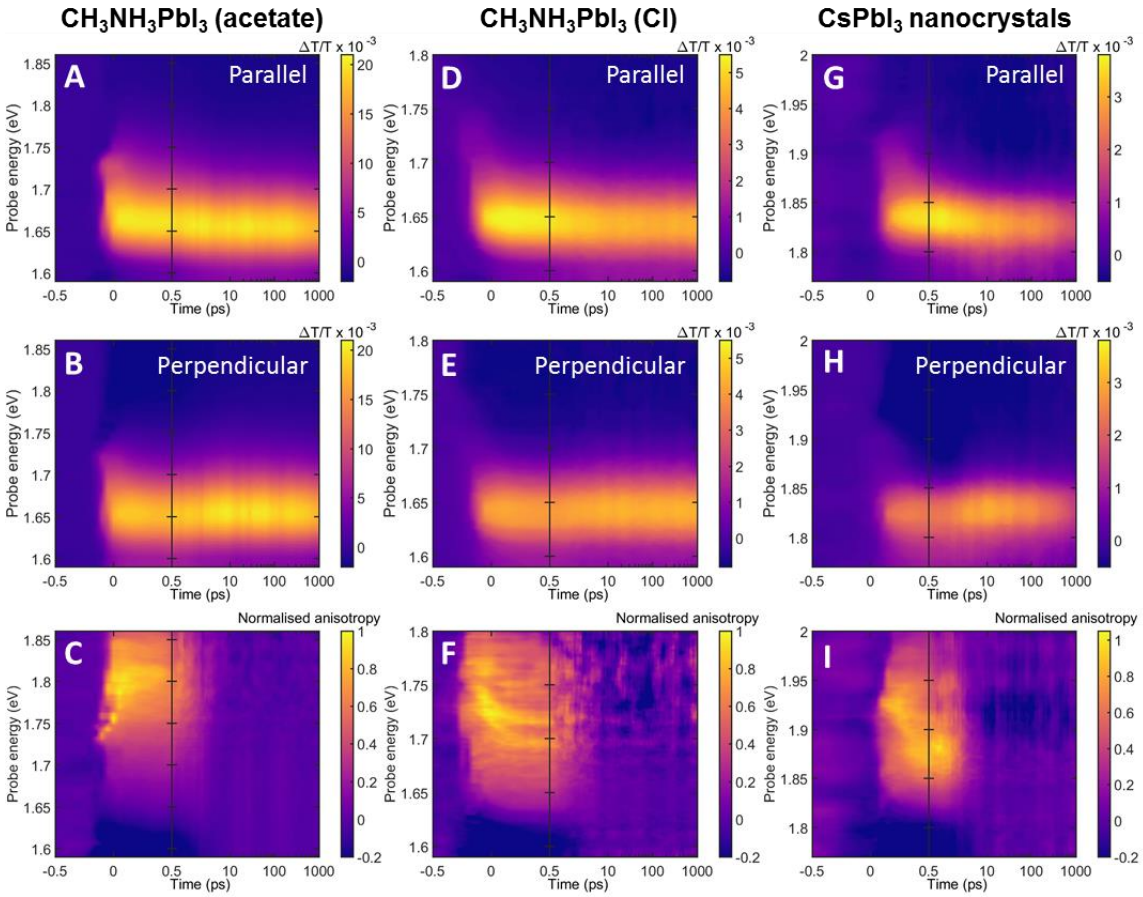

Figure 4.8 LPTA maps of standard lead halide perovskites. *LPTA maps of a (A,B) $CH_3NH_3PbI_3$ (acetate) bulk film, (D,E) $CH_3NH_3PbI_3$ (Cl) bulk film and (G,H) $CsPbI_3$ nanocrystal film and (C,F,I) the corresponding anisotropy maps. The $CH_3NH_3PbI_3$ (acetate) bulk film, the $CH_3NH_3PbI_3$ (Cl) bulk film and the $CsPbI_3$ nanocrystal film were excited with lasers of energy 1.72 eV, 1.72 eV and 1.9 eV and intensities of ~16 μJ cm^{-2}, ~2 μJ cm^{-2}, ~3 μJ cm^{-2} respectively. All lasers had a 1 kHz repetition rate, ~50 fs pulse duration and ~25 meV FWHM.*

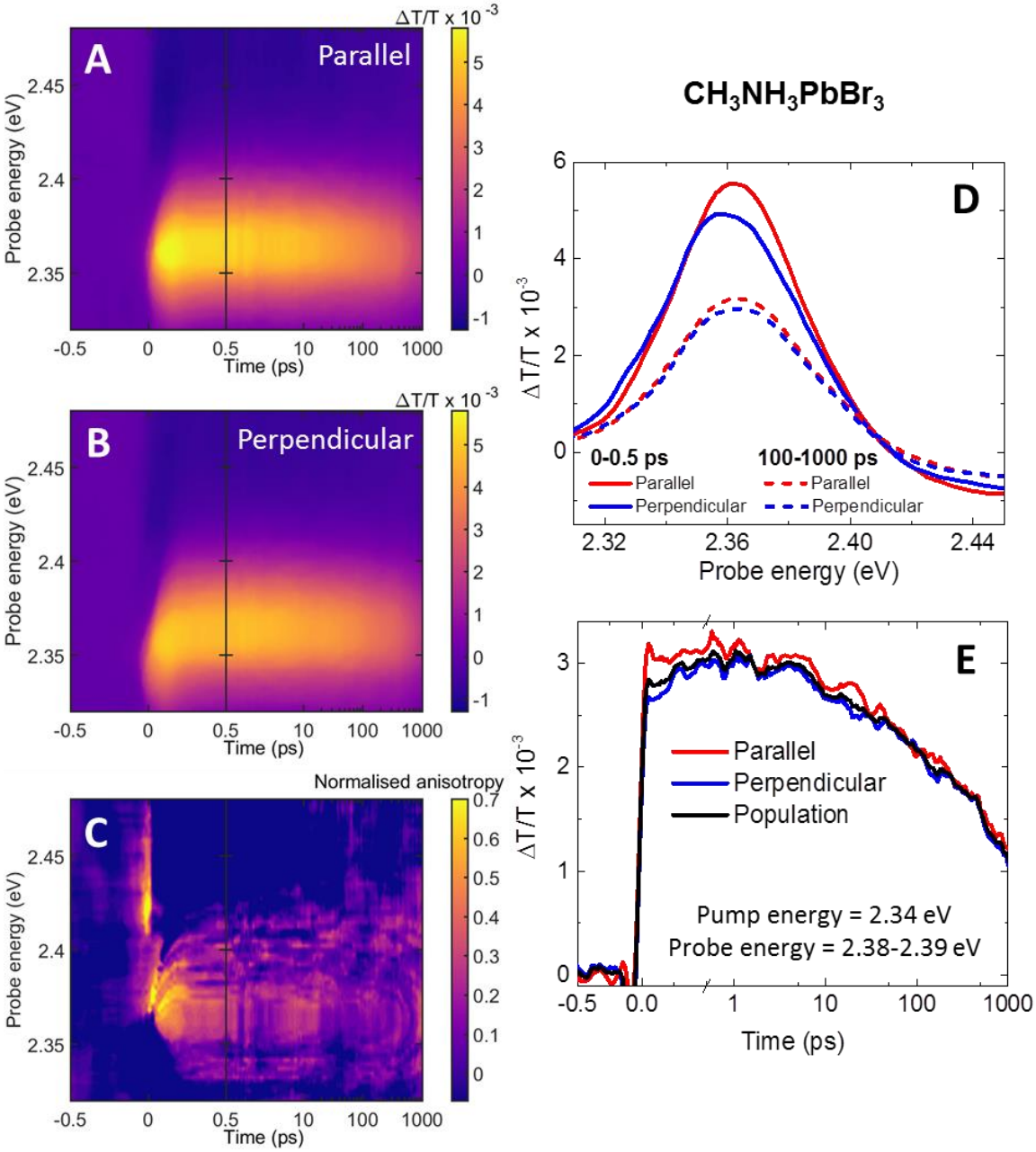

Figure 4.9 LPTA of a $CH_3NH_3PbI_3$ bulk film. *LPTA maps with the linear polarisation of the probe pulse aligned (A) parallel and (B) perpendicular to the linear polarisation of the pump pulse. (C) Anisotropy map. LPTA (D) spectra and (E) kinetics measured with the linear polarisation of the probe pulse aligned either parallel (red) or perpendicular (blue) to the linear polarisation of the pump pulse.*

4.4.4 Effect of pump energy on the polarisation anisotropy

Different pump energies create excited states at different positions in the band, allowing us to investigate whether the behaviour of the observed anisotropy is dependent on the initial state occupied by the photoexcited charge carriers. The anisotropy measured at a fixed probe energy above the GSB peak for all the standard lead halide perovskite samples is shown in Figure 4.10. The anisotropy is calculated at probe energies of 1.71 eV, 1.69 eV, 1.87 eV and 2.37 eV for the $CH_3NH_3PbI_3$ (acetate), $CH_3NH_3PbI_3$ (Cl), $CH_3NH_3PbBr_3$ bulk films and the $CsPbI_3$ nanocrystal film respectively and is averaged over the first 10 ps in the iodide samples and over the first 1 ps in the bromide sample. The pump energy was varied from 1.7-2.5 eV, whilst keeping the excitation density constant.

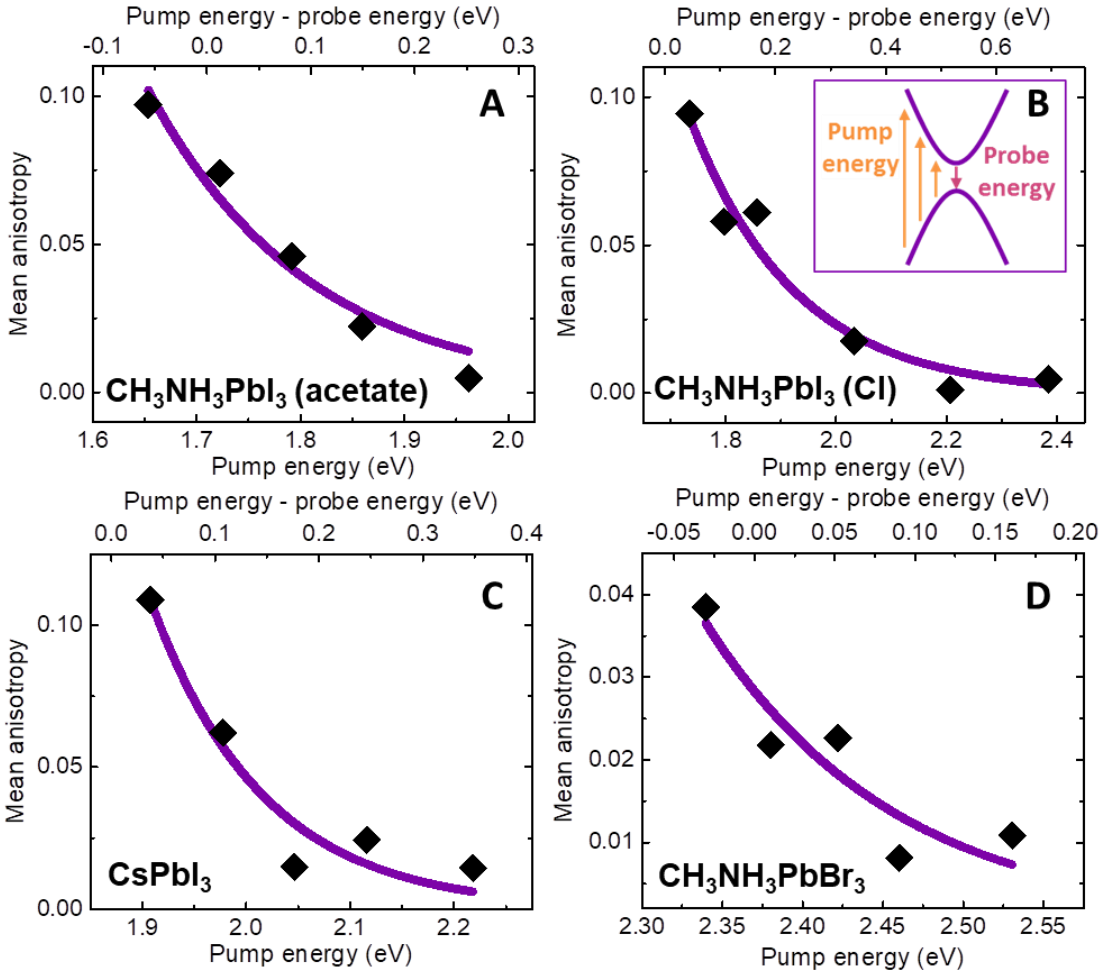

Figure 4.10 Pump energy dependent average anisotropy for all standard lead halide perovskites. *The anisotropy of the GSB was averaged over the first ~10 ps after photoexcitation for the (A) $CH_3NH_3PbI_3$ (acetate) bulk film, (B) $CH_3NH_3PbI_3$ (Cl) bulk film and (C) $CsPbI_3$ nanocrystal film and over the first ~1 ps after photoexcitation for the (D) $CH_3NH_3PbBr_3$ bulk film. The $CH_3NH_3PbI_3$ (acetate), $CH_3NH_3PbI_3$ (Cl), $CsPbI_3$ and $CH_3NH_3PbBr_3$ samples were excited with lasers of intensity ~16 $\mu J\ cm^{-2}$, ~2 $\mu J\ cm^{-2}$, ~40 $\mu J\ cm^{-2}$ and ~1 $\mu J\ cm^{-2}$ respectively. The data is fitted with simple single-exponentials with decay constants of 155 meV, 190 meV, 110 meV and 120 meV for the $CH_3NH_3PbI_3$ (acetate), $CH_3NH_3PbI_3$ (Cl), $CsPbI_3$ and $CH_3NH_3PbBr_3$ samples respectively.*

In all samples, the average anisotropy is largest when the pump energy is close to resonance with the probe energy. The anisotropy decreases as the difference between pump and probe energy increases. Simple single-exponential fits to the data indicate characteristic energies of around 150 meV, which is over an order of magnitude higher than the dominant phonon modes of the material (~50 cm^{-1} = 6 meV). The corresponding pump energy dependent anisotropy kinetics of the GSB signal for all the standard lead halide perovskites are plotted in Figure 4.11. We observe that increasing the pump energy reduces the magnitude of the anisotropy, but does not significantly change the lifetime.

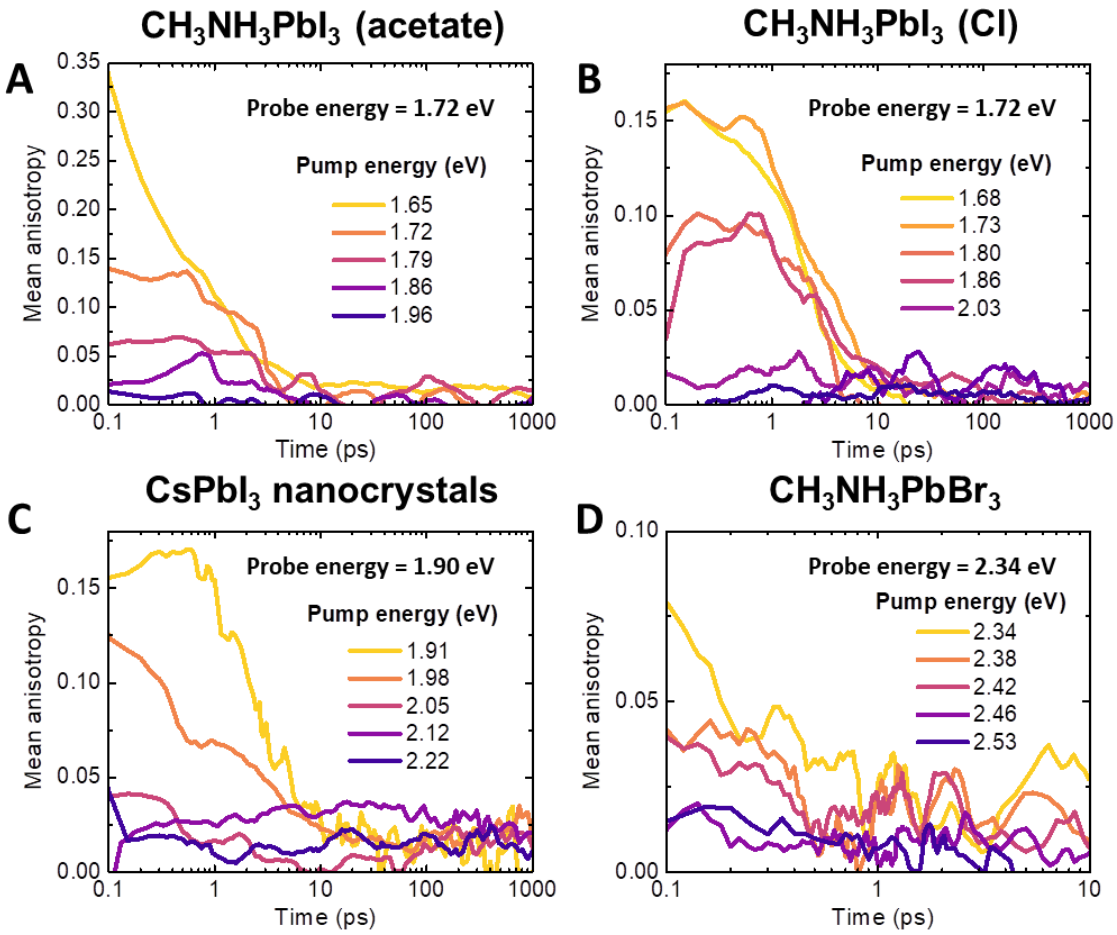

Figure 4.11 Pump energy dependent anisotropy kinetics for all standard lead halide perovskite samples. *The anisotropy kinetics decay within ~10 ps in the (A) $CH_3NH_3PbI_3$ (acetate) bulk film, (B) $CH_3NH_3PbI_3$ (Cl) bulk film and (C) $CsPbI_3$ nanocrystal film. The anisotropy kinetics decay within ~1 ps in the (D) $CH_3NH_3PbBr_3$ bulk film. The $CH_3NH_3PbI_3$ (acetate), $CH_3NH_3PbI_3$ (Cl), $CsPbI_3$ and $CH_3NH_3PbBr_3$ samples were excited with lasers of intensity ~16 $\mu J\ cm^{-2}$, ~2 $\mu J\ cm^{-2}$, ~40 $\mu J\ cm^{-2}$ and ~1 $\mu J\ cm^{-2}$ respectively.*

4.4.5 Effect of excitation density on the polarisation anisotropy

In order to investigate whether the behaviour of the observed anisotropy was dependent on excitation density, we carried out excitation density dependent LPTA measurements on the standard lead halide perovskite films. The typical response is shown in Figure 4.12, for a $CH_3NH_3PbI_3$ bulk film excited with a 1.72 eV at excitation densities of ~10^{16} cm^{-3}, ~10^{17} cm^{-3} and ~10^{18} cm^{-3}. The average anisotropy decreases with increasing excitation density, but the lifetime remains around ~10 ps.

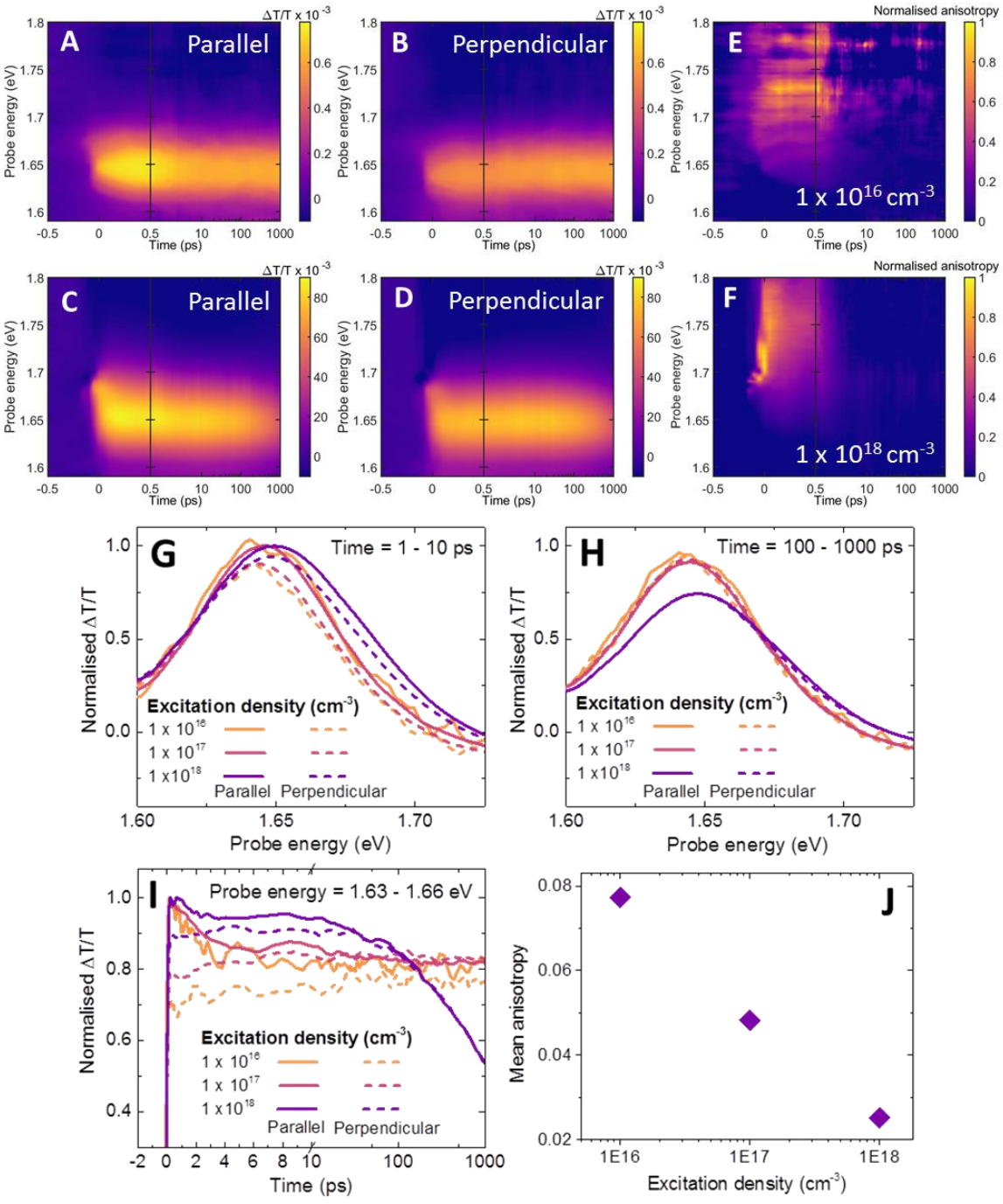

Figure 4.12 Effect of excitation density on the anisotropy. *LPTA maps of a $CH_3NH_3PbI_3$ bulk film excited with a 1.72 eV laser (1 kHz repetition rate, ~50 fs pulse duration and ~25 meV FWHM) with an excitation density of (A,B) ~10^{16} cm^{-3} and (C,D) ~10^{18} cm^{-3}. (E,F) Corresponding anisotropy maps. LPTA (G,H) spectra and (I) kinetics, indicating that the anisotropy is larger for lower excitation densities, but has an excitation independent lifetime of ~10 ps. (J) Anisotropy averaged over time delays of 0-10 ps and probe energies of 1.64-1.68 eV for excitation densities of ~10^{16} cm^{-3}, ~10^{17} cm^{-3} and ~10^{18} cm^{-3}. The average anisotropy is lower at higher excitation densities.*

4.4.6 First principles calculations of the polarisation anisotropy

In standard inorganic semiconductors, like GaAs, photoexcitation with linearly polarised light can generate a charge carrier population with an anisotropic carrier momentum distribution, because the optical transition dipole moment (TDM) can vary with the angular momentum of the electronic wave functions[192–195]. However, this anisotropy decays through carrier-carrier scattering within a few femtoseconds after photoexcitation[194]. In contrast, in standard organic semiconductors, with more localised excitonic states, optical alignment may arise from an alignment of the TDM with the physical structure. In this case either an intrinsic (steady-state)[169,170,253,254] or an induced (transient)[185–187,255,256] anisotropy may be observed. If the anisotropy is induced (transient), it may decay through physical reorientation of the photoexcited molecules or by diffusion of the excited charge carriers to neighbouring regions with different TDM orientations. The timescales of such physical reorientation and diffusion are typically orders of magnitude longer than the timescales associated with carrier scattering.

In order to determine whether the anisotropy observed in the LPTA of the standard lead halide perovskite samples is likely to arise from similar mechanisms, we used first principles calculations to model the perovskite band structure. Liang Tan, in the group of Andrew Rappe at the University of Pennsylvania, carried out these calculations by considering a $\sqrt{2} \times \sqrt{2} \times 2$ unit cell of the tetragonal phase $CH_3NH_3PbI_3$ structure. We used a structure in which the CH_3NH_3 molecules are in a polar configuration, which is known to be a local energy minimum for this unit cell[257]. This structure therefore serves as a local electronic structure model for $CH_3NH_3PbI_3$. It has a polar axis in the z-direction, which breaks the local inversion symmetry. Our calculations show that the breaking of the inversion symmetry has consequences not only for the band energies, but also for the transition dipole moments (TDM). In Figure 4.13 we plot the calculated transition dipole moments and ground state absorption close to the absorption edge. We find that the absorption is stronger when the light polarisation axis is perpendicular to the Rashba direction and weaker when it is parallel to the Rashba direction, with a crossing near the band edge.

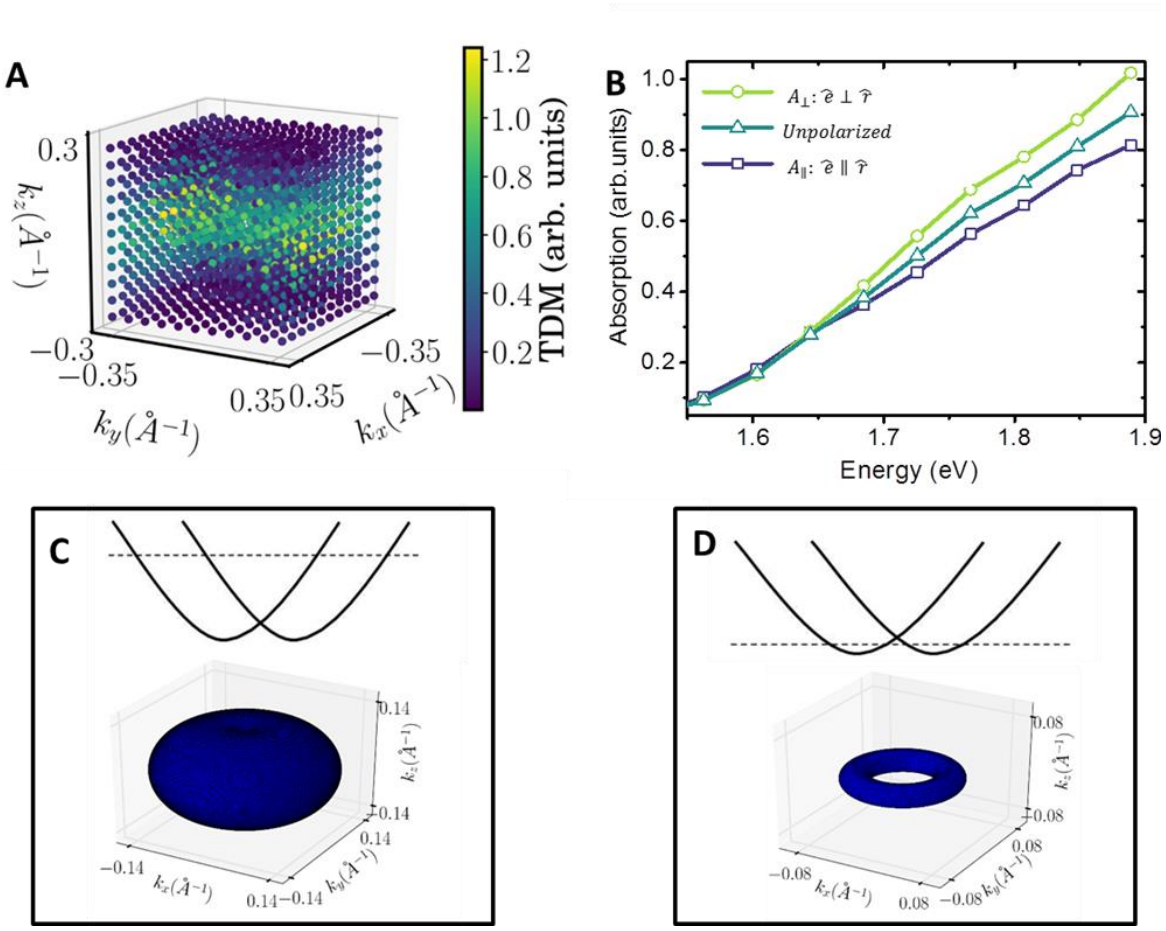

Figure 4.13 First-principles calculation of the transition dipole moments (TDMs) of $CH_3NH_3PbI_3$. *(A) Plot of the TDM k-space asymmetry for energies close to the band minima (B) Calculated absorption spectrum from first principles for electric field polarisation direction ê parallel and perpendicular to the Rashba direction of the crystal lattice r̂, and for unpolarised light. Iso-energetic surfaces of photoexcited carrier distributions for photon energies (C) above and (D) close to the band edge.*

The shape of the measured LPTA spectra can be understood by using the spectral dependence of the calculated anisotropy in a simple model[137]. While qualitative agreement with experiment can be achieved in this way, as shown in Figure 4.14A, there is a mismatch in the crossing point of parallel and perpendicular polarisations that cannot be replicated. A more quantitative fit to the data can be achieved if, in addition, the effective carrier temperature is allowed to differ for different polarisations, also shown in Figure 4.14B. This recreates the experimental data more effectively, including the crossing near the band edge, and shows that there is different broadening in the parallel and perpendicular spectra which is accurately modelled as a change in effective carrier temperature. This spectral broadening cannot be qualitatively accounted for by differences in the homogeneous and inhomogeneous broadening, reduced effective mass, or asymmetry in the effective masses of electrons and holes. This leads to the intriguing possibility that the parallel and perpendicular populations maintain different temperatures, or carrier-phonon interactions, for many picoseconds. This may well be justified, given the early-time data shown in Figure 4.4, which shows clear differences in the thermalisation rates for the carrier populations probed in the parallel and perpendicular configurations at time delays of less than 100 fs.

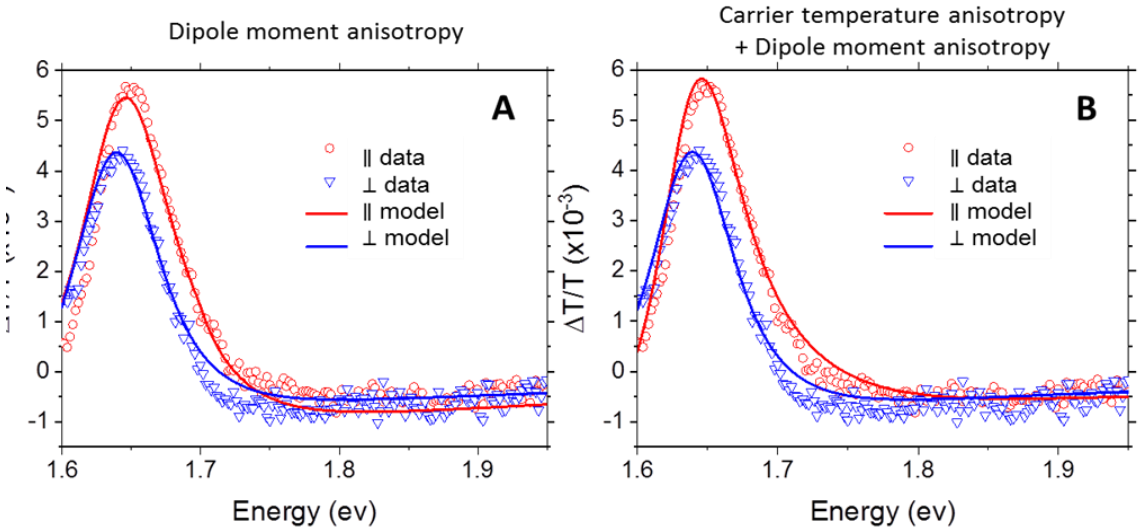

Figure 4.14 LPTA spectra and modelled spectra of $CH_3NH_3PbI_3$. *Experimental data (hollow circles and triangles) and modelled data (solid lines) are shown with the linear polarisation of the probe pulse aligned parallel (red) and perpendicular (blue) to the linear polarisation of the pump pulse. (A) LPTA data is modelled using the procedure described in Price et al.*[137]*. All parameters are identical in the parallel and perpendicular cases, except for the transition dipole moment which has an anisotropy of the form predicted in the first-principles calculations. (B) LPTA data modelled as in (A) but with an additional difference in effective carrier temperature. The parallel and perpendicular spectra have effective carrier temperatures of 410 K and 310 K respectively. When this difference in effective carrier temperatures is included, the model effectively replicates the spectral broadening and the crossing near the optical bandgap observed in the experimental data.*

The first-principles calculations predict that the anisotropy in absorption is imprinted into the carrier populations upon optical excitation. The total transient absorption signal for a sample containing many polarised nanoregions (NR) can be written in the condensed shown in Equation 4.4,

$$\langle \alpha \rangle = \sum_{i \in NR} \Pi_i \cdot n_i \qquad 4.4$$

where Π_i is the transition dipole element squared in a given nanoregion i and n_i is the density of available optical transitions in that nanoregion. Since each region has a different Rashba axis, Π_i and n_i depend on the nanoregion, and cannot be treated as constant.

The larger the TDMs along the light polarisation axis, the higher the excitation density will be, and the lower n_i will be. For the parallel and perpendicular configurations, the correlations between Π_i and n_i will be different in magnitude. This leads to different values of $\langle \alpha \rangle$ and generates an anisotropy, as quantified in Equation 4.5,

$$A = -\frac{3}{2}\frac{C_{20}}{C_{00}}\frac{B_{20}}{B_{00}} \qquad 4.5$$

where C_{lm} and B_{lm} are the coefficients of the expansions of Π_i and n_i in spherical harmonics. We estimate values of C_{lm} and B_{lm} from our DFT calculations, obtaining a value of A = 0.09 for the polarisation anisotropy of $CH_3NH_3PbI_3$, for pump and probe energies of 1.7 eV. Comparing this theoretical estimate to the magnitudes of the measured anisotropy indicates that this mechanism is largely responsible for the observed polarisation anisotropy. As this theoretical estimate is based on a single structure at a local energy minimum, it is likely that it will be increased if other non-equilibrium structures with higher polarity are considered as well.

As the structure fluctuates on picosecond time scales, the Rashba axis changes stochastically in each nanoregion. We assume that this stochastic evolution approximates a random walk, with nanoregions losing memory of their initial Rashba directions after a characteristic time τ. Over this time scale, the values of Π_i become randomized and uncorrelated with n_i. The LPTA signals for both parallel and perpendicular configurations would then regress towards the uncorrelated value $\langle \alpha \rangle = \langle \Pi \rangle \cdot \langle \mathrm{n} \rangle$ in the long time limit. This would cause the anisotropy to decay to zero, as observed in the LPTA measurements.

Our theoretical model above assumes an isotropic distribution of carrier momenta shortly after photoexcitation, in agreement with literature which suggests that thermalisation and cooling processes randomise carrier momentum within 200 fs after photoexcitation[135]. This is true for excitations with more than ~100 meV excess energy above the band edge, for which the excitation isosurface is approximately spherical, as shown in Figure 4.13. However, excitations close to the band edge access a restricted momentum space, since the presence of polar distortions leads to toroidal isosurfaces, also shown in Figure 4.13. To demonstrate how the changes in the momentum space distribution with energy affect the LPTA signals, we write the LPTA signal for a single nanoregion as an integral over momentum space, as shown in Equation 4.6.

$$\alpha_i = \int_S dk\ \Pi_i(k) n_i(k) \qquad 4.6$$

Here, the momentum resolved TDMs $\Pi_i(k)$ and the energy isosurface S depend only on the probe energy and the Rashba direction. On the other hand, the momentum resolved carrier densities $n_i(k)$ depend on the pump energy and the Rashba direction. As the pump energy is increased above the optical bandgap, the carrier density isosurface at excitation becomes progressively more spherical, and hence less correlated with the Rashba direction. This leads to a decreasing correlation between α_i and the Rashba direction with increasing separation between the pump and probe energies. The dependence of the anisotropy on pump energy, shown in Figure 4.10, is consistent with this interpretation. However, we cannot rule out an additional influence from more energetic carriers losing excess energy to the lattice as they relax to the band edges, which could result in more rapid structural deformations of the lead-halide lattice and a partial randomisation of the initial Rashba directions.

4.5 Conclusions and future work

In this chapter, we have investigated the role of lattice distortion and the coupling between charge carriers and lattice phonons in $CH_3NH_3PbI_3$ (acetate), $CH_3NH_3PbI_3$ (Cl) and $CH_3NH_3PbBr_3$ bulk films and in $CsPbI_3$ nanocrystal films, all with spatially and temporally averaged central symmetry. Using LPTA we have shown that standard lead halide perovskites exhibit a long-lived photo-induced anisotropy, with a lifetime of

around ~10 ps in iodide perovskites and a lifetime of around ~1 ps in bromide perovskites, independent of whether the A-site cation is CH_3NH_3 or Cs. These observations contrast similar measurements in GaAs, in which the anisotropy decays through carrier-carrier and carrier-phonon scattering within a few 100 fs after photoexcitation.

First-principles calculations suggest that the observed anisotropy arises from dynamic disorder in the lead halide lattice. Dynamic deformations of small regions of the lattice, for example through anharmonic lattice vibrations, lead to localised polarised lattice distortions. Experiments and calculations suggest that such nanoregions form spontaneously within lead iodide lattices on picosecond timescales and have characteristic sizes of <10 nm[42,44]. This indicates that the samples and individual crystallites consist of multiple nanoregions, each with different optical and electronic properties, which dynamically fluctuate on picosecond timescales[48,53,240,241].

These picosecond local polar lattice distortions affect the optical and electronic properties of charge carriers in lead halide perovskites under device operating conditions (ambient temperature and pressure), giving rise to a dynamic landscape of electronic states. In the future, it may be possible to enhance and stabilise this effect by applying a suitable external strain to the lattice, such as a piezoelectric force[49,37]. The electron-phonon interactions mediated by this mechanism also suggest that such external strain could also be used to control thermal conductivity, with implications for lead halide perovskite thermoelectrics. This behaviour is not typically observed in classical organic or inorganic semiconductors, so our observations have far-reaching implications for the understanding and application of this important new class of materials.

Although the first principles calculations offer one explanation for the observed long-lived photo-induced anisotropy, reduced carrier-carrier and carrier-phonon scattering could offer another explanation. In this case, the parallel and perpendicular LPTA spectra shown in Figure 4.5 could be interpreted as a hotter, higher density carrier population and a colder, lower density carrier population respectively. This means that each population must have thermalised individually, in order for both the parallel and perpendicular spectra to represent fully thermalised Fermi-Dirac distributions with different temperatures. The observation that the population probed in the parallel configuration is hotter (blue shifted LPTA signal) and represents a higher density of

carriers (higher LPTA signal), indicates that these carriers have undergone less scattering with phonons or are in higher energy states. While the observation that the population probed in the perpendicular configuration is colder (red shifted LPTA signal) and represents a lower density of carriers (lower LPTA signal), indicates that these carriers have undergone more scattering with phonons or are in lower energy states. Over picosecond timescales, these carrier populations interact with each other and the parallel and perpendicular spectra converge to an intermediate temperature. This explanation is consistent with other literature that suggests that carrier-carrier and carrier-phonon scattering (especially with high energy LO phonons[239]) is hindered in lead halide perovskites[137,141,163], perhaps due to the formation of large polarons[239,258].

5 Recombination in mixed cation lead halide perovskites

In this chapter, we use TA, TPL, PLQE, XRD and Raman spectroscopy to identify the photophysical origin of the exceptional power conversion efficiencies reported in mixed cation lead halide perovskites. We find that these exceptional power conversion efficiencies coincide with a significant enhancement in the carrier lifetimes and PLQEs of these materials. Using TA and TPL we show that the first-order recombination rate decreases when inorganic and organic cations are incorporated into the crystal lattice. We also show that radiative recombination remains a second-order process at early times, even in regimes where carrier recombination is dominated by non-radiative first-order or third-order processes. By extracting the crystal lattice parameters using XRD, we find that the incorporation of mixed cations into the crystal lattice distorts the crystal lattice. These distortions coincide with changes to the vibrational modes of the crystal lattice observed in resonant-Raman measurements, which indicate that the crystal lattice becomes more homogeneous when inorganic and organic cations are incorporated into the crystal lattice. We have shown that this is an effective method of reducing the density of trap states in the material and enhancing device performance. The PLQE measurements in this chapter were carried out by Johannes Richter and Edward Booker, the Raman measurements were carried out by Tudor Thomas, and the XRD measurements were carried out by Tudor Thomas, Edward Booker and Tim van de

Goor. All samples were prepared by Michael Saliba and Silver Cruz, in the group of Michael Grätzel, at the École Polytechnique Fédérale de Lausanne.

5.1 Background and Motivation

At the end of 2016, an article was published in Science[59], indicating that the performance of lead halide perovskite solar cells is significantly improved when rubidium cations are incorporated into the crystal lattice. Michael Saliba et al., in the group of Michael Grätzel, at the École Polytechnique Fédérale de Lausanne[59] achieved stabilised power conversion efficiencies (PCEs) of up to 21.6% on small area photovoltaic devices (with an average PCE of 20.2%) and PCEs of up to 19.0% on 0.5 cm^2 photovoltaic devices. In addition to high PCEs, these devices also exhibited relatively high EQEs (3.8%) and high open circuit voltages (1.24 V). These open circuit voltages, measured in lead halide perovskites with a bandgap of 1.63 eV, correspond to a voltage drop of only 0.39 V. This is even lower than the voltage drop of 0.4 V in commercial silicon solar cells.

In addition to improving device performance, the addition of rubidium cations enhanced the stability of the material. An improved Goldschmidt tolerance factor and an increase in the entropy of mixing have been suggested as the reason for this increase in stability[59]. Coated with a polymer layer, the devices maintained 95% of their initial performance at 85°C for 500 hours under full solar illumination and maximum power point tracking[59].

Such improvements in device performance and stability have also been reported in other mixed cation lead halide perovskites. Previous record-breaking solar cell performances were achieved by mixing methylammonium and formamidinium cations as well as Br and I halides[63–65]. Several other investigations have also focused on improving the stability and efficiency of perovskite devices by using various mixtures of Cs, methylammonium and formamidinium cations[57,58,60–62].

The results of these high-impact studies demonstrate the exciting commercialisation potential of these materials. However, many questions remain about the fundamental origin of their excellent photovoltaic performance. For example, does the addition of rubidium change the properties of the crystal structure, lead to localised regions, change the free carrier nature of the dominant charge carriers, change the nature of the radiative

and non-radiative recombination pathways, or reduce the density of trapping sites in the material? Answering these questions, by combining results from photoluminescence quantum efficiency (PLQE), transient photoluminescence (TPL), transient absorption (TA), x-ray diffraction (XRD) and Raman spectroscopies, could lead to new ideas for further improvements in device performance and will therefore be the focus of this chapter.

5.2 Preparation of mixed cation perovskites

All mixed cation perovskites were prepared by the group of Michael Grätzel, at the École Polytechnique Fédérale de Lausanne, using the methods described in detail in Section 3.1.2. Throughout this chapter we use the nomenclature MAPbI, MAPbIBr, MAFAPbIBr, CsMAFAPbIBr and RbCsMAFAPbIBr to refer to the complete perovskite compounds containing the various combinations of methylammonium CH_3NH_3 (MA), formamidinium $(NH_2)_2CH^+$ (FA), Cs, Rb, Pb, I and Br. All of the FA containing samples are prepared with FA as the majority cation, because the red-shifted band gap is beneficial for solar cell performance. The percentage of Rb and Cs included in the total A-site composition can be varied, but we focus on the samples containing 5% Rb and 5% Cs, as the best performing solar cells were fabricated from these materials.

Increasing the percentages of Rb and Cs beyond 5% leads to a decrease in photovoltaic performance and stability, because the ionic radii of Rb and Cs are too small to form stable photoactive perovskite crystal structures. At room temperature, pure $RbPbI_3$ and $CsPbI_3$ exist in a non-photoactive yellow phase because their tolerance factor does not lie comfortably between the required values of 0.8 and 1, as shown in Figure 5.1. Therefore, while adding a few percent of Rb and Cs can improve the quality of the crystal lattice, adding too much can lead to phase segregation and the formation of regions of $RbPbI_3$ and $CsPbI_3$ as shown in Figure 5.2. Images of the films obtained from scanning electron microscopy (SEM) also indicate that the addition of 5% Rb to the perovskite lattice leads to the formation of larger perovskite crystals, which have previously been shown to enhance the performance of solar cell devices[259].

Image removed for copyright reasons.

Figure 5.1 Tolerance factors of $APbI_3$ perovskites (where A is either Li, Na, K, Rb, Cs, methylammonium or formamidinium) and corresponding images of the films formed, both taken from reference 59. *(A) A stable perovskite crystal structure is generally only formed when the tolerance factor lies comfortably between 0.8 and 1. (B) $CsPbI_3$ has a tolerance factor very close to 0.8 and therefore exists in a non-photoactive yellow phase at room temperature. A phase transition to the photoactive black phase occurs when the material is heated to 380°C. $RbPbI_3$ also exists in a yellow non-photoactive phase at room temperature and remains in a non-photoactive yellow phase at 380°C.*

Image removed for copyright reasons.

Figure 5.2 X-ray diffraction (XRD) spectra of $RbPbI_3$, and RbCsMAFAPbIBr perovskite with varying Rb percentage x, taken from reference 59. *(A) Addition of Rb modifies the crystal lattice and reduces the intensity of the peaks assigned to Pb excess and yellow-phase impurities. (B) As the percentage x of Rb is increased, peaks appear at 13.4° and 10.1°. Similar peaks are observed in pure $RbPbI_3$, indicating that phase segregation occurs at higher Rb concentrations.*

Image removed for copyright reasons.

Figure 5.3 Scanning electron microscopy (SEM) images of RbCsMAFAPbIBr perovskites, taken from reference 59. *Films contain (A) 0% Rb, (B) 2% Rb, (C) 5% Rb and (D) 10% Rb.*

5.3 Steady-state absorption of mixed cation perovskites

In order to confirm that the prepared samples were representative of those investigated in previous literature, the steady-state absorption spectrum of each mixed cation sample was measured using the method described in detail in section 3.2.4 and the optical bandgaps were extracted using standard Tauc plots[260], as shown in Figure 5.4.

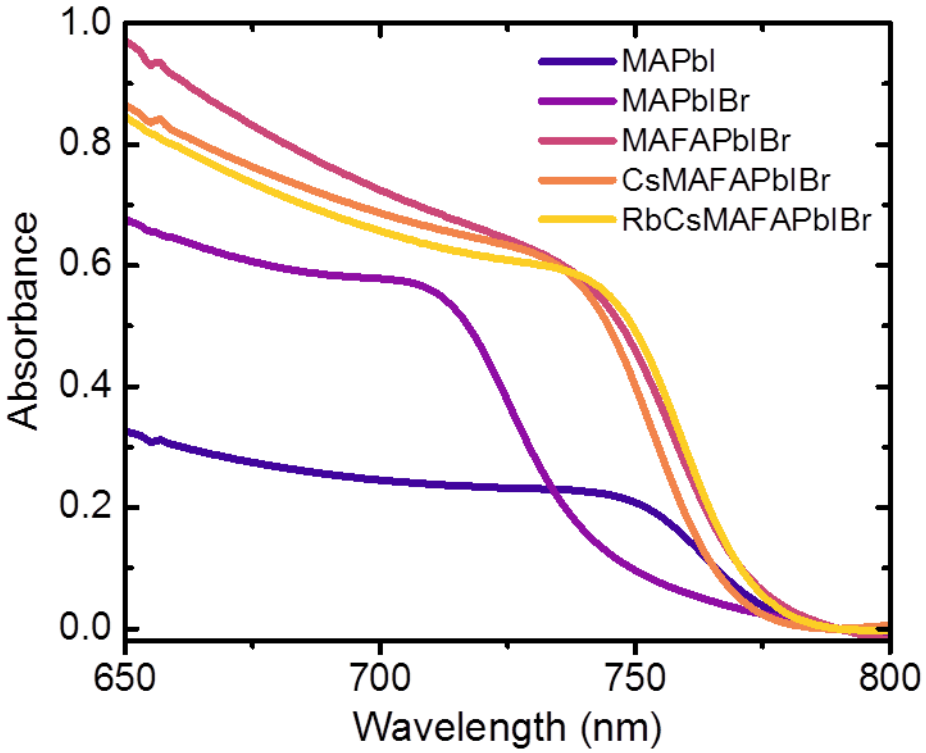

Figure 5.4 Steady-state absorption spectra of mixed cation perovskite samples. *All samples were prepared on glass. The absorbance of all samples is similar, except for the MAPbI sample. The reduced absorbance in the MAPbI sample arises from the experimental challenges associated with preparing thick MAPbI films, resulting in a ~130 nm thick MAPbI sample compared to the ~400 nm thick MAPbIBr, MAFAPbIBr, CsMAFAPbIBr and RbCsMAFAPbIBr samples*[59].

The pure MAPbI was found to have an optical bandgap onset of 779 nm (1.59 eV), which blue shifts upon the addition of Br to 748 nm (1.66 eV) in the MAPbIBr sample. The addition of FA leads to a red shift, resulting in an optical band gap of 776 nm (1.60 eV) for the MAFAPbIBr sample. But the addition of Cs (5%) and Rb (5%) makes little difference, resulting in optical bandgaps of 770 nm (1.61 eV) and 775 nm (1.60 eV) for

the CsMAFAPbIBr and RbCsMAFAPbIBr samples respectively. Therefore, the enhanced device performance of the RbCsMAFAPbIBr sample cannot simply be explained by a change in the optical bandgap. Such values are comparable to those found in the literature[59,62], indicating that the prepared films had comparable optical properties to those found in the literature.

5.4 Photoluminescence quantum efficiency (PLQE) of mixed cation perovskites

In general, the PLQE of a material is a good indicator of potential device performance, where materials with higher PLQEs generally outperform materials with lower PLQEs[165]. This is because low PLQEs indicate that recombination may mostly be occurring through undesirable non-radiative recombination pathways including trap states. These non-radiative recombination pathways reduce the build-up of charge carrier density in solar cells, reducing the open-circuit voltage and therefore the device efficiency. This is why device efficiencies are generally higher when they are fabricated from materials with higher PLQEs.

The PLQEs of the mixed cation perovskites were measured by Johannes Richter and Edward Booker using the method described in detail in Section 3.2.5. The PLQEs vary by almost an order of magnitude from between 2.7% for the MAPbIBr film to 26.4% for the RbCsMAFAPbIBr film, as shown in Table 5.1.

Sample	PLQE (%)
MAPbI	16.8
MAPbIBr	2.7
MAFAPbIBr	22.6
CsMAFAPbIBr	11.7
RbCsMAFAPbIBr	26.4

Table 5.1 Table of the PLQEs of the mixed cation perovskite samples. *All samples were prepared on standard glass, to eliminate changes in the PLQEs due to changes in outcoupling efficiency. This can arise when perovskite samples are prepared on substrates with different surface roughness*[152]*. All samples were excited with a 532 nm laser with a 650 um diameter spot size and 100 mW average power. In order to reduce any effects of sample degradation, the data was collected immediately after unblocking the laser beam. Measurements were carried out by Johannes Richter and Edward Booker.*

5.5 Transient photoluminescence (TPL) of mixed cation perovskites

In order to understand why the PLQE of the RbCsMAFAPbIBr sample was significantly higher than the PLQEs of the other samples, we carried out TPL measurements on the all samples using the method described in detail in Section 3.3.2. The low excitation density (~10^{16} cm^{-3}) TPL spectra, temporally integrated over the first µs after photoexcitation, are plotted in Figure 5.5. In agreement with the steady-state absorption spectra, the addition of Br to the lattice blue shifts the TPL spectrum, the addition of FA to the lattice red shifts the TPL spectrum, and the addition of Cs and Rb to the lattice slightly blue shifts and red shifts the TPL spectrum respectively.

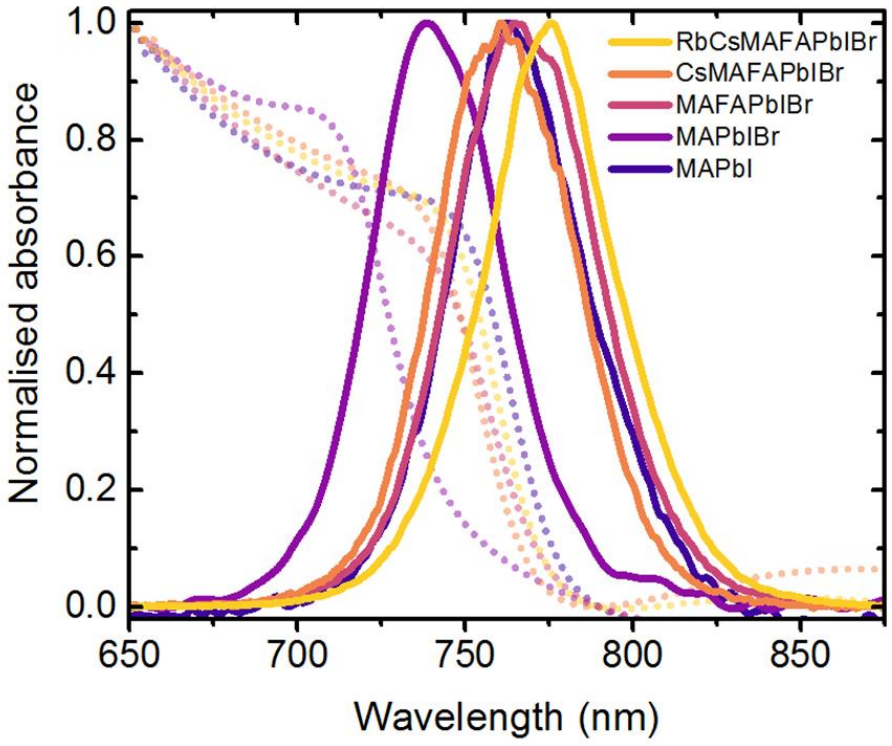

Figure 5.5 Transient photoluminescence (TPL) spectra of mixed cation perovskite samples. *The TPL spectra, temporally integrated over the first µs after photoexcitation (solid lines), are centred at 764 nm, 740 nm, 770 nm, 761 nm and 776 nm for the MAPbI, MAPbIBr, MAFAPbIBr, CsMAFAPbIBr and RbCsMAFAPbIBr samples respectively. All samples were photoexcited with a 400 nm laser (1 kHz repetition rate, ~90 fs pulse duration, ~25 meV FWHM) with a photoexcitation density of ~10^{16} cm^{-3}. Only a small Stokes shift is observed between the TPL and the steady-state absorption (dotted line) of all samples.*

The corresponding low excitation density (~10^{16} cm^{-3}) TPL kinetics, spectrally integrated over the TPL spectra, are plotted in Figure 5.6. It is clear that the photoluminescent lifetimes (1/e) change dramatically with sample composition, ranging from 32 ns for the MAPbIBr sample to 335 ns for the RbCsMAFAPbIBr sample. The excitation density dependent TPL kinetics for each sample are also plotted in Figure 5.6. In each sample, the TPL lifetime is highly excitation density dependent until the excitation density drops to below ~10^{16} cm^{-3}. Below this point, the lifetimes do not change significantly as the excitation density is reduced further, indicating that the dominant recombination mechanism transitions from a higher-order process to a first-order process.

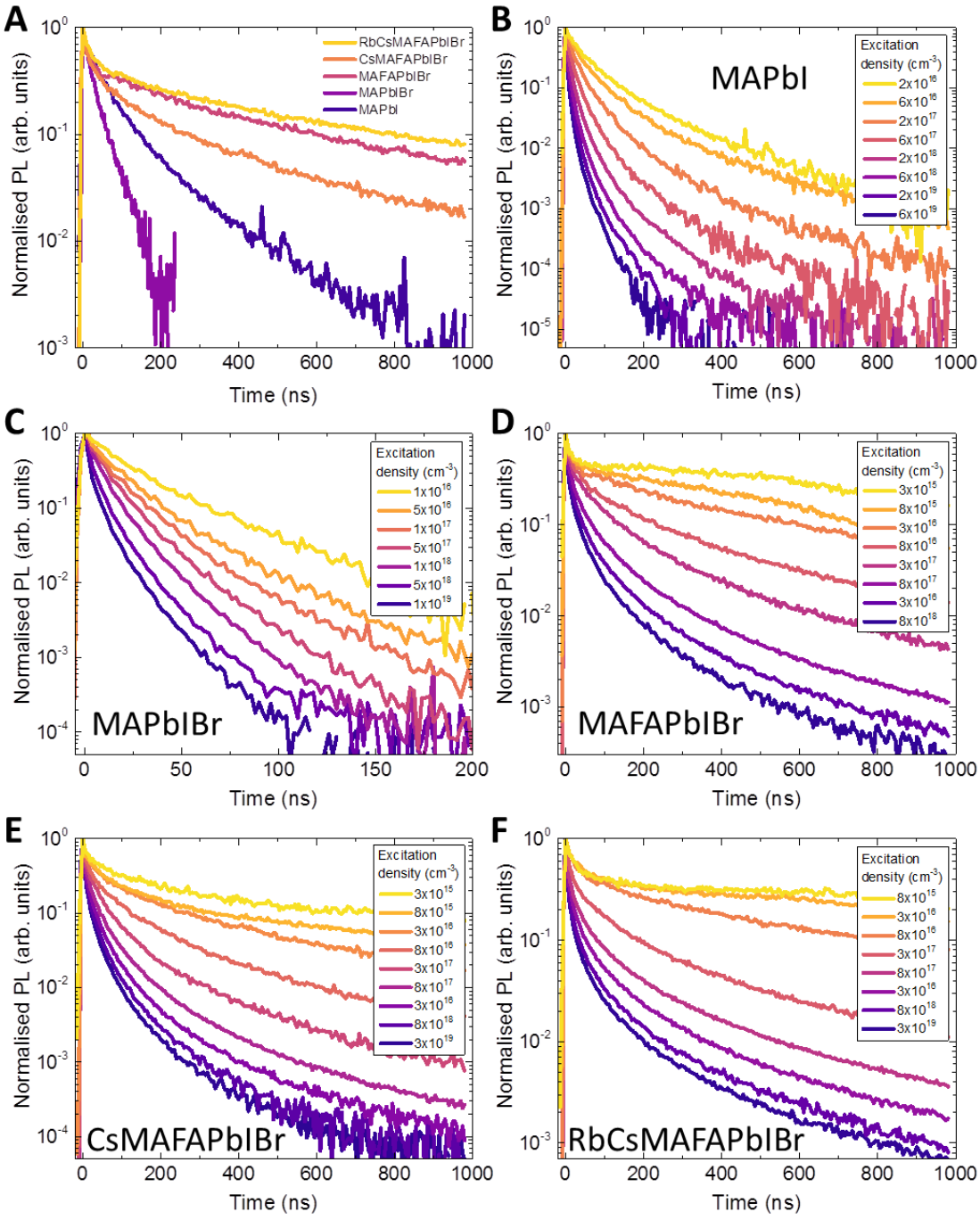

Figure 5.6 Transient photoluminescence (TPL) kinetics of mixed cation perovskite samples. *(A) The TPL kinetics, spectrally integrated over the TPL spectra, are measured with a 400 nm laser (1 kHz repetition rate, ~90 fs pulse duration, ~25 meV FWHM) with a photoexcitation density of ~10^{16} cm^{-3}. Excitation density dependent TPL kinetics, spectrally integrated over the TPL spectra, for (B) MAPbI, (C) MAPbIBr, (D) MAFAPbIBr, (E) CsMAFAPbIBr and (F) RbCsMAFAPbIBr mixed cation perovskite samples are measured with a 400 nm laser (1 kHz repetition rate, ~90 fs pulse duration, ~25 meV FWHM).*

As described in Section 2.2.2.3.4, recombination in inorganic semiconductors can generally be described by a sum of first, second and third-order processes, with different processes dominating recombination at different excitation densities. A detailed review of the recombination processes occurring in lead halide perovskites may be found in the literature[125,147,151,261,262]. Which process dominates recombination, $-\frac{dn(t)}{dt}$, at a given carrier density $n(t)$, is dependent on the first, second and third-order recombination constants k_1, k_2 and k_3 respectively, as shown in Equation 5.1.

$$-\frac{dn(t)}{dt} = k_1 \cdot n(t) + k_2 \cdot n(t)^2 + k_3 \cdot n(t)^3. \quad 5.1$$

This equation describes how both radiative and non-radiative recombination processes reduce the carrier density in the material. At any given time t, the observed TPL signal $\mathrm{TPL}(t)$ scales with the radiative recombination rate $\left(-\frac{\mathrm{d}n(t)}{\mathrm{d}t}\right)_{rad}$ at that time,

$$\mathrm{TPL}(t) \sim \left(-\frac{\mathrm{d}n(t)}{\mathrm{d}t}\right)_{rad}. \quad 5.2$$

Therefore, the TPL kinetics decrease as $n(t)$ decreases, independent of whether $n(t)$ decreases through a radiative or non-radiative process, and the first-order recombination constants can be estimated from low excitation density TPL kinetics, as shown in Figure 5.7. The MAPbIBr sample was found to have the fastest first-order decay rate (3.1×10^7 s^{-1}) and the RbCsMAFAPbIBr sample the slowest (3.0×10^6 s^{-1}).

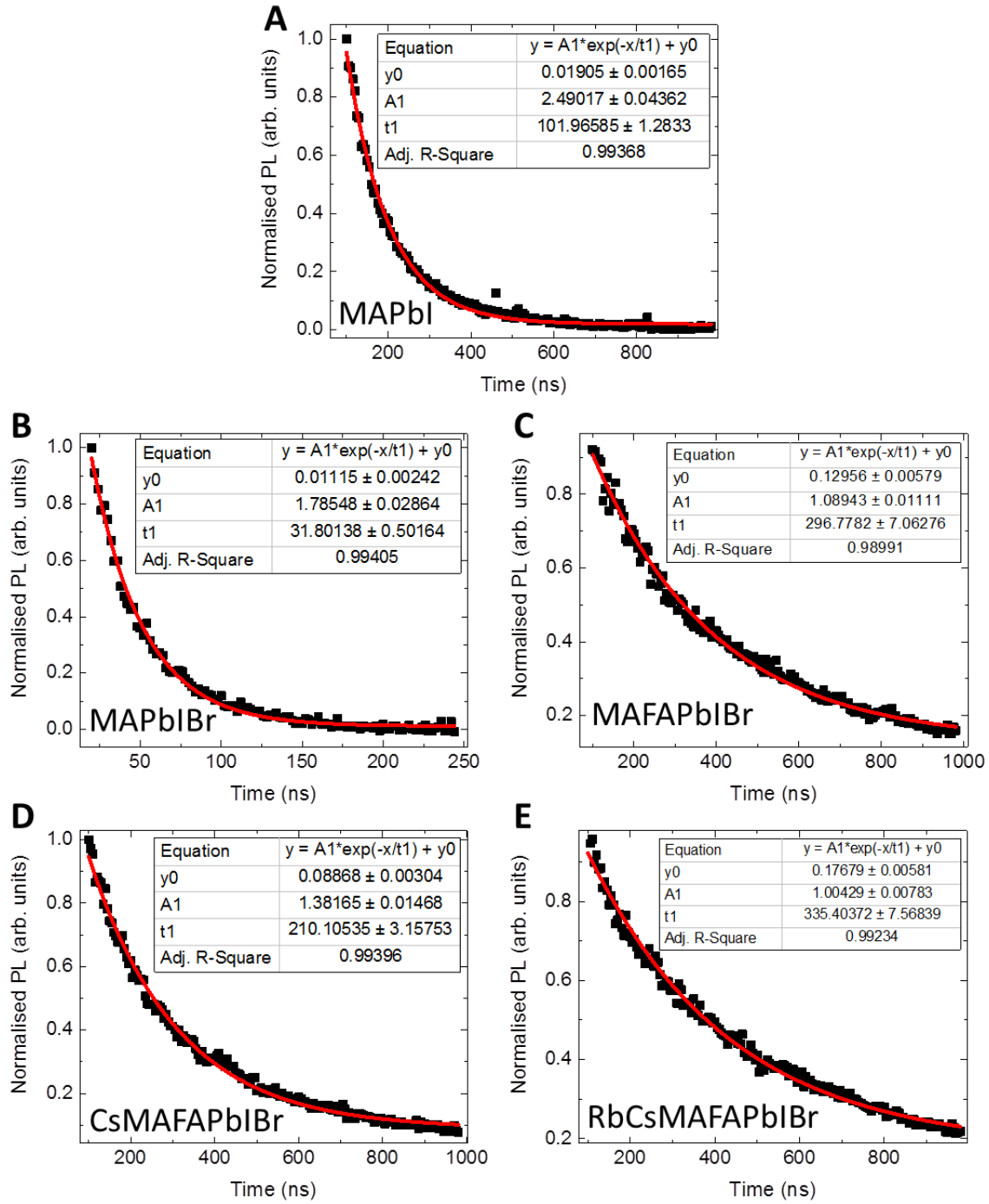

Figure 5.7 Estimated lifetimes of mixed cation perovskite samples from TPL measurements. *The TPL kinetics (black squares), spectrally integrated over the TPL spectra, were fitted after either 25 ns or 100 ns with simple monoexponential decays (solid red line) for the (A) MAPbI, (B) MAPbIBr, (C) MAFAPbIBr, (D) CsMAFAPbIBr and (E) RbCsMAFAPbIBr mixed cation perovskite samples. All samples were excited with a 400 nm laser (1 kHz repetition rate, ~90 fs pulse duration, ~25 meV FWHM) with a photoexcitation density of ~10^{16} cm^{-3}.*

In order to determine whether radiative recombination is a first, second or third-order process, the TPL signal is plotted against the carrier density $n(t)$. This is achieved by measuring the TPL signal immediately after photoexcitation PL_0, when the carrier density can be calculated from the experimental parameters such as the laser wavelength, power and spot size, as described in Section 2.2.2.3.4. Plots of PL_0 against carrier density, shown in Figure 5.8, indicate that radiative recombination is always a second-order process in mixed cation perovskites, even when the dominant carrier recombination mechanism is first-order. This suggests that radiative recombination occurs through the band-to-band recombination of free carriers, consistent with previous literature on other lead halide perovskite materials[152,263–265].

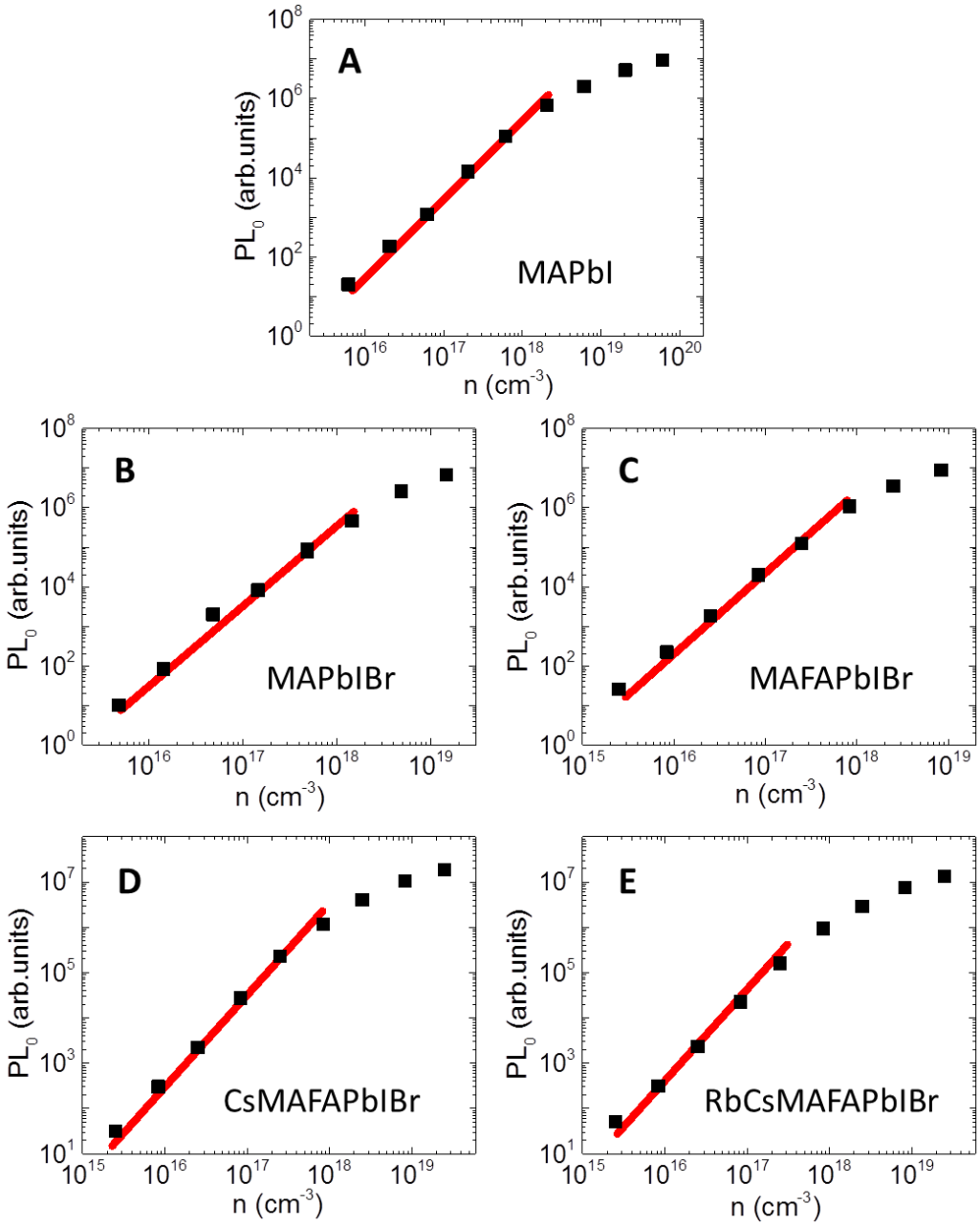

Figure 5.8 Initial TPL signal (PL_0) plotted against excitation density n for the mixed cation perovskite samples. *PL_0 (black squares) scales quadratically with carrier density even at low excitation densities where recombination is dominated by a first-order process in (A) MAPbI, (B) MAPbIBr, (C) MAFAPbIBr, (D) CsMAFAPbIBr and (E) RbCsMAFAPbIBr mixed cation perovskite samples. Red lines are guides to the eye indicating a quadratic dependence. At high excitation densities, the measured value of PL_0 does not continue to increase quadratically with excitation density because the measurement is limited by the time resolution of the ICCD setup. All samples were photoexcited with a 400 nm laser (1 kHz repetition rate, ~90 fs pulse duration, ~25 meV FWHM).*

5.6 Transient absorption (TA) of mixed cation perovskites

Next we carried out TA measurements on the mixed cation perovskite samples in order to extract the first, second and third-order recombination constants and to confirm which recombination processes dominate at which carrier densities. All measurements were done according to the method described in detail in Section 3.3.3. Typical spectra and kinetics for each mixed cation perovskite sample are shown in Figure 5.9.

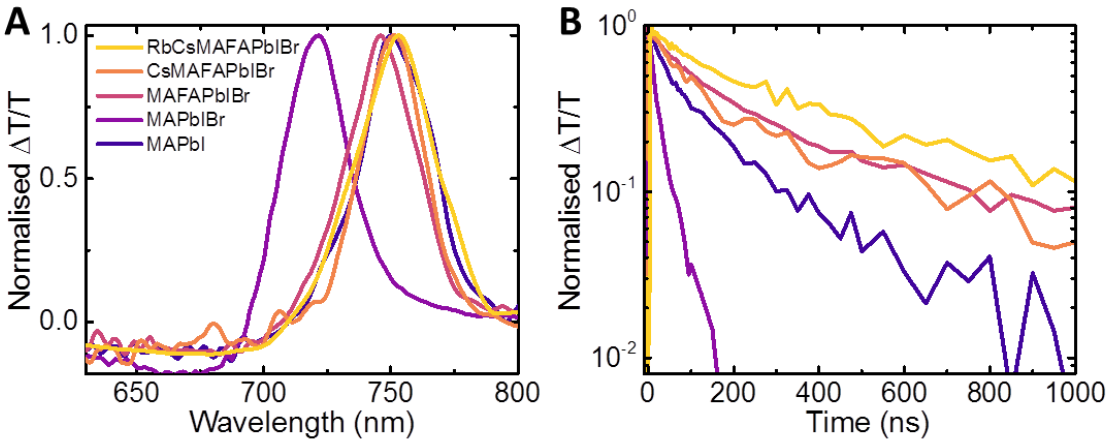

Figure 5.9 Transient absorption (TA) spectra and kinetics of mixed cation perovskite samples. *(A) The ground state bleaches (GSB) of the TA spectra, temporally integrated over the first µs after photoexcitation, are centred around 751 nm, 721 nm, 746 nm, 752 nm and 753 nm for the MAPbI, MAPbIBr, MAFAPbIBr, CsMAFAPbIBr and RbCsMAFAPbIBr samples respectively. (B) The TA kinetics, spectrally integrated over the GSB, exhibit lifetimes (1/e) of around 87 ns, 18 ns, 179 ns, 140 ns and 315 ns for the MAPbI, MAPbIBr, MAFAPbIBr, CsMAFAPbIBr and RbCsMAFAPbIBr samples respectively. All samples were excited with a 532 nm laser (500 Hz repetition rate, ~2 ns pulse duration, ~25 meV FWHM) with excitation density ~10^{17} cm^{-3}.*

The dominant feature in every TA spectrum is the positive ground state bleach (GSB) signal, arising from phase-space filling by photoexcited carriers[137,162,138], which is observed at around 720 nm in the MAPbIBr sample and at around 750 nm in all the other samples. A negative signal at wavelengths below 700 nm is also observed in all samples, arising from previously reported refractive index changes[137]. The lifetime of the GSB signal varies significantly for different sample compositions, with the MAPbIBr sample having a lifetime of around only 18 ns and the RbCsMAFAPbIBr

sample having a lifetime of around 315 ns, at an excitation density of ~10^{17} cm^{-3}. This spectral shift and increase in lifetime is consistent with the TPL measurements.

The first, second and third-order recombination constants were extracted from the TA data by plotting the recombination rate $-\frac{dn(t)}{dt}$ against carrier density $n(t)$ for each mixed cation perovskite sample, as shown in Figure 5.10. As reported in the literature[152], a good estimate of the carrier density as a function of time can be achieved by integrating over the GSB as a function of time and then scaling this to the initial excitation density calculated from the experimental parameters such as the laser wavelength, power and spot size, as described in Section 2.2.2.3.4. Once the carrier density as a function of time is known, the recombination rate is calculated simply by taking the derivative of the carrier density with respect to time. This recombination rate is then plotted against carrier density to generate the plots in Figure 5.10.

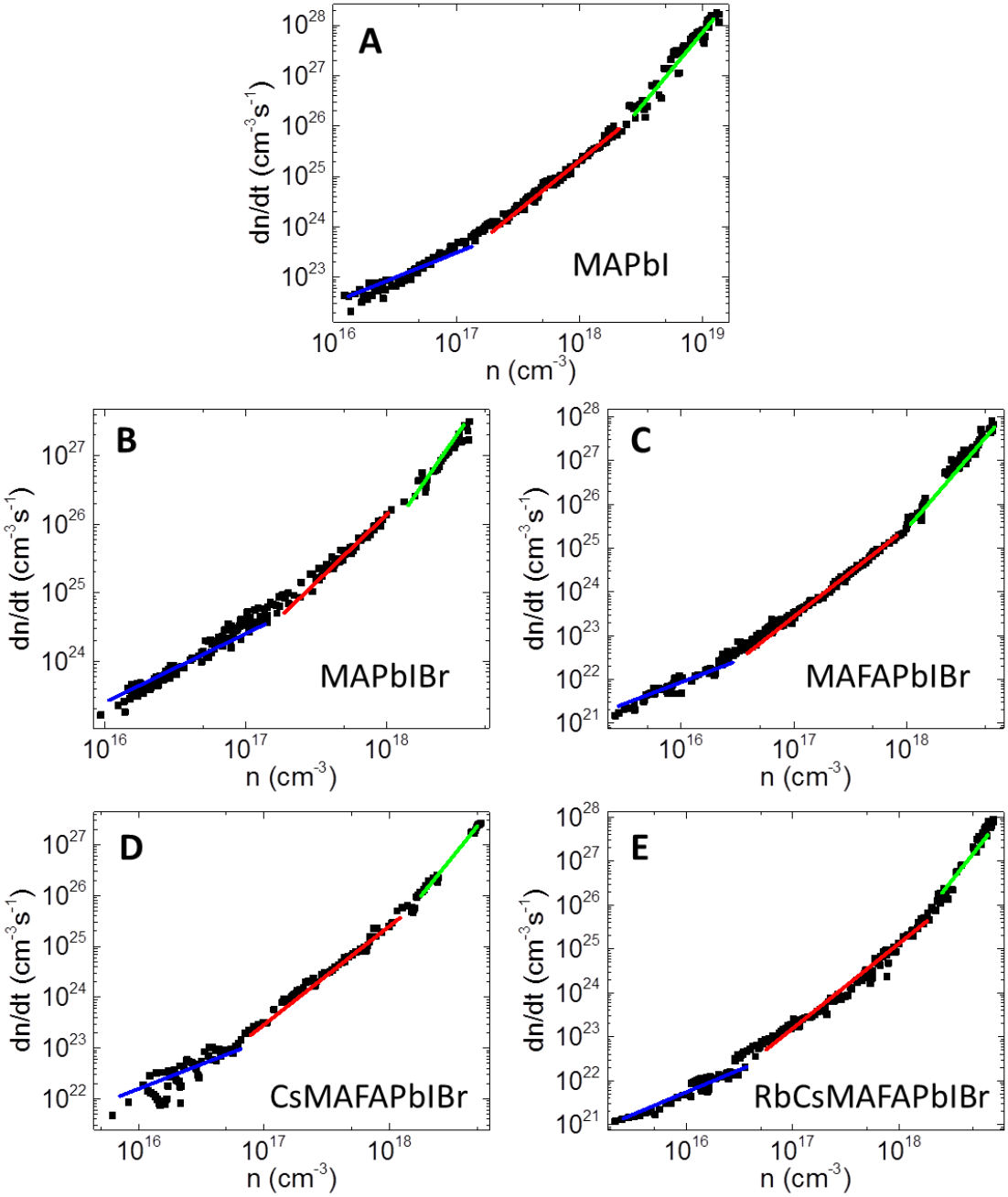

Figure 5.10 Recombination rate plotted against carrier density for all mixed cation perovskite samples. *Black squares indicate experimental data extracted from TA measurements on the (A) MAPbI, (B) MAPbIBr, (C) MAFAPbIBr, (D) CsMAFAPbIBr and (E) RbCsMAFAPbIBr mixed cation perovskite samples. Blue, red and green solid lines are guides to the eye with gradients of one, two and three, indicating the first, second and third-order recombination regimes respectively.*

In order to extract the recombination constants for each sample, the plots of recombination rate against carrier density should simply be fitted with Equation 5.1. However, since the data spans over multiple orders of magnitude, it is extremely difficult to fit. Therefore, we took the log of both the recombination rate and carrier density and fitted the data with Equation 5.3, as shown in Figure 5.11.

$$\log\left(\frac{dn(t)}{dt}\right) = \log\left(k_1 \cdot 10^{\log(n(t))} + k_2 \cdot 10^{2\cdot\log(n(t))} + k_3 \cdot 10^{3\cdot\log(n(t))}\right). \qquad 5.3$$

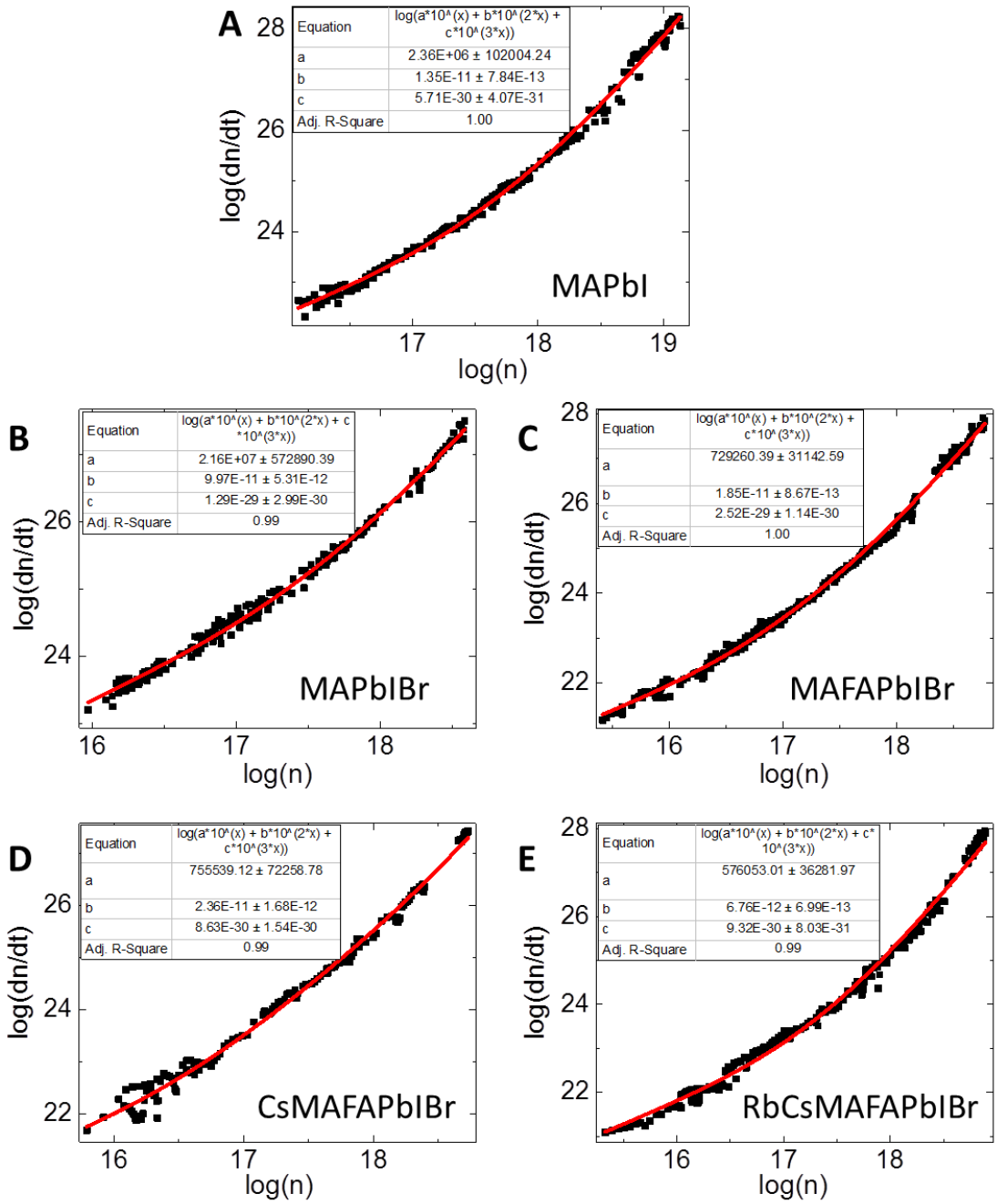

Figure 5.11 Fits of log(recombination rate) plotted against log(carrier density) for all mixed cation perovskite samples. *The values of a, b and c correspond to the first, second and third-order recombination constants* $\boldsymbol{k_1}$, $\boldsymbol{k_2}$ *and* $\boldsymbol{k_3}$ *respectively for the (A) MAPbI, (B) MAPbIBr, (C) MAFAPbIBr, (D) CsMAFAPbIBr and (E) RbCsMAFAPbIBr mixed cation perovskite samples.*

The recombination constants extracted from TA and TPL are shown in Table 5.2. The first-order recombination rate constant is largest in the MAPbIBr sample (2.2×10^{7} s^{-1} from TA and 3.1×10^{7} s^{-1} from TPL) and smallest in the RbCsMAFAPbIBr sample (6.0×10^{5} s^{-1} from TA and $<3.0\times10^{6}$ s^{-1} from TPL). This is in agreement with the significant variation in lifetime observed in the low excitation density TA and TPL measurements and indicates that the density of non-radiative first-order recombination pathways is smaller in the RbCsMAFAPbIBr sample than in the other mixed cation perovskite samples. This reduction in non-radiative recombination channels is likely to be the origin of the higher PLQEs and improved device performance observed in these materials[262].

Sample	k_1 (s^{-1})	k_2 ($cm^3\ s^{-1}$)	k_3 ($cm^6\ s^{-1}$)	k_1 from TPL (s^{-1})
MAPbI	2.4×10^{6}	1.3×10^{-11}	5.7×10^{-30}	$< 9.8\times10^{6}$
MAPbIBr	2.2×10^{7}	1.0×10^{-12}	1.3×10^{-29}	3.1×10^{7}
MAFAPbIBr	7.3×10^{5}	1.8×10^{-11}	2.5×10^{-29}	$< 3.4\times10^{6}$
CsMAFAPbIBr	7.6×10^{5}	2.4×10^{-11}	8.6×10^{-30}	$< 4.8\times10^{6}$
RbCsMAFAPbIBr	6.0×10^{5}	6.8×10^{-12}	9.3×10^{-30}	$< 3.0\times10^{6}$

Table 5.2 Table of the first, second and third-order recombination rates extracted from TA and TPL measurements. *Both the first-order and second-order recombination rates are reduced in the best performing RbCsMAFAPbIBr material, indicating a reduction in the density of undesirable non-radiative recombination pathways.*

It is also observed that the second-order recombination rate is smaller in the RbCsMAFAPbIBr sample than in the CsMAFAPbIBr, MAFAPbIBr and MAPbI sample. This reduction may originate from a decrease in the density of non-radiative second-order recombination pathways, which would again lead to an increase in the PLQE. Evidence for such non-radiative second-order recombination processes have been reported in the literature, but the origin of these processes is not yet clearly understood[152,266].

In addition to investigating the effect of mixed cations on recombination, we also used TA to investigate the effect of mixed cations on carrier cooling. According to the literature[137], in TA measurements on standard lead halide perovskites excited above the optical bandgap, a negative feature is observed at energies just below the optical bandgap within the first few picoseconds after photoexcitation. This feature arises from bandgap renormalisation due to the presence of free charge carriers. Bandgap renormalisation reduces the bandgap, enabling transitions to previously unavailable lower energy states. While these states are unoccupied, a negative photo-induced absorption is observed in TA. This feature decays as the photoexcited carriers cool from their high energy photoexcited states to the band edge. Therefore, the kinetics of this feature can be used to compare carrier cooling in the mixed cation perovskite samples.

The kinetics and corresponding TA maps for the mixed cation perovskite samples are shown in Figure 5.12. No significant differences in the carrier cooling were observed in the mixed cation perovskite samples, indicating that the fundamental photophysical properties of these materials are unchanged when organic and inorganic cations are incorporated into the lattice.

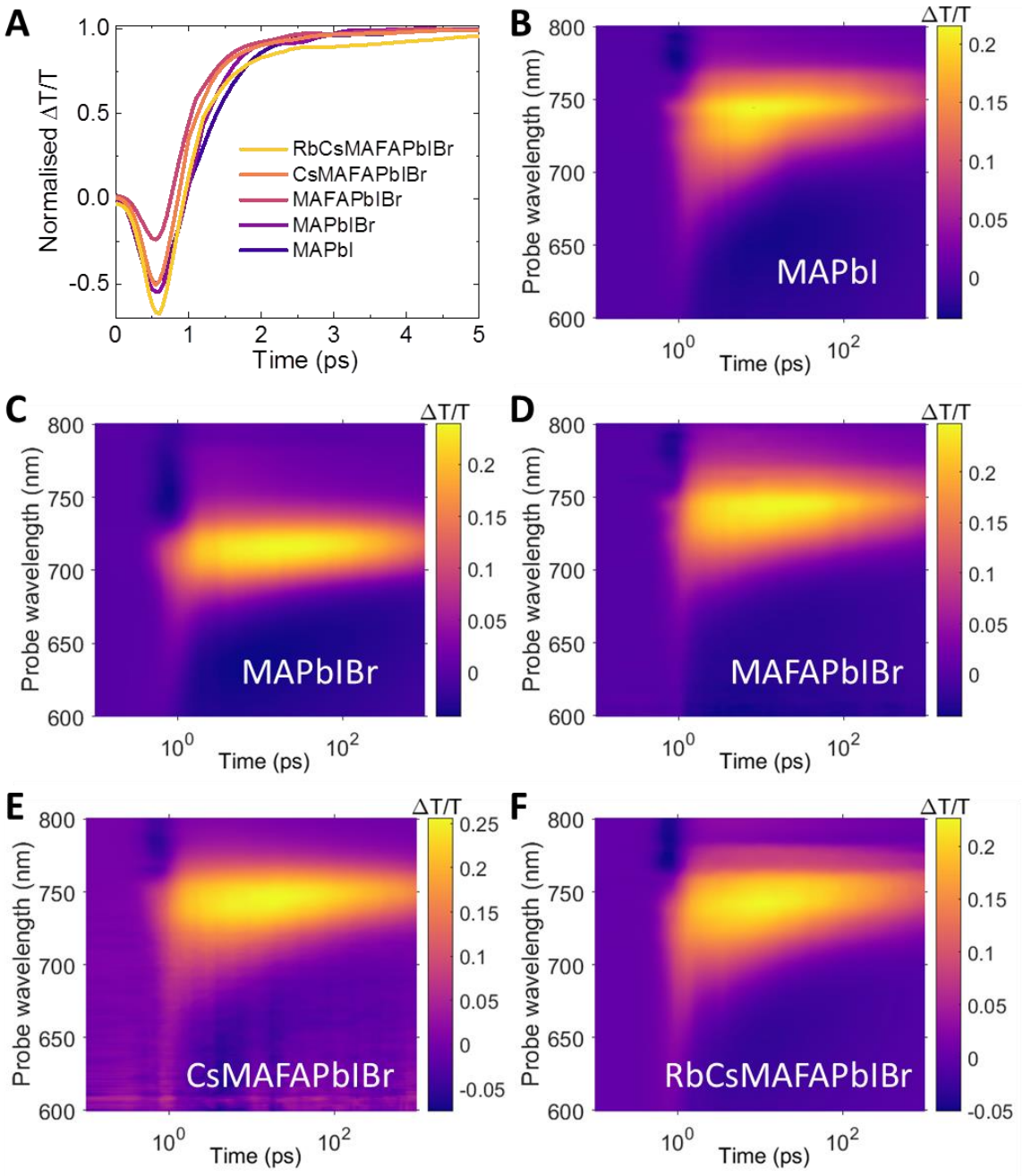

Figure 5.12 Carrier cooling in mixed cation perovskite samples. *(A) Kinetics of the below bandgap negative feature observed in the TA maps, integrated between 770-780 nm for the MAPbI, MAFAPbIBr, CsMAFAPbIBr and RbCsMAFAPbIBr samples and between 740-750 nm in the MAPbIBr sample. TA maps of the (B) MAPbI, (C) MAPbIBr, (D) MAFAPbIBr, (E) CsMAFAPbIBr and (F) RbCsMAFAPbIBr mixed cation perovskite samples. All samples were excited with a 400 nm laser (1 kHz repetition rate, ~90 fs pulse duration, ~25 meV FWHM) with a high photoexcitation density of ~10^{19} cm^{-3}.*

5.7 X-ray diffraction (XRD) of mixed cation perovskites

In order to gain insight into whether the lower first and second-order recombination rate constants observed in the RbCsMAFAPbIBr sample originate from structural changes in the material, x-ray diffraction was carried out by Tudor Thomas, Edward Booker and Tim van de Goor using the method described in detail in Section 3.2.3. The results are plotted in Figure 5.13.

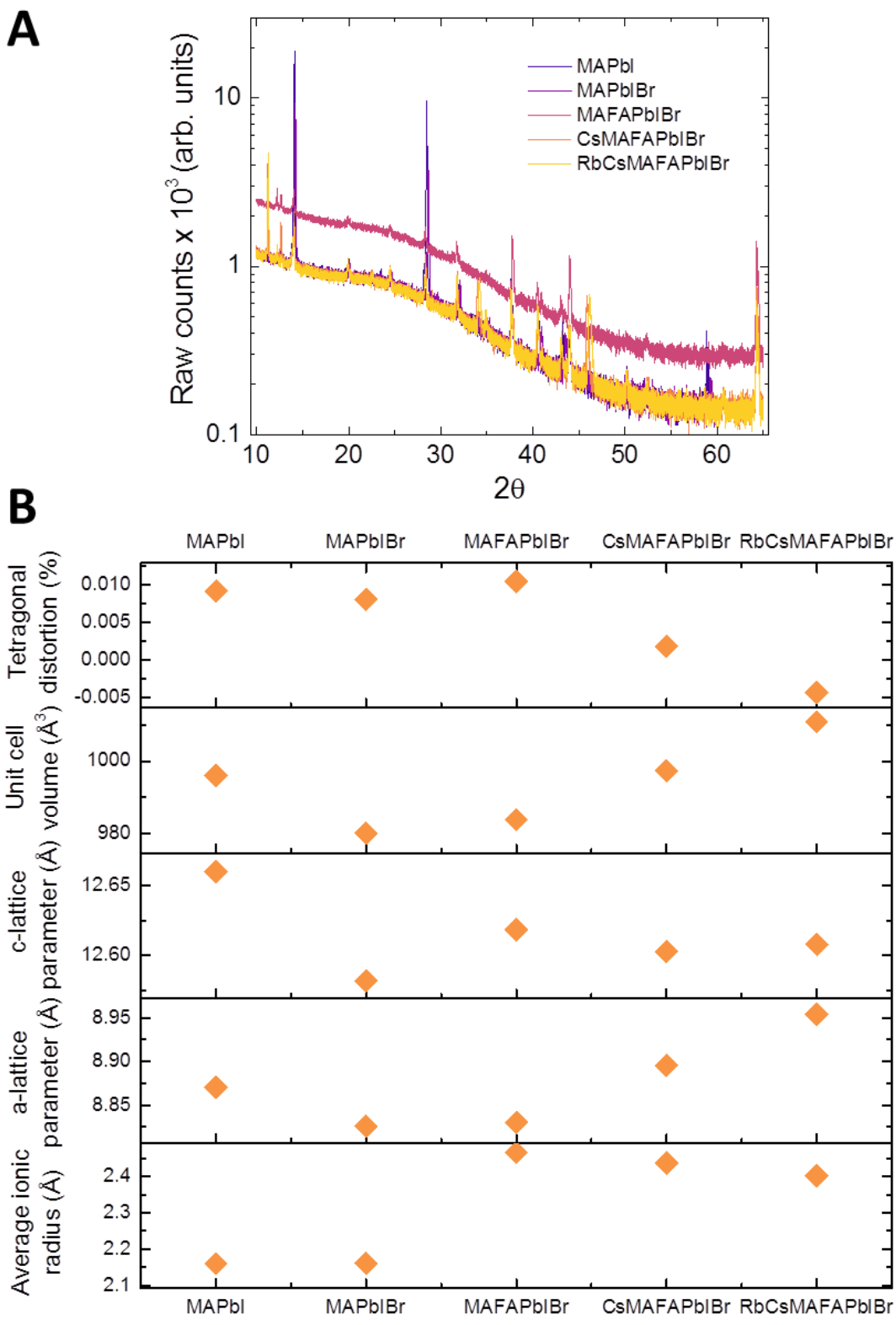

Figure 5.13 X-ray diffraction (XRD) of mixed cation perovskites samples. *(A) XRD patterns and (B) extracted structural properties of MAPbI, MAPbIBr, MAFAPbIBr, CsMAFAPbIBr and RbCsMAFAPbIBr samples. Measurements were carried out by Tudor Thomas, Edward Booker and Tim van de Goor.*

According to previous literature[267–269], MAPbI adopts a tetragonal crystal structure at room temperature with space-group I4/mcm. The addition of Br to MAPbI decreases the tetragonal distortion and acts to make the unit cell lattice parameters of MAPbIBr closer to those of the cubic perovskite $MAPbBr_3$[269]. The a-lattice parameter does not change substantially, whereas the c-lattice parameter roughly obeys Vegard's law for solid solutions upon incorporation of Br[269]. The addition of the bulky organic $(NH_2)_2CH^+$ cation to MAPbIBr increases both the a-parameter and the c-parameter of MAFAPbIBr, whereas the addition of the smaller Cs and Rb cations to MAFAPbIBr increases the a-parameter and decreases the c-parameter.

The lattice parameters and symmetry of the unit cells are strongly dependent on the mean ionic radii of the mixed cations. The square base of the tetragonal cell increases linearly with mean ionic radius, due to steric effects, which results in a decrease in the c-lattice parameter. It also leads to an increase in tetragonal strain, with the intermediate sample CsMAFAPbIBr being close to a cubic unit cell. No additional perovskite phases are observed in any of the materials and there is no obvious trend in lattice strain, which might be expected as the stoichiometry becomes more complicated.

5.8 Raman spectroscopy of mixed cation perovskites

In order to gain insight into whether the lower first and second-order recombination rate constants observed in the RbCsMAFAPbIBr sample originate from changes in the material dynamics, resonant-Raman spectroscopy was carried out by Tudor Thomas using the method described in detail in Section 3.2.2. The resulting resonant-Raman spectra are shown in Figure 5.14.

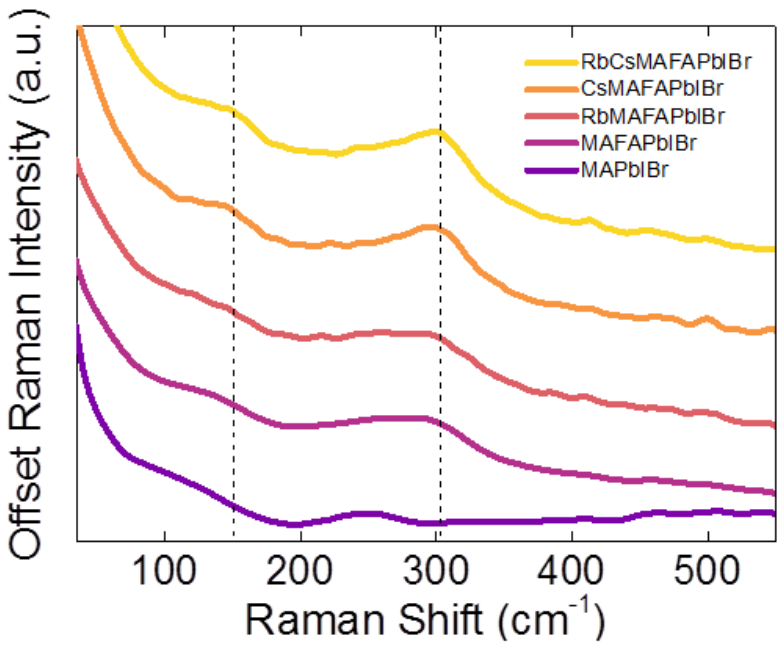

Figure 5.14 Resonant-Raman spectra of mixed cation perovskites. *The peaks at ~150 cm^{-1} and ~300 cm^{-1} are assigned to $CH_3NH_3^+$ and $(NH_2)_2CH^+$ libration respectively. The large shoulder observed at low wavenumbers arises from Rayleigh scattering of the incident laser. Previously reported peaks at <100 cm^{-1} arising from sample degradation were not observed. All measurements were carried out by Tudor Thomas.*

According to previous literature, the peak observed at ~150 cm^{-1} arises from $CH_3NH_3^+$ libration[220,270]. This peak becomes increasingly shifted to higher wavenumbers as the sample composition changes from MAPbIBr, MAFAPbIBr, CsMAFAPbIBr to RbCsMAFAPbIBr and the equivalent bond-constant for the vibration increases. This is consistent with the reduction in size of the unit-cell upon incorporation of the heavy metals, decreasing the relative ease of organic libration. A second peak at ~300 cm^{-1} is assigned to $(NH_2)_2CH^+$ libration, through comparison with the $CH_3NH_3^+$ bond-constant and the observation that this peak is only present in samples which contain $(NH_2)_2CH^+$. This peak also stiffens, and increases in sharpness as the unit-cell decreases in volume with the addition of multiple cations, indicating an increased homogeneity of the unit cell with the addition of multiple cations, consistent with the results from the TA and TPL measurements.

5.9 Conclusions and future work

In this chapter, we have shown that the origin of the excellent RbCsMAFAPbIBr perovskite device performance[59,271] is likely to be due to the reduction in the density of non-radiative first and second-order recombination pathways observed in these materials. Using TA and TPL spectroscopies, we showed that the first-order recombination rate constant is reduced by almost two orders of magnitude from $2.2x10^7$ s^{-1} in MAPbIBr to $6.0x10^5$ s^{-1} in RbCsMAFAPbIBr. This is consistent with previous reports where the addition of triiodide ions to $FAPbI_3$ films containing small amounts of $MAPbBr_3$ was found to surpass the formation of deep-level defects[6]. This reduction in non-radiative recombination is likely to be the origin of the enhanced PLQEs observed in the mixed cation perovskite samples, increasing from 2.7% in the MAPbIBr sample to 26.4% in the RbCsMAFAPbIBr sample. XRD and Raman spectroscopy measurements indicate that the lattice volume increases upon the addition of FA, Cs and Rb. Reports on similar materials[265] indicate that this increase in lattice volume may reduce lattice strain, resulting in improved optoelectronic performance and increased photo-stability.

Further work will be done on these materials to investigate in more detail the role the mixed cations on the crystal lattice. TA and TPL microscopy will also be carried out in order to determine whether there are local differences in the first, second and third-order

recombination rates and whether they correlate with regions of higher and lower PLQEs.

6 Recombination in additive-controlled lead halide perovskites

In this chapter, we use TA, TPL, PLQE and XRD to study the how the photophysical properties of lead halide perovskites change when organic additives of different sizes and polarities are incorporated into the crystal lattice. It has been shown by Muyang Ban and others in the group of Baoquan Sun at Soochow University, that using selected organic additives to control lead halide perovskite crystallisation can significantly improve the efficiency of perovskite LEDs, resulting in devices with over 15% EQE. By studying the radiative recombination channels in these materials using TA and TPL, we show that this enhancement in efficiency is most likely due to an energy funnelling effect, arising from the dimensional modulation of the three-dimensional perovskite crystal structure into a layered quasi-two-dimensional perovskite crystal structure. This energy funnelling effect appears to localise charge carriers in the material, resulting in a change in the dominant radiative recombination process from second-order to first-order and an enhancement in the PLQE. The sample fabrication, steady-state absorption, XRD and device fabrication in this chapter were carried out by Muyang Ban and others in the group of Baoquan Sun at Soochow University.

6.1 Background and motivation

The outstanding developments in lead halide perovskite solar cells have prompted research into other potential applications for these materials, including lead halide perovskite light-emitting diodes (LEDs). The first lead halide perovskite LED, with an EQE of less than 1%[7], was reported in 2014. Since then, a number of key developments, summarised in Table 6.1 on Page 147, have led to the fabrication of lead halide perovskite LEDs with EQEs of up to 11.7%.

In this chapter, we discuss the photophysical properties of additive-controlled $CsPbBr_3$ perovskites, which were synthesised and incorporated into record-breaking perovskite LEDs – with EQEs of up to 15.5% – by Muyang Ban and others in the group of Baoquan Sun at Soochow University. By incorporating the organic molecules phenethylamine bromide (PEABr) and a chemical additive with an electron-rich -O-C-O- chemical bond (-O-C-O-) into the $CsPbBr_3$ perovskite lattice, high efficiency and large area (1x1.5 cm^2) green emitting (515 nm) devices were achieved, as shown in Figure 6.1. A batch of 42 devices containing both PEABr and -O-C-O- additives, had an average EQE of ~13%. Devices fabricated with both PEABr and -O-C-O- additives also exhibited increased stability compared to devices fabricated with only PEABr additives.

Such high efficiencies are typically difficult to achieve, because the charge carriers in lead halide perovskites have low exciton binding energies and high diffusivity, leading to reduced radiative recombination rates. These radiative recombination pathways are in constant competition with non-radiative recombination pathways, such as recombination with grain boundary defects or other trap states. Therefore, lead halide perovskite PLQEs are highly dependent on both trap density and carrier density.

Under normal LED operating conditions, the carrier densities injected into lead halide perovskite LEDs are usually lower than the trap densities in these materials, resulting in low PLQEs and device efficiencies. In an attempt to increase the injected carrier densities, devices have been fabricated with very thin (~20 nm) lead halide perovskite layers. However, in such thin layers, pinholes are inevitable, resulting in poor device performance[7]. Other approaches, such as spatially confining injected charge carriers within engineered lead halide perovskite nanograins, have led to devices with EQEs of 8.5%[272]. This approach is reasonably effective in bromide perovskites, but is generally

not as effective in iodide perovskites, in which the exciton binding energy is often lower[125].

Table removed for copyright reasons.

Table 6.1 Table of the highest efficiency perovskite LEDs reported in the literature since 2014, adapted from reference 8. *Our highest performing device had an EQE of 15.5%, which is almost 5% higher than any previously reported perovskite LED.*

Figure 6.1 Additive-controlled lead halide perovskite LEDs, taken from reference 8. *(A) A 1x1.5 cm^2 $CsPbBr_3$ perovskite LED, containing both PEABr and -O-C-O- additives, operating at 4V. (B) Normalised electroluminescence spectrum from $CsPbBr_3$ devices containing only PEABr and both PEABr and -O-C-O- additives, centred around 515 nm. (C) Histogram of the EQEs of 42 40% PEABr--O-C-O--KBr LEDs, with an average EQE of ~13%. (D) Normalised EQE of $CsPbBr_3$ devices containing only PEABr and both PEABr and -O-C-O- additives. Devices were operated at 3.5 V for 100 s. Significant degradation was observed in the $CsPbBr_3$ device containing only the PEABr additive, while the $CsPbBr_3$ device containing both PEABr and -O-C-O- additives was relatively stable.*

In order to improve device efficiencies further, a new strategy has been proposed, in which the dimensionality of the lead halide perovskite lattice is modulated by incorporating organic additives into the lattice[74–77]. By modulating the dimensionality of the lead halide perovskite lattice, the energy landscape of the material can be engineered, so that charge carriers efficiently funnel into lower energy sites and become strongly concentrated in localised regions of the material. It has been shown that such energy funnelling can effectively outcompete non-radiative recombination, resulting in excellent PLQEs and device performance.

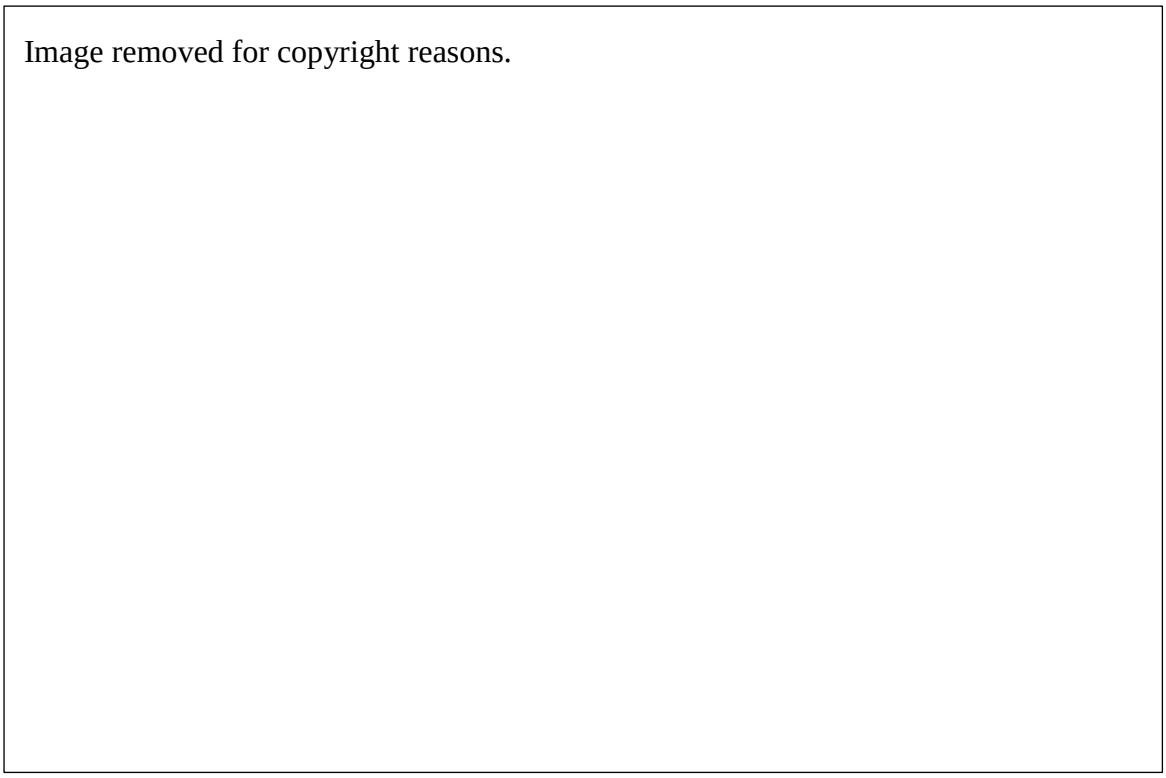

Figure 6.2 Diagrams demonstrating how dimensional modulation of the lead halide perovskite lattice can alter the energy landscape and result in efficiency energy funnelling, all taken from reference 75. *(A) In bulk three-dimensional perovskites, the low exciton binding energy and high diffusivity of charge carriers results in low radiative recombination rates. (B) In quasi-two-dimensional perovskites, non-radiative recombination processes compete with radiative recombination processes. (C) In an engineered quasi-two-dimensional perovskite system, energy funnelling can occur faster than non-radiative recombination, leading to an increase in PLQE and device performance. (D) In a flat energy landscape, significant non-radiative recombination may occur. (E) In an engineered energy landscape, strong funnelling may outcompete non-radiative recombination. (F) Energy funnelling results in higher PLQEs at lower carrier densities.*

The excellent device efficiencies achieved by the group of Baoquan Sun at Soochow University, indicate that similar energy funnelling processes may be occurring in our additive-controlled lead halide perovskites. By combining results from photoluminescence quantum efficiency (PLQE), transient photoluminescence (TPL), transient absorption (TA), x-ray diffraction (XRD) spectroscopies we aim to investigate the role of energy funnelling processes in these materials and develop an understanding of how energy funnelling processes can be controlled to further improve device performance. This will be the focus of this chapter.

6.2 Preparation of additive-controlled perovskites

All additive-controlled perovskites were prepared by the group of Baoquan Sun at Soochow University, using the methods described in detail in Section 3.1.3. Throughout this chapter we use the nomenclature 0% PEABr, 40% PEABr, 40% PEABr--O-C-O- and 40% PEABr--O-C-O--KBr to refer to the complete $CsPbBr_3$ perovskite compounds containing various combinations of the phenethylamine bromide (PEABr), a chemical additive with an electron-rich -O-C-O- chemical bond (-O-C-O-) and potassium bromide (KBr) additives. We chose to study only materials containing a 40% ratio of PEABr, as these materials exhibited the highest PLQEs and device efficiencies[8]. The full details of the chemical additive with an electron-rich -O-C-O- chemical bond (-O-C-O-) will be published shortly[8].

6.3 Steady-state absorption and steady-state photoluminescence of additive-controlled perovskites

In order to investigate the effect of the PEABr and -O-C-O- additives on the optical properties of the $CsPbBr_3$ perovskite, steady-state absorption and photoluminescence spectra were measured by the group of Baoquan Sun. The steady-state absorption and photoluminescence spectra of 0% PEABr, 40% PEABr and 40% PEABr--O-C-O- are shown in Figure 6.3. The 40% PEABr--O-C-O--KBr spectra are indistinguishable from the 40% PEABr--O-C-O- spectra.

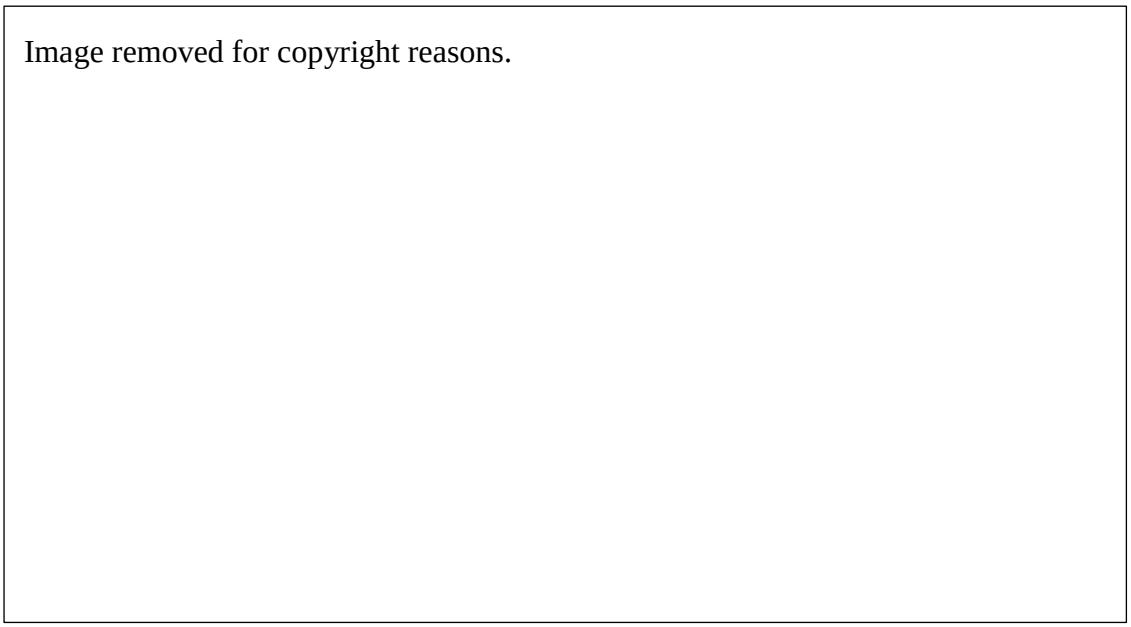

Figure 6.3 Steady-state absorption and photoluminescence of $CsPbBr_3$ with PEABr and -O-C-O- additives, taken from reference 8. *(A) Steady-state absorption spectra and (B) steady-state photoluminescence spectra for 0% PEABr (red lines) and 40% PEABr (black lines) samples with (dotted lines) and without (solid lines) -O-C-O-.*

In the 0% PEABr sample, an exciton-like absorption peak is observed at ~520 nm. This peak reduces in intensity as the percentage of PEABr is increased and is barely visible in the 40% PEABr sample. This reduction in intensity is consistent with a reduction in the interaction between charge carriers. As the percentage of PEABr is increased from 0% to 40%, new absorption peaks also appear at ~405 nm, ~436 nm and ~467 nm. Such peaks have been assigned in the literature to n = 1, 2 and 3 perovskite nanoplatelets, where n corresponds to the number of perovskite unit cells stacked in the nanoplatelet[277]. The intensity of these peaks reduce when -O-C-O- is added. The appearance of these peaks suggest the formation of an ensemble of differently sized nanocrystalline regions, which is modified by the addition of -O-C-O-.

Despite the significant changes observed in the steady-state absorption spectra, the steady-state photoluminescence spectra remain similar as the percentage of PEABr is increased from 0% to 40%. There is a slight peak shift from ~525 nm in the 0% PEABr sample to ~515 nm in the 40% PEABr sample, consistent with the slight blue shift observed in the main absorption peak at ~520 nm, and most likely due a reduction in the mean of the grain size distribution. Although photoexcitation was carried out with a 365 nm laser, no additional features associated with the higher energy absorption peaks are observed, indicating that emission from the thinner nanoplatelets is negligible compared to the dominating photoluminescence observed from the thicker nanoplatelets (n > 15) and three-dimensional regions. This suggests that energy is efficiently funnelled from smaller, higher energy regions of the sample to larger, lower energy regions of the sample before radiative recombination occurs.

6.4 Photoluminescence quantum efficiency (PLQE) of additive-controlled perovskites

As discussed in Section 5.4, materials with higher PLQEs usually perform better in devices, because recombination is more likely to occur through desirable radiative pathways rather than undesirable non-radiative pathways[165]. The PLQEs of the additive-controlled perovskites were measured by the group of Baoquan Sun and are shown in Table 6.2. The PLQEs vary by almost two orders of magnitude from <1% in the 0% PEABr sample to 70% in the 40% PEABr--O-C-O- sample.

Sample	PLQE (%)
0% PEABr	< 1%
40% PEABr	23%
40% PEABr--O-C-O-	70%
40% PEABr--O-C-O--KBr	71%

Table 6.2 Table of the PLQEs of the additive-controlled perovskites. *All samples were excited with a 365 nm laser with an intensity of ~2.3 mW cm^{-2}. Measurements were carried out by the group of Baoquan Sun.*

6.5 Transient photoluminescence (TPL) of additive-controlled perovskites

In order to understand why the PLQE of the 40% PEABr--O-C-O- sample was significantly higher than the PLQEs of the 40% PEABr and 0% PEABr samples we carried out TPL measurements on these samples and the 40% PEABr--O-C-O--KBr sample. The low excitation density (~10^{16} cm^{-3}) TPL spectra and kinetics are plotted in Figure 6.4. The 0% PEABr spectrum is slightly red shifted compared to the other samples, consistent with the steady-state absorption and photoluminescence measurements. But the 40% PEABr, 40% PEABr--O-C-O- and 40% PEABr--O-C-O--KBr spectra are all centred at ~518 nm, suggesting that radiative recombination in these materials occurs dominantly in thicker nanoplatelets (n > 15) and three-dimensional regions.

Despite the similarities observed in the TPL spectra, the TPL kinetics vary significantly, with lifetimes ranging from <5 ns in the 0% PEABr sample to ~58 ns in the 40% PEABr--O-C-O--KBr. The observed combination of a longer photoluminescence lifetime and an increased PLQE, suggest that the density of non-radiative recombination pathways and therefore the non-radiative recombination rate is reduced when PEABr, PEABr--O-C-O- and PEABr--O-C-O--KBr are added to standard $CsPbBr_3$ perovskites.

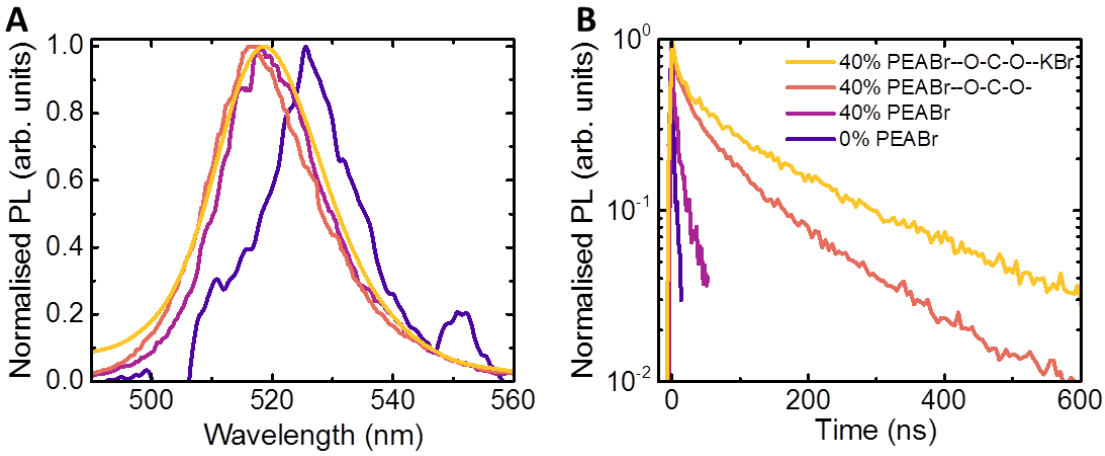

Figure 6.4 Transient photoluminescence (TPL) spectra and kinetics of additive-controlled perovskite samples. (A) The TPL spectra, temporally integrated over the first 10 ns after photoexcitation, are centred at ~518 nm for all samples except for the 0% PEABr sample which is centred at ~526 nm. (B) The TPL kinetics, spectrally integrated over the TPL spectra, exhibit lifetimes of <5 ns, ~8 ns, ~36 ns and ~58 ns for the 0% PEABr, 40% PEABr, 40% PEABr--O-C-O- and 40% PEABr--O-C-O--KBr samples respectively. All samples were photoexcited with a 400 nm laser (1 kHz repetition rate, ~90 fs pulse duration, ~25 meV FWHM) with a photoexcitation density of ~10^{16} cm^{-3}.

The excitation density dependent TPL kinetics, spectrally integrated over the TPL spectrum, are plotted in Figure 6.5. The lifetime of the 0% PEABr sample is shorter than the time resolution of the ICCD setup, so it is not possible to compare the lifetimes at different excitation densities. In the 40% PEABr, 40% PEABr--O-C-O- and 40% PEABr--O-C-O--KBr samples, the photoluminescence lifetimes seem independent of excitation density below excitation densities of ~10^{18} cm^{-3}. At higher excitation densities, the photoluminescence lifetimes become shorter with increasing excitation densities. This indicates a transition in the dominant recombination mechanism from a first-order process at low and mid excitation densities to a higher-order process at high excitation densities.

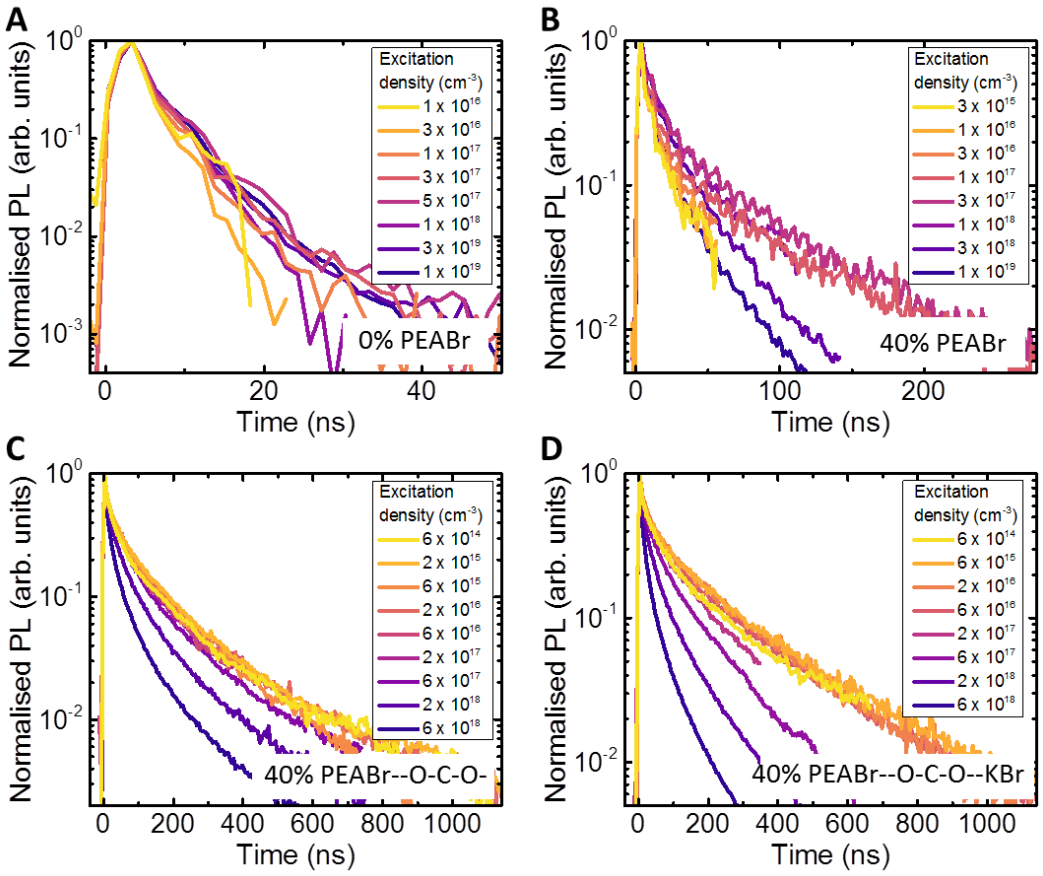

Figure 6.5 Transient photoluminescence (TPL) kinetics of additive-controlled perovskite samples. *The TPL kinetics, spectrally integrated over the TPL spectra, are measured with a 400 nm laser (1 kHz repetition rate, ~90 fs pulse duration, ~25 meV FWHM) for the (A) 0% PEABr, (B) 40% PEABr, (C) 40% PEABr--O-C-O- and (D) 40% PEABr--O-C-O--KBr samples. The photoluminescence lifetime of the 0% PEABr sample is shorter than the time resolution of the ICCD setup, so cannot be resolved.*

As described in Section 2.2.2.3.4, recombination $\left(-\frac{dn(t)}{dt}\right)$ in lead halide perovskites can be described by a sum of first, second and third-order processes, with first, second and third-order recombination rate constants k_1, k_2 and k_3 respectively[125,147,151,261,262]. Different radiative and non-radiative recombination processes dominate recombination at different excitation densities $n(t)$, as shown in Equation Figure 6.1.

$$-\frac{dn(t)}{dt} = k_1 \cdot n(t) + k_2 \cdot n(t)^2 + k_3 \cdot n(t)^3. \quad 6.1$$

At any given time t, the observed TPL signal $\mathrm{TPL}(t)$ scales with the radiative recombination rate $\left(-\frac{\mathrm{d}n(t)}{\mathrm{d}t}\right)_{rad}$ at that time,

$$\mathrm{TPL}(t) \sim \left(-\frac{\mathrm{d}n(t)}{\mathrm{d}t}\right)_{rad}. \quad 6.2$$

Therefore, the TPL kinetics decrease as $n(t)$ decreases, independent of whether $n(t)$ decreases through a radiative or non-radiative process.

In order to determine whether radiative recombination is a first, second or third-order process, the TPL signal is plotted against the carrier density, $n(t)$. This is achieved by measuring the TPL signal immediately after photoexcitation PL_0, when the carrier density can be calculated from the experimental parameters such as the laser wavelength, power and spot size, as described in Section 2.5.2. Plots of PL_0 against carrier density for the additive-controlled perovskite samples are shown in Figure 6.6. Interestingly, the dominant radiative recombination process seems to be second-order only in the 0% PEABr sample. In the 40% PEABr, 40% PEABr--O-C-O- and 40% PEABr--O-C-O--KBr samples, the dominant radiative recombination process seems to be first-order.

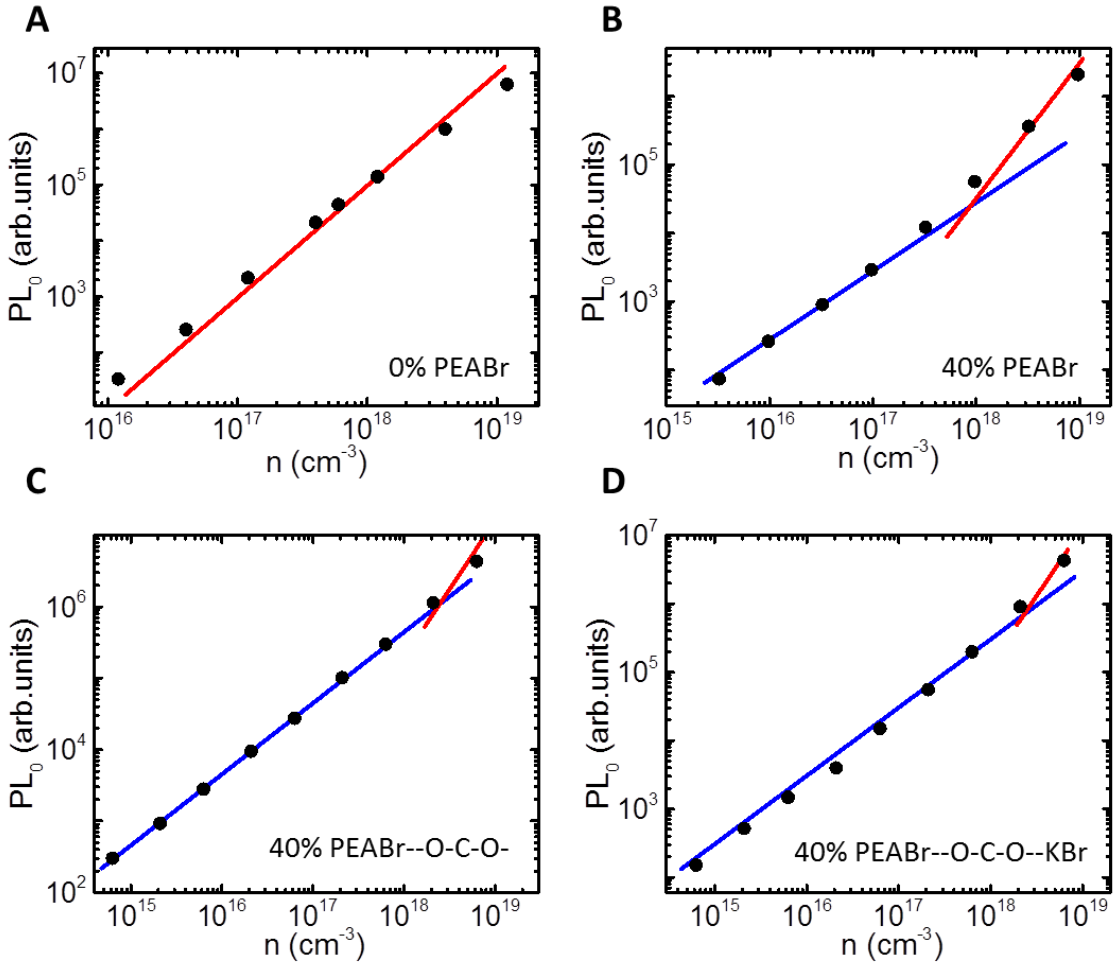

Figure 6.6 Initial TPL signal (PL_0) plotted against excitation density (n) for the additive-controlled perovskite samples. *PL_0 (black circles) scales quadratically with carrier density only in the (A) 0% PEABr sample. In the (B) 40% PEABr, (C) 40% PEABr--O-C-O- and (D) 40% PEABr--O-C-O--KBr samples, PL0 scales linearly with carrier density, except when the excitation density is higher than ~10^{18} cm^{-3}. Red and blue lines are guides to the eye indicating quadratic and linear dependencies respectively. All samples were photoexcited with a 400 nm laser (1 kHz repetition rate, ~90 fs pulse duration, ~25 meV FWHM).*

In typical three-dimensional lead halide perovskites, radiative recombination is always a second-order process arising from band-to-band recombination of free carriers[152,263–265]. This is a second-order process, since doubling the number of charge carriers quadruples the number of ways the carriers can recombine. First-order radiative recombination is only observed in lead halide perovskite nanocrystals, at excitation densities lower than the density of nanocrystals, such that each nanocrystal contains no more than a single photoexcited charge carrier pair[155–157]. This is a first-order process, since doubling the number of charge carriers only doubles the recombination rate, because the charge carrier pairs are localised and can only recombine geminately. We confirmed this behaviour by plotting the initial TPL signal against carrier density for a film of $CsPbI_3$ nanocrystals prepared by Nathaniel Davis using the method described in detail in Section 3.1.1.2. As shown in Figure 6.7, the radiative recombination rate scales linearly with laser power, indicating that radiative recombination is dominated by a first-order process.

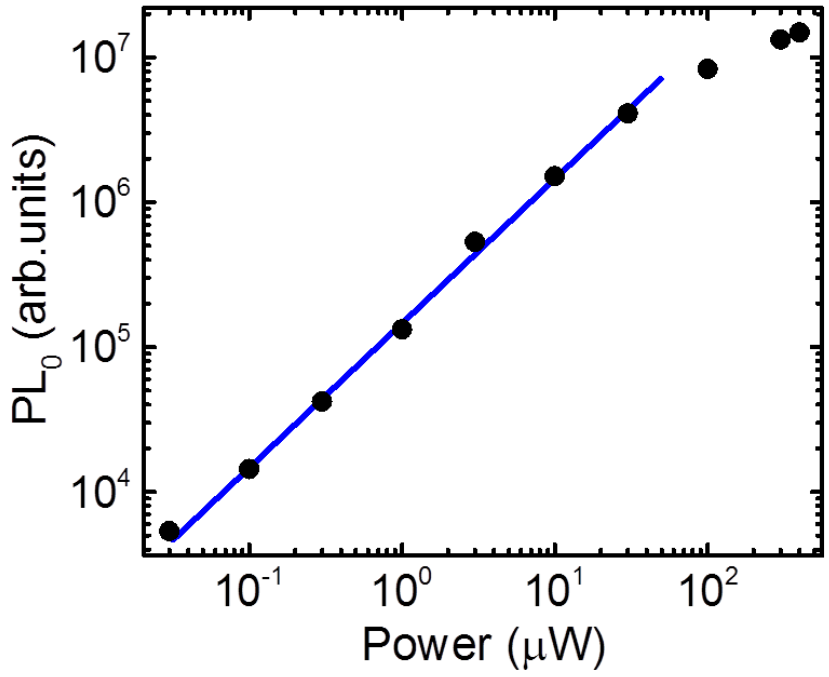

Figure 6.7 Initial TPL signal (PL_0) plotted against excitation density (n) for a film of $CsPbI_3$ nanocrystals. *PL_0 (black circles) scales linearly with laser power. Blue line is a guide to the eye indicating the linear dependence. PL_0 is spectrally integrated over the TPL spectrum, between 640-740 nm. The sample was photoexcited with a 400 nm laser (1 kHz repetition rate, ~90 fs pulse duration, ~25 meV FWHM) with a beam diameter (FWHM) of 600×580 μm.*

The observation that radiative recombination is dominated by a first-order process indicates that the 40% PEABr, 40% PEABr--O-C-O- and 40% PEABr--O-C-O--KBr samples are not typical three-dimensional lead halide perovskite materials. Instead, it suggests that these materials consist of nanocrystalline regions in which charge carriers are localised. This is in agreement with the steady-state absorption spectra, which indicate that these materials consist of nanoplatelets of different thicknesses. Since emission from thinner nanoplatelets is not observed in the steady-state or TPL spectra, it is likely that efficient energy funnelling is occurring from the higher energy thinner nanoplatelets into the lower energy thicker nanoplatelets ($n > 15$) and three-dimensional regions. Once the charge carriers are localised on these thicker nanoplatelets ($n > 15$) and three-dimensional regions, it appears that efficient first-order radiative recombination occurs.

6.6 Transient absorption (TA) of additive-controlled perovskites

Next we carried out TA measurements on the additive-controlled perovskite samples in order to extract the first, second and third-order recombination constants and to confirm which recombination processes dominate at which carrier densities. All measurements were done according to the method described in detail in Section 3.3.3. Typical spectra and kinetics for each additive-controlled perovskite sample are shown in Figure 6.8.

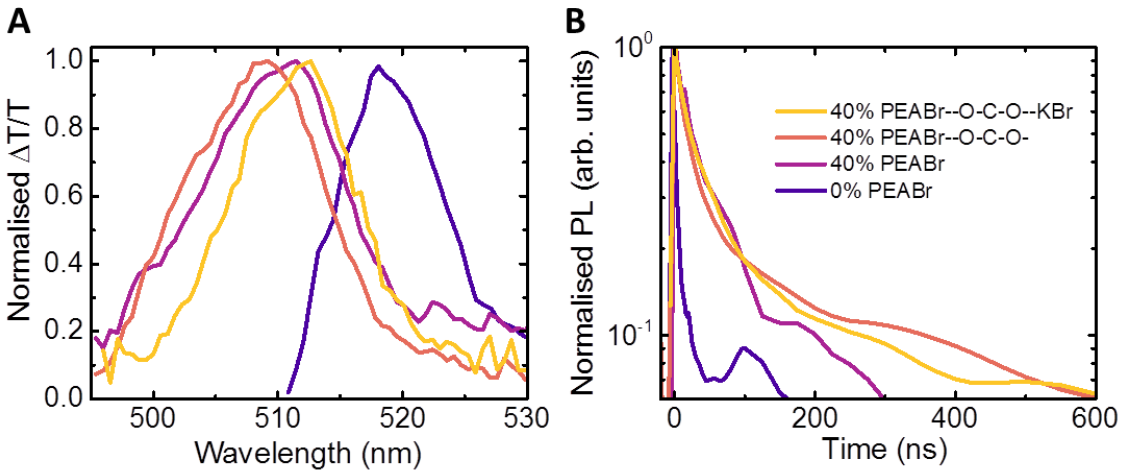

Figure 6.8 Transient absorption (TA) spectra and kinetics of additive-controlled perovskite samples. *(A) The ground state bleaches (GSB) of the TA spectra, temporally integrated over the first 10 ns after photoexcitation, are centred at 518 nm, 511 nm, 509 nm and 512 nm for the 0% PEABr, 40% PEABr, 40% PEABr--O-C-O- and 40% PEABr--O-C-O--KBr samples respectively. (B) The TA kinetics, spectrally integrated over the GSB, exhibit lifetimes (1/e) of around 7 ns, 43 ns, 34 ns and 44 ns for the 0% PEABr, 40% PEABr, 40% PEABr--O-C-O- and 40% PEABr--O-C-O--KBr samples respectively. All samples were excited with a 532 nm laser (500 Hz repetition rate, ~2 ns pulse duration, ~25 meV FWHM) with excitation density ~10^{16} cm^{-3}.*

The dominant feature in every TA spectrum is the positive ground state bleach (GSB) signal, arising from phase-space filling by photoexcited carriers[137,162,138], which is observed at around 520 nm in the 0% PEABr sample and at around 510 nm in all the other samples. The lifetime of the GSB signal varies significantly for different sample compositions, with the 0% PEABr sample having a lifetime of around only 7 ns and the 40% PEABr--O-C-O--KBr sample having a lifetime of around 44 ns, at an excitation density of ~10^{16} cm^{-3}. This spectral shift and increase in lifetime is consistent with the TPL measurements.

The first, second and third-order recombination constants were extracted from the TA data by plotting the recombination rate $-\frac{dn(t)}{dt}$ against carrier density $n(t)$ for each additive-controlled perovskite sample, as shown in Figure 6.9. As reported in the literature[152], a good estimate of the carrier density as a function of time can be achieved by integrating over the GSB as a function of time and then scaling this to the initial excitation density calculated from the experimental parameters such as the laser wavelength, power and spot size, as described in Section 2.2.2.3.4. Once the carrier density as a function of time is known, the recombination rate is calculated simply by taking the derivative of the carrier density with respect to time. This recombination rate is then plotted against carrier density to generate the plots in Figure 6.9.

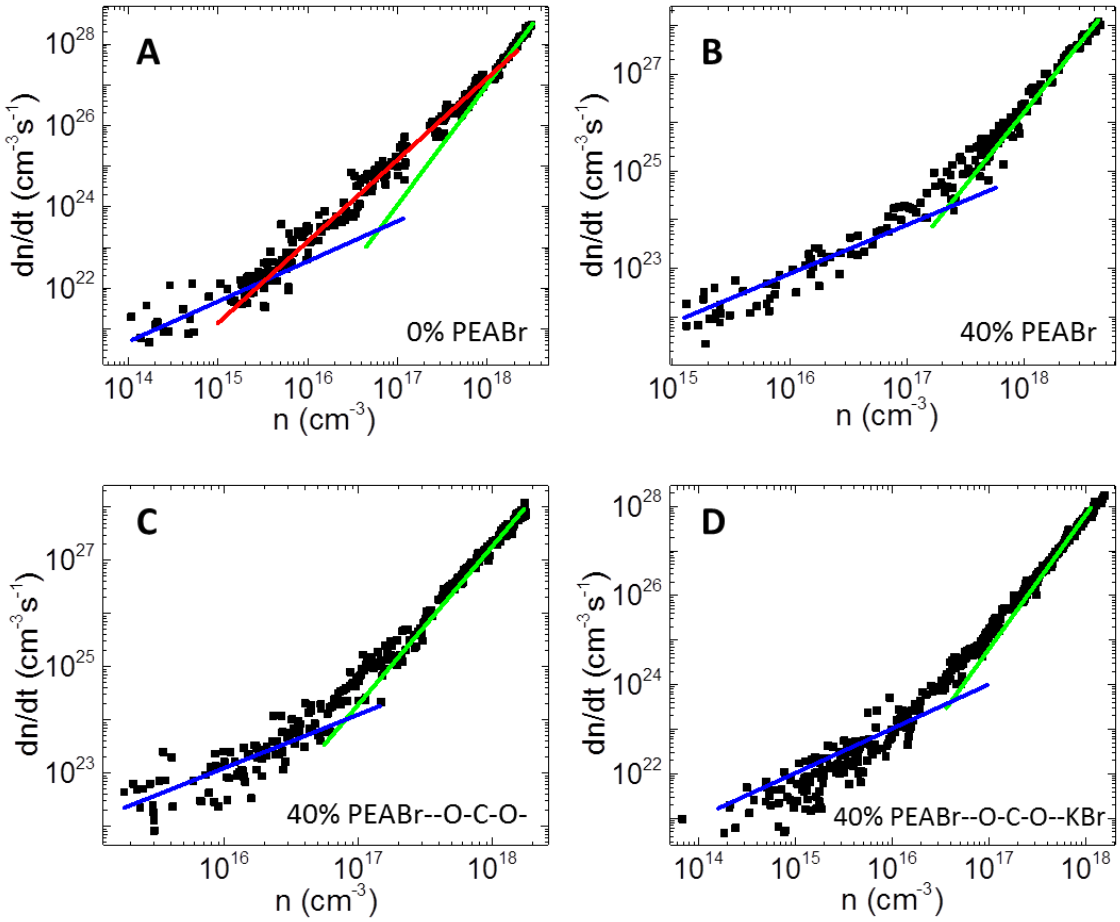

Figure 6.9 Recombination rate plotted against carrier density for all additive-controlled perovskite samples. *Black squares indicate experimental data extracted from TA measurements on the (A) 0% PEABr, (B) 40% PEABr, (C) 40% PEABr--O-C-O- and (D) 40% PEABr--O-C-O--KBr additive-controlled perovskite samples. Blue, red and green solid lines are guides to the eye with gradients of one, two and three, indicating the first, second and third-order recombination regimes respectively. Recombination in the 0% PEABr sample is clearly dominated by a second-order process between excitation densities of ~10^{15}-10^{18} cm^{-3}. However, it is not clear that a second-order process dominates recombination at any excitation density in the 40% PEABr, 40% PEABr--O-C-O- and 40% PEABr--O-C-O--KBr samples.*

In order to extract the recombination constants for each sample, the plots of recombination rate against carrier density should simply be fitted with Equation 6.1. However, since the data spans over multiple orders of magnitude, it is extremely difficult to fit. Therefore, we took the log of both the recombination rate and carrier density and fitted the data with Equation 6.3, as shown in Figure 6.10.

$$\log\left(\frac{dn(t)}{dt}\right) = \log\left(k_1 \cdot 10^{\log(n(t))} + k_2 \cdot 10^{2\cdot\log(n(t))} + k_3 \cdot 10^{3\cdot\log(n(t))}\right). \qquad 6.3$$

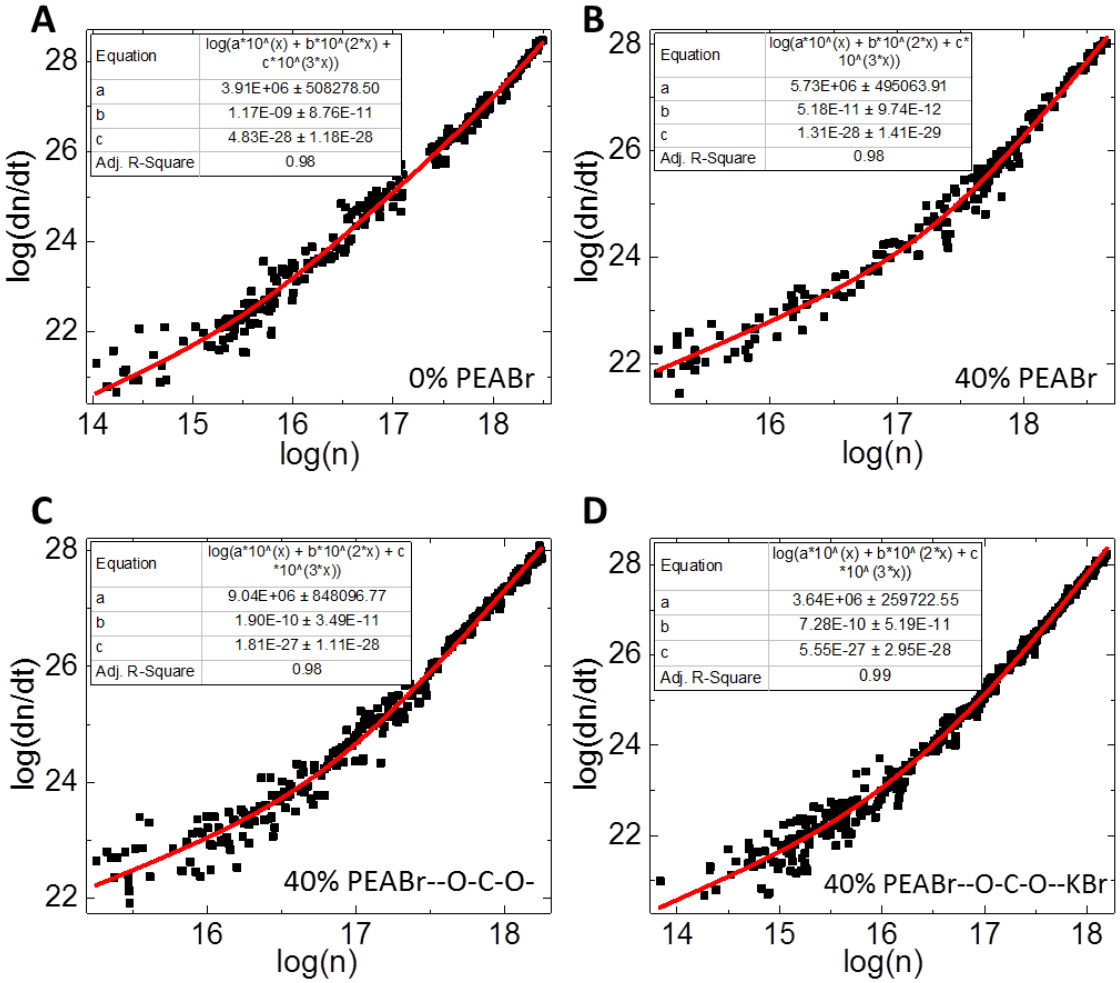

Figure 6.10 Fits of log(recombination rate) plotted against log(carrier density) for all additive-controlled perovskite samples. *The values of a, b and c correspond to the first, second and third-order recombination constants* $\boldsymbol{k_1}$, $\boldsymbol{k_2}$ *and* $\boldsymbol{k_3}$ *respectively for the (A) 0% PEABr, (B) 40% PEABr, (C) 40% PEABr--O-C-O- and (D) 40% PEABr--O-C-O--KBr additive-controlled perovskite samples.*

The recombination rate constants extracted from TA and TPL are shown in Table 6.3. The second-order recombination rate constants are an order of magnitude smaller in the

40% PEABr, 40% PEABr--O-C-O- and 40% PEABr--O-C-O--KBr samples than in the 0% PEABr sample. In fact, the 40% PEABr, 40% PEABr--O-C-O- and 40% PEABr--O-C-O--KBr samples may be approximated reasonably well with only first-order and third-order recombination rate constants, as shown in Figure 6.11. In agreement with the TPL measurements, this suggests that second-order recombination processes are less likely to occur in additive-controlled perovskites than in standard lead halide perovskites and is evidence that the charge carriers are localised in these materials[158]. The third-order recombination rate constants are also an order of magnitude larger in the 40% PEABr--O-C-O- and 40% PEABr--O-C-O--KBr samples than in the 0% PEABr and 40% PEABr samples. This is consistent with our prediction that charge carriers are more localised in smaller nanocrystalline regions in these materials, resulting in an enhanced interaction probability at high excitation densities and a faster Auger recombination rate[125].

Sample	k_1 (s^{-1})	k_2 ($cm^3\ s^{-1}$)	k_3 ($cm^6\ s^{-1}$)
0% PEABr	3.9×10^{6}	1.2×10^{-9}	4.8×10^{-28}
40% PEABr	5.7×10^{6}	5.2×10^{-11}	1.3×10^{-28}
40% PEABr--O-C-O-	9.0×10^{6}	1.9×10^{-10}	1.8×10^{-27}
40% PEABr--O-C-O--KBr	3.6×10^{6}	7.3×10^{-10}	5.6×10^{-27}

Table 6.3 Table of the first, second and third-order recombination rates extracted from TA and TPL measurements. *The second-order recombination rate constant is an order of magnitude smaller in the 40% PEABr, 40% PEABr--O-C-O- and 40% PEABr--O-C-O--KBr samples than in the 0% PEABr sample, indicating that second-order recombination is less dominating in these materials. The third-order recombination rate is also an order of magnitude larger in the 40% PEABr--O-C-O- and 40% PEABr--O-C-O--KBr samples than in the 0% PEABr and 40% PEABr samples, indicating that carriers are more localised and therefore more likely to interact with each other in these materials.*

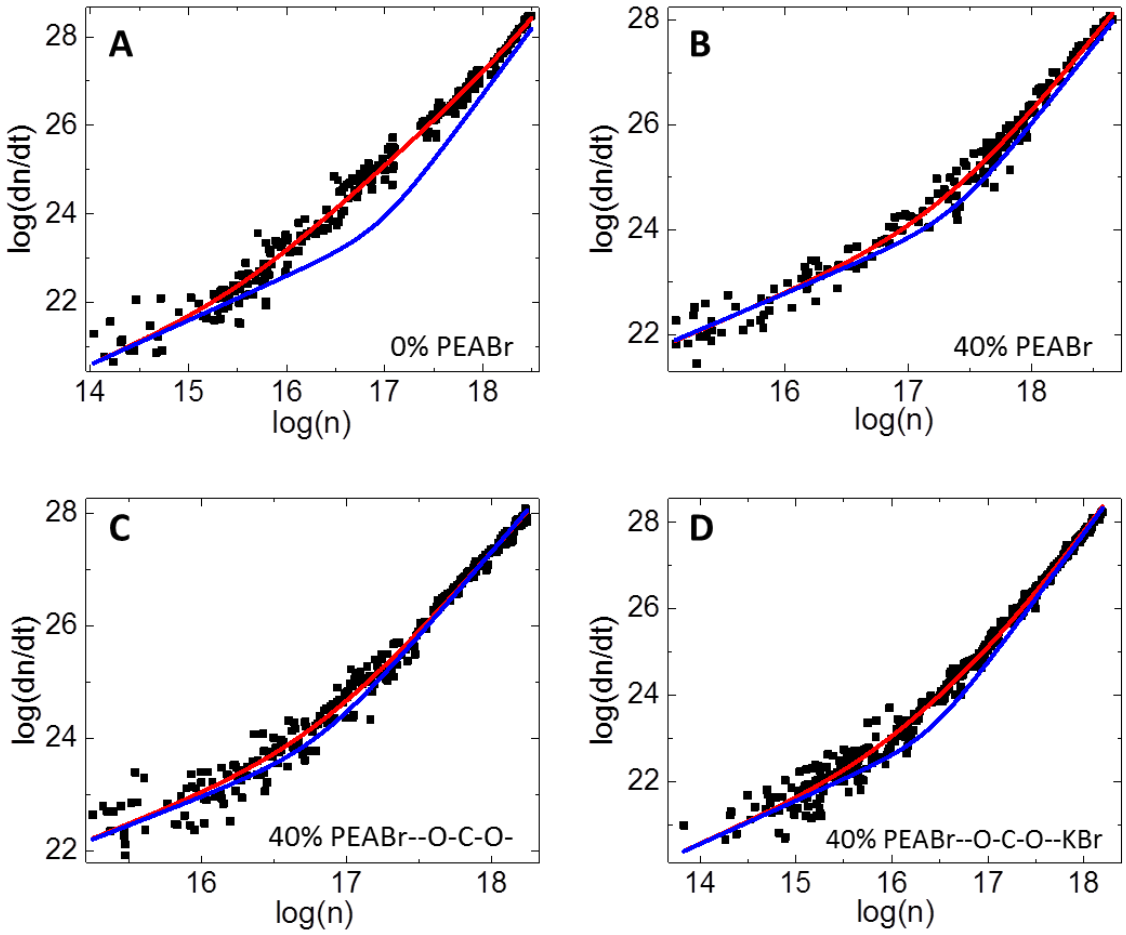

Figure 6.11 Fits of log(recombination rate) plotted against log(carrier density) for all additive-controlled perovskite samples. *The red lines are fits including the first, second and third-order recombination rate constants for the (A) 0% PEABr, (B) 40% PEABr, (C) 40% PEABr--O-C-O- and (D) 40% PEABr--O-C-O--KBr additive-controlled perovskite samples. The blue lines are the same fits with the second-order recombination rate constant set to zero.*

6.7 Scanning electron microscopy (SEM), atomic force microscopy (AFM) and grazing incidence x-ray diffraction (GIXRD) of additive-controlled perovskites

In order to confirm that the organic PEABr and -O-C-O- additives cause structural changes to the $CsPbBr_3$ perovskite, SEM, AFM and GIXRD was carried out by the group of Baoquan Sun, as shown in Figure 6.12. The SEM and AFM images show that the film morphology is significantly improved in the 40% PEABr and 40% PEABr--O-C-O- samples than in the 0% PEABr sample. These films have fewer holes and a lower surface roughness, due to the smaller grain sizes observed in these materials. This suggests that the large PEABr molecules impede perovskite crystal growth, consistent with previous reports in which long-chain ammonium halides were used to impede perovskite growth, reduce surface roughness and reduce the perovskite dimensionality from three-dimensional to two-dimensional[274].

The GIXRD measurements suggest that adding PEABr to the $CsPbBr_3$ perovskite causes the crystallites to preferentially align with the substrate. In the 0% PEABr GIXRD pattern, powder-like rings are observed, indicating that the crystallites have a preferred orientation in the 110 direction but are randomly aligned. Whereas in the 40% PEABr and 40% PEABr--O-C-O- GIXRD patterns, distinct peaks are observed. This is consistent with the formation of self-stacked two-dimensional nanoplatelets[74,278]. The XRD peaks are also broader in the 40% PEABr and 40% PEABr--O-C-O- samples. This suggests that the average size of the crystallites is smaller in these materials, as shown in Table 6.4, and is consistent with the reductions in crystallite size observed in the SEM and AFM images. An additional peak is observed in the 40% PEABr GIXRD pattern, arising from PEABr crystallisation. This peak is not observed in the 40% PEABr--O-C-O- GIXRD pattern, indicating that the addition of -O-C-O- suppresses PEABr crystallisation, further reducing the average perovskite crystallite size and further improving film morphology. The role of KBr is still being investigated.

Image removed for copyright reasons.

Figure 6.12 Structural characterisation of additive-controlled perovskites. *Grazing-incidence x-ray diffraction (GIXRD, left), scanning electron microscopy (SEM, middle) and atomic force microscopy (AFM, right) of (A) 0% PEABr, (B) 40% PEABr and (C) 40% PEABr--O-C-O-. An additional peak is observed in the 40% PEABr GIXRD pattern (red arrow), indicating PEABr crystallisation. The SEM images indicate that the 40% PEABr and 40% PEABr--O-C-O- film morphologies are of high quality and consist of small crystallites. The AFM images indicate that the root mean squared (r.m.s) roughness is significantly lower in the 40% PEABr and 40% PEABr--O-C-O- samples than in the 0% PEABr sample. The scale bars on the SEM images are all 200 nm. The scan areas of the AFM images are all 2 × 2 μm.*

Sample	Average grain size (nm)
0% PEABr	42.8
40% PEABr	18.5
40% PEABr--O-C-O-	13.3

Table 6.4 Table of the average grain size of the additive-controlled perovskite samples. *Average grain sizes were extracted from θ-2θ XRD using the Scherer equation. Measurements were carried out by the group of Baoquan Sun.*

6.8 Conclusions and future work

In this chapter, we have demonstrated highly efficient additive-controlled $CsPbBr_3$ perovskite LEDs, with EQEs of over 15%. We have shown that the origin of this excellent device performance is likely to be due to the increased carrier localisation observed in these materials. Using steady-state absorption and photoluminescence measurements, we have shown that the incorporation of phenethylamine bromide (PEABr) and a chemical additive with an electron-rich -O-C-O- chemical bond (-O-C-O-) into $CsPbBr_3$ perovskite lattice seems to modulate the dimensionality of the $CsPbBr_3$ perovskite lattice. This modulation appears to enable an efficient energy funnelling process to lower energy emissive states in the material, which outcompetes the non-radiative recombination processes that dominate recombination in typical three-dimensional perovskites. This is in agreement with TPL measurements, which indicate that radiative recombination is dominated by a second-order process in standard $CsPbBr_3$, but by a first-order process in $CsPbBr_3$ with PEABr and -O-C-O- additives. We demonstrated that the same behaviour is observed in standard $CsPbI_3$ nanocrystal films, suggesting that charge carrier localisation is occurring in the additive-controlled perovskite films. This is confirmed by TA measurements, which show that second-order recombination is suppressed and third-order recombination is enhanced in the materials containing PEABr and -O-C-O- molecules. This energy funnelling effect leads to an increase in the PLQE from <1% to 70% and is most likely the origin of the excellent device performance.

Further work will be done on these materials to investigate in more detail how different organic additives modify the crystal lattice and also to understand how the KBr further enhances the PLQE. Different organic additives might lead to even more efficient energy funnelling processes, resulting in even higher device efficiencies.

7 Conclusions and future work

In this thesis, we used transient photoluminescence and absorption spectroscopies to investigate the fundamental nature of charge carrier generation, relaxation and recombination in a range of lead halide perovskites. We studied the standard lead halide perovskites, as well as the lead halide perovskites used in the current record perovskite solar cells – with power conversion efficiencies of over 22% – and the current record perovskite light-emitting diodes – with external quantum efficiencies of over 15%. We found that the optical and electronic properties of lead halide perovskites can be readily tuned by modifying the lead halide lattice. The choice of A-site cation appears not to have any direct effect on the fundamental photophysical properties of these materials, but it can have a significant indirect influence if it modifies the lead halide lattice.

We have shown that lead halide perovskites have different photophysical properties to those observed in classical purely organic and inorganic semiconductors. The hybrid nature of the lead halide perovskite crystal lattice results in a dynamic and highly flexible material with easily modifiable optical and electronic properties. In particular, we have demonstrated that in the future it may be possible to enhance the general optoelectronic performance a range of standard lead halide perovskites by applying external strain, how incorporating mixed A-site cations into $CH_3NH_3PbI_3$ perovskites can improve solar cell performance and how using organic molecular additives in $CsPbI_3$ perovskites can improve light-emitting diode performance.

In Chapter 4, we investigated how the optoelectronic properties of lead halide perovskites differ from those observed in classical organic and inorganic semiconductors and considered the impact of the hybrid nature of these materials on device performance. Using linear polarisation selective transient absorption spectroscopy, we showed that lead halide perovskites exhibit a photo-induced anisotropy. This anisotropy lives for ~10 ps in iodide perovskites and ~1 ps in bromide perovskites, which is significantly longer than the typical carrier scattering times in these materials. Using first-principles calculations, we demonstrated that this anisotropy likely originates from dynamic deformations of the lead halide lattice. These deformations occur over length scales of ~10 nm and lead to local variations in the optical and electronic properties of lead halide perovskites. By stabilising and enhancing this effect, for example by applying external strain to the material, it may be possible to control the optoelectronic properties of these materials in devices and enhance device performance.

In Chapter 5, we investigated how the incorporation of mixed A-site cations into the lead halide perovskite lattice can also lead to significant improvements in solar cell performance. By combining transient photoluminescence and absorption spectroscopies we found that the first-order and second-order recombination rates were reduced by almost two orders of magnitude when a mixture of rubidium, caesium and formamidinium were used in the preparation of methylammonium lead halide perovskites. This suggests that the density of non-radiative first and second-order recombination pathways is reduced in these materials, most likely because of a reduction in the formation of deep-level defects. We also found that radiative recombination is always dominated by a second-order process and that the PLQEs increase as the first and second-order recombination rates decrease. Changes to the lattice volume measured with x-ray diffraction and Raman spectroscopy indicate that the observed increases in PLQE and reduction in defect density most likely arise from a reduction in lattice strain, which leads to enhanced solar cell performance and photo-stability in these materials.

In Chapter 6, we investigated how the incorporation of organic molecular additives into the lead halide perovskite lattice can also lead to significant improvements in light-emitting diode performance. By combining transient photoluminescence and absorption spectroscopies with scanning electron microscopy, atomic force microscopy and grazing

incidence x-ray diffraction, we showed that the addition of phenethylamine bromide and a chemical additive with an electron-rich -O-C-O- chemical bond can modulate the dimensionality of a caesium lead bromide perovskite lattice. As the dimensionality is modulated, the second-order recombination rate is reduced, the third-order recombination rate is increased, and radiative recombination changes from a dominantly second-order process to a dominantly first-order process without corresponding changes in the emission spectra. This suggests that the dimensionality modulation enables an efficient energy funnelling process to localised lower energy regions of the material where the carriers interact more frequently and radiatively recombine more effectively. These energy funnelling and carrier localisation effects seem to enhance the PLQE at low excitation densities and lead to enhanced light-emitting diode performance in these materials.

The work carried out in Chapters 4-6 has highlighted that the optoelectronic properties of lead halide perovskites are extremely sensitive to modifications in the lead halide lattice. These high levels of control suggest a future where different lead halide perovskite materials will be precisely manufactured for specific optoelectronic applications. There are a number of new potential molecular additives and treatments, which could be applied to lead halide perovskites to further improve performance. Such treatments could also be applied locally in order to locally modulate the perovskite crystal structure. The effect of these modulations on the optoelectronic properties of the material could then be locally probed with transient photoluminescence and absorption microscopy techniques. By combining the knowledge from such investigations, it is likely that we will be able to significantly improve the performance of lead halide perovskite solar cells and light-emitting diodes over the next few years.

LIST OF PUBLICATIONS

Jasmine P. H. Rivett, Tudor H. Thomas, Johannes M. Richter, Edward Booker, Tim Van De Goor, Siân E. Dutton, Dan Credgington, Michael Saliba, Felix Deschler "Recombination in mixed-cation lead-halide perovskites" *In preparation*

Jasmine P. H. Rivett, Liang Z. Tan, Michael B. Price, Nathaniel J. L. K. Davis, Roxanne Middleton, Andrew M. Rappe, Dan Credgington, Felix Deschler "Dynamic structural motions generate long-lived photo-excited polarization anisotropy in hybrid perovskites" *Submitted*

Muyang Ban‡, Yatao Zou‡, **Jasmine P. H. Rivett‡**, Yingguo Yang, Tudor H. Thomas, Yeshu Tan, Tao Song, Xinyu Gao, Dan Credgington, Felix Deschler, Henning Sirringhaus, Baoquan Sun "Solution-Processed Perovskite Light Emitting Diodes with Efficiency Exceeding 15% through Additive-Controlled Nanostructure Tailoring" *Submitted* (‡ These authors contributed equally to this work)

Jasmine P. H. Rivett, Johannes M. Richter, Michael B. Price, Dan Credgington, Felix Deschler "Carrier-phonon interactions in hybrid halide perovskites probed with ultrafast anisotropy studies" *SPIE Nanoscience + Engineering* **99231E-99231E-4** (2016)

Dawei Di, Alexander S. Romanov, Le Yang, Johannes M. Richter, **Jasmine P. H. Rivett**, Saul Jones, Tudor H. Thomas, Mojtaba Abdi Jalebi, Richard H. Friend, Mikko Linnolahti, Manfred Bochmann, Dan Credgington "High-performance light-emitting diodes based on carbene-metal-amides" *Science* **356**, 6334 (2017)

Johannes M. Richter, Mojtaba Abdi-Jalebi, Aditya Sadhanala, Maxim Tabachnyk, **Jasmine P. H. Rivett**, Luis M. Pazos-Outón, Karl C. Gödel, Michael Price, Felix Deschler, Richard H. Friend "Enhancing photoluminescence yields in lead halide perovskites by photon recycling and light out-coupling" *Nat. Commun*. **7**, 13941 (2016)

Marcus L. Böhm, Tom C. Jellicoe, **Jasmine P. H. Rivett**, Aditya Sadhanala, Nathaniel J. L. K. Davis, Frederik S. F. Morgenstern, Karl C. Gödel, Jayamurugan Govindasamy, Callum G. M. Benson, Neil C. Greenham, Bruno Ehrler "Size and Energy Level Tuning of Quantum Dot Solids via a Hybrid Ligand Complex" *J. Phys. Chem. Lett.* **6**, 17 (2015)

REFERENCES

1. Sargent, E. H. Colloidal quantum dot solar cells. *Nat. Photonics* **6,** 133–135 (2012).
2. Dreyfus, G. & Gallinat, C. Rise and Shine: Lighting the World with 10 Billion LED Bulbs. *U.S. Dep. Energy* (2015). at <https://www.energy.gov/articles/rise-and-shine-lighting-world-10-billion-led-bulbs>
3. Schmidt-Mende, L. & Weickert, J. *Organic and Hybrid Solar Cells, An Introduction*. (Walter de Gruyter GmbH, 2016).
4. Round, H. J. A Note on Carborundum. *Electr. World* **49,** (1907).
5. Kojima, A., Teshima, K., Shirai, Y. & Miyasaka, T. Organometal Halide Perovskites as Visible-Light Sensitizers for Photovoltaic Cells. *J. Am. Chem. Soc.* **131,** 6050–6051 (2009).
6. Yang, W. S. *et al.* Iodide management in formamidinium-lead-halide–based perovskite layers for efficient solar cells. *Science.* **356,** 1376–1379 (2017).
7. Tan, Z.-K. *et al.* Bright light-emitting diodes based on organometal halide perovskite. *Nat. Nanotechnol.* **9,** 687–692 (2014).
8. Ban, M., Zou, Y., Rivett, J. & Yang, Y. Solution-Processed Perovskite Light Emiting Diodes with Efficiency Exceeding 15% through Additive-Controlled Nanostructure Tailoring. *Submitted* (2017).
9. Deschler, F. *et al.* High Photoluminescence Efficiency and Optically Pumped Lasing in Solution-Processed Mixed Halide Perovskite Semiconductors. *J. Phys. Chem. Lett.* **5,** 1421–1426 (2014).
10. Zhu, H. *et al.* Lead halide perovskite nanowire lasers with low lasing thresholds and high quality factors. *Nat. Mater.* **14,** 636–642 (2015).
11. Sutherland, B. R. & Sargent, E. H. Perovskite photonic sources. *Nat. Photonics* **10,** 295–302 (2016).
12. Veldhuis, S. A. *et al.* Perovskite Materials for Light-Emitting Diodes and Lasers. *Adv. Mater.* **28,** 6804–6834 (2016).
13. Mitzi, D. B., Chondroudis, K. & Kagan, C. R. Organic-inorganic electronics.

IBM J. Res. Dev. **45,** 29–45 (2001).

14. Luo, J. *et al.* Water photolysis at 12.3% efficiency via perovskite photovoltaics and Earth-abundant catalysts. *Science.* **345,** (2014).

15. Dou, L. *et al.* Solution-processed hybrid perovskite photodetectors with high detectivity. *Nat. Commun.* **5,** (2014).

16. Xu, X. *et al.* High-Performance Near-IR Photodetector Using Low-Bandgap MA0.5FA0.5Pb0.5Sn0.5I3 Perovskite. *Adv. Funct. Mater.* **27,** 1701053 (2017).

17. Oxford Photovoltaics. Oxford Photovoltaics Homepage. (2105). at <https://www.oxfordpv.com/>

18. Goldschmidt, V. M. Die Gesetze der Krystallochemie. *Naturwissenschaften* **14,** 477–485 (1926).

19. Jin, H., Rhim, S. H., Im, J. & Freeman, A. J. Topological Oxide Insulator in Cubic Perovskite Structure. *Sci. Rep.* **3,** (2013).

20. Smolin, S. Y., Scafetta, M. D., Guglietta, G. W., Baxter, J. B. & May, S. J. Ultrafast transient reflectance of epitaxial semiconducting perovskite thin films. *Appl. Phys. Lett.* **105,** 022103 (2014).

21. Hayashi, S., Aoki, R. & Nakamura, T. Metallic conductivity in perovskite-type compounds AMoO3 (A = Ba, Sr, Ca) down to 2.5K. *Mater. Res. Bull.* **14,** 409–413 (1979).

22. Peña, M. A. & Fierro, J. L. G. Chemical structures and performance of perovskite oxides. *Chem. Rev.* **101,** 1981–2017 (2001).

23. Wells, H. L. Über die Cäsium- und Kalium-Bleihalogenide. *Z. Anorg. Allg. Chem.* **3,** 195 (1893).

24. Zhao, Y. *et al.* Organic–inorganic hybrid lead halide perovskites for optoelectronic and electronic applications. *Chem. Soc. Rev.* **45,** 655–689 (2016).

25. Stranks, S. D. & Snaith, H. J. Metal-halide perovskites for photovoltaic and light-emitting devices. *Nat. Nanotechnol.* **10,** 391–402 (2015).

26. De Wolf, S. *et al.* Organometallic Halide Perovskites: Sharp Optical Absorption Edge and Its Relation to Photovoltaic Performance. *J. Phys. Chem. Lett.* **5,** 1035–1039 (2014).

27. Park, N. G., Grätzel, M. & Miyasaka, T. *Organic-inorganic halide perovskite photovoltaics: From fundamentals to device architectures*. (2016).

28. Knox, R. S. *Theory of excitons*. (Academic Press, 1963). at <http://www.worldcat.org/title/theory-of-excitons/oclc/330436>

29. Reynolds, D. C. & Collins, T. C. *Excitons, their properties and uses*. (Academic Press, 1981).

30. Miyata, A. *et al.* Direct measurement of the exciton binding energy and effective masses for charge carriers in organic–inorganic tri-halide perovskites. *Nat. Phys.* **11,** 582–587 (2015).

31. Galkowski, K. *et al.* Determination of the exciton binding energy and effective masses for methylammonium and formamidinium lead tri-halide perovskite semiconductors. *Energy Environ. Sci.* **9,** 962–970 (2016).

32. Wehrenfennig, C., Eperon, G. E., Johnston, M. B., Snaith, H. J. & Herz, L. M. High Charge Carrier Mobilities and Lifetimes in Organolead Trihalide Perovskites. *Adv. Mater.* **26,** 1584–1589 (2014).

33. Stranks, S. D. *et al.* Electron-Hole Diffusion Lengths Exceeding 1 Micrometer in an Organometal Trihalide Perovskite Absorber. *Science.* **342,** (2013).

34. Xing, G. *et al.* Long-Range Balanced Electron- and Hole-Transport Lengths in Organic-Inorganic CH3NH3PbI3. *Science.* **342,** (2013).

35. Pazos-Outón, L. M., Szumilo, M., Lamboll, R. & Richter, J. Photon recycling in lead iodide perovskite solar cells. *Science.* **351,** 1430–1434 (2016).

36. Strelcov, E. *et al.* CH3NH3PbI3 perovskites: Ferroelasticity revealed. *Sci. Adv.* **3,** e1602165 (2017).

37. Zhou, Y. *et al.* Giant photostriction in organic–inorganic lead halide perovskites. *Nat. Commun.* **7,** 11193 (2016).

38. Ding, R. *et al.* High-performance piezoelectric nanogenerators composed of formamidinium lead halide perovskite nanoparticles and poly(vinylidene fluoride). *Nano Energy* **37,** 126–135 (2017).

39. Röhm, H., Leonhard, T., Hoffmann, M. J. & Colsmann, A. Ferroelectric domains in methylammonium lead iodide perovskite thin-films. *Energy Environ. Sci.* **10,**

950–955 (2017).

40. Sajedi Alvar, M., Kumar, M., Blom, P. W. M., Wetzelaer, G.-J. A. H. & Asadi, K. Absence of ferroelectricity in methylammonium lead iodide perovskite. *AIP Adv.* **7,** 095110 (2017).

41. Fan, Z. *et al.* Ferroelectricity of CH3NH3PbI3 perovskite. *J. Phys. Chem. Lett.* **6,** 1155–1161 (2015).

42. Yaffe, O. *et al.* Local Polar Fluctuations in Lead Halide Perovskite Crystals. *Phys. Rev. Lett.* **118,** 136001 (2017).

43. Leguy, A. M. A. *et al.* Dynamic disorder, phonon lifetimes, and the assignment of modes to the vibrational spectra of methylammonium lead halide perovskites. *Phys. Chem. Chem. Phys.* **18,** 27051–27066 (2016).

44. Beecher, A. N. *et al.* Direct Observation of Dynamic Symmetry Breaking above Room Temperature in Methylammonium Lead Iodide Perovskite. *ACS Energy Lett.* **1,** 880–887 (2016).

45. Chen, T. *et al.* Rotational dynamics of organic cations in the CH3NH3PbI3 perovskite. *Phys. Chem. Chem. Phys.* **17,** 31278–31286 (2015).

46. Bakulin, A. A. *et al.* Real-Time Observation of Organic Cation Reorientation in Methylammonium Lead Iodide Perovskites. *J. Phys. Chem. Lett.* **6,** 3663–3669 (2015).

47. Selig, O. *et al.* Organic Cation Rotation and Immobilization in Pure and Mixed Methylammonium Lead-Halide Perovskites. *J. Am. Chem. Soc.* **139,** 4068–4074 (2017).

48. Etienne, T., Mosconi, E. & De Angelis, F. Dynamical Origin of the Rashba Effect in Organohalide Lead Perovskites: A Key to Suppressed Carrier Recombination in Perovskite Solar Cells? *J. Phys. Chem. Lett.* **7,** 1638–1645 (2016).

49. Leppert, L., Reyes-Lillo, S. E. & Neaton, J. B. Electric Field- and Strain-Induced Rashba Effect in Hybrid Halide Perovskites. *J. Phys. Chem. Lett.* **7,** 3683–3689 (2016).

50. Niesner, D. *et al.* Giant Rashba Splitting in $CH_3NH_3PbBr_3$ Organic-Inorganic

Perovskite. *Phys. Rev. Lett.* **117,** 126401 (2016).

51. Yu, Z.-G. Rashba Effect and Carrier Mobility in Hybrid Organic–Inorganic Perovskites. *J. Phys. Chem. Lett.* **7,** 3078–3083 (2016).

52. Even, J., Pedesseau, L., Jancu, J. M. & Katan, C. Importance of spin-orbit coupling in hybrid organic/inorganic perovskites for photovoltaic applications. *J. Phys. Chem. Lett.* **4,** 2999–3005 (2013).

53. Zheng, F., Tan, L. Z., Liu, S. & Rappe, A. M. Rashba spin-orbit coupling enhanced carrier lifetime in CH3NH3PbI3. *Nano Lett.* **15,** 7794–7800 (2015).

54. Noh, J. H., Im, S. H., Heo, J. H., Mandal, T. N. & Seok, S. Il. Chemical Management for Colorful, Efficient, and Stable Inorganic–Organic Hybrid Nanostructured Solar Cells. *Nano Lett.* **13,** 1764–1769 (2013).

55. Eperon, G. E. *et al.* Formamidinium lead trihalide: a broadly tunable perovskite for efficient planar heterojunction solar cells. *Energy Environ. Sci.* **7,** 982 (2014).

56. Amat, A. *et al.* Cation-induced band-gap tuning in organohalide perovskites: Interplay of spin-orbit coupling and octahedra tilting. *Nano Lett.* **14,** 3608–3616 (2014).

57. Li, Z. *et al.* Stabilizing Perovskite Structures by Tuning Tolerance Factor: Formation of Formamidinium and Cesium Lead Iodide Solid-State Alloys. *Chem. Mater.* **28,** 284–292 (2016).

58. Yi, C. *et al.* Entropic stabilization of mixed A-cation ABX 3 metal halide perovskites for high performance perovskite solar cells. *Energy Environ. Sci.* **9,** 656–662 (2016).

59. Saliba, M. *et al.* Incorporation of rubidium cations into perovskite solar cells improves photovoltaic performance. *Science.* **354,** 206–209 (2016).

60. Choi, H. *et al.* Cesium-doped methylammonium lead iodide perovskite light absorber for hybrid solar cells. *Nano Energy* **7,** 80–85 (2014).

61. Lee, J. W. *et al.* Formamidinium and cesium hybridization for photo- and moisture-stable perovskite solar cell. *Adv. Energy Mater.* **5,** 1501310 (2015).

62. Saliba, M. *et al.* Cesium-containing triple cation perovskite solar cells: improved stability, reproducibility and high efficiency. *Energy Environ. Sci.* **9,** 1989–1997

(2016).

63. Jeon, N. J. *et al.* Compositional engineering of perovskite materials for high-performance solar cells. *Nature* **517,** 476–480 (2015).

64. Saliba, M. *et al.* A molecularly engineered hole-transporting material for efficient perovskite solar cells. *Nat. Energy* **1,** 15017 (2016).

65. Li, X. *et al.* A vacuum flash-assisted solution process for high-efficiency large-area perovskite solar cells. *Science.* **353,** 58–62 (2016).

66. Stoumpos, C. C. *et al.* Ruddlesden-Popper Hybrid Lead Iodide Perovskite 2D Homologous Semiconductors. *Chem. Mater.* **28,** 2852–2867 (2016).

67. Blancon, J.-C. *et al.* Strongly bound excitons in Ruddlesden-Popper 2D perovskites. *arXiv* **1710.07653,** (2017).

68. Yu, Y., Zhang, D. & Yang, P. Ruddlesden-Popper Phase in Two-Dimensional Inorganic Halide Perovskites: A Plausible Model and the Supporting Observations. *Nano Lett.* **17,** 5489–5494 (2017).

69. Tsai, H. *et al.* High-efficiency two-dimensional Ruddlesden–Popper perovskite solar cells. *Nature* **536,** 312–316 (2016).

70. Stoumpos, C. C. *et al.* High Members of the 2D Ruddlesden-Popper Halide Perovskites: Synthesis, Optical Properties, and Solar Cells of (CH3(CH2)3NH3)2(CH3NH3)4Pb5I16. *Chem* **2,** 427–440 (2017).

71. Zhang, T. *et al.* Bication lead iodide 2D perovskite component to stabilize inorganic α-CsPbI 3 perovskite phase for high-efficiency solar cells. *Sci. Adv.* **3,** e1700841 (2017).

72. Zhou, J., Chu, Y. & Huang, J. Photodetectors Based on Two-Dimensional Layer-Structured Hybrid Lead Iodide Perovskite Semiconductors. *ACS Appl. Mater. Interfaces* **8,** 25660–25666 (2016).

73. Chen, Y. *et al.* 2D Ruddlesden-Popper Perovskites for Optoelectronics. *Adv. Mater.* 1703487 (2017). doi:10.1002/adma.201703487

74. Yuan, M. *et al.* Perovskite energy funnels for efficient light-emitting diodes. *Nat. Nanotechnol.* **11,** 872–877 (2016).

75. Quan, L. N. *et al.* Tailoring the Energy Landscape in Quasi-2D Halide

Perovskites Enables Efficient Green-Light Emission. *Nano Lett.* **17,** 3701–3709 (2017).

76. Wang, N. *et al.* Perovskite light-emitting diodes based on solution-processed self-organized multiple quantum wells. *Nat. Photonics* **10,** 699–704 (2016).

77. Chen, Z. *et al.* High-Performance Color-Tunable Perovskite Light Emitting Devices through Structural Modulation from Bulk to Layered Film. *Adv. Mater.* **29,** 1603157 (2017).

78. Kaltzoglou, A. *et al.* Trimethylsulfonium Lead Triiodide: An Air-Stable Hybrid Halide Perovskite. *Inorg. Chem.* **56,** 6302–6309 (2017).

79. Sun, S. *et al.* Synthesis, crystal structure, and properties of a perovskite-related bismuth phase, (NH4)3Bi2I9. *APL Mater.* **4,** 031101 (2016).

80. Qian, J., Guo, Q., Liu, L., Xu, B. & Tian, W. A theoretical study of hybrid lead iodide perovskite homologous semiconductors with 0D, 1D, 2D and 3D structures. *J. Mater. Chem. A* **5,** 16786–16795 (2017).

81. Weidman, M. C., Seitz, M., Stranks, S. D. & Tisdale, W. A. Highly Tunable Colloidal Perovskite Nanoplatelets through Variable Cation, Metal, and Halide Composition. *ACS Nano* **10,** 7830–7839 (2016).

82. Li, J. *et al.* 2D Behaviors of Excitons in Cesium Lead Halide Perovskite Nanoplatelets. *J. Phys. Chem. Lett.* **8,** 1161–1168 (2017).

83. Weidman, M. C., Goodman, A. J. & Tisdale, W. A. Colloidal Halide Perovskite Nanoplatelets: An Exciting New Class of Semiconductor Nanomaterials. *Chem. Mater.* **29,** 5019–5030 (2017).

84. Lim, D.-H., Ramasamy, P., Kwak, D.-H. & Lee, J.-S. Solution-phase synthesis of rubidium lead iodide orthorhombic perovskite nanowires. *Nanotechnology* **28,** 255601 (2017).

85. Zhang, D. *et al.* Ultrathin Colloidal Cesium Lead Halide Perovskite Nanowires. *J. Am. Chem. Soc.* **138,** 13155–13158 (2016).

86. Waleed, A. *et al.* All inorganic cesium lead iodide perovskite nanowires with stabilized cubic phase at room temperature and nanowire array-based photodetectors. *Nano Lett.* **17,** 4951–4957 (2017).

87. Fu, P. *et al.* Perovskite nanocrystals: synthesis, properties and applications. *Sci. Bull.* **62,** 369–380 (2017).

88. Kovalenko, M. V. & Bodnarchuk, M. I. Lead Halide Perovskite Nanocrystals: From Discovery to Self-assembly and Applications. *Chim. Int. J. Chem.* **71,** 461–470 (2017).

89. Gomez, L., de Weerd, C., Hueso, J. L. & Gregorkiewicz, T. Color-stable water-dispersed cesium lead halide perovskite nanocrystals. *Nanoscale* **9,** 631–636 (2017).

90. Woo, J. Y. *et al.* Highly Stable Cesium Lead Halide Perovskite Nanocrystals through in Situ Lead Halide Inorganic Passivation. *Chem. Mater.* **29,** 7088–7092 (2017).

91. Protesescu, L. *et al.* Nanocrystals of Cesium Lead Halide Perovskites ($CsPbX_3$, X = Cl, Br, and I): Novel Optoelectronic Materials Showing Bright Emission with Wide Color Gamut. *Nano Lett.* **15,** 3692–3696 (2015).

92. European Parliament. Directive 2002/95/EC of the European Parliament and of the Council of 27 January 2003 on the restriction of the use of certain hazardous substances in electrical and electronic equipment. *Off. J. Eur. Union* **46,** (2003).

93. Binek, A. *et al.* Recycling Perovskite Solar Cells To Avoid Lead Waste. *ACS Appl. Mater. Interfaces* **8,** 12881–12886 (2016).

94. Hoefler, S. F., Trimmel, G. & Rath, T. Progress on lead-free metal halide perovskites for photovoltaic applications: a review. *Monatshefte für Chemie - Chem. Mon.* **148,** 795–826 (2017).

95. Konstantakou, M. & Stergiopoulos, T. A critical review on tin halide perovskite solar cells. *J. Mater. Chem. A* **5,** 11518–11549 (2017).

96. Toshniwal, A. & Kheraj, V. Development of organic-inorganic tin halide perovskites: A review. *Sol. Energy* **149,** 54–59 (2017).

97. Stoumpos, C. C., Malliakas, C. D. & Kanatzidis, M. G. Semiconducting Tin and Lead Iodide Perovskites with Organic Cations: Phase Transitions, High Mobilities, and Near-Infrared Photoluminescent Properties. *Inorg. Chem.* **52,** 9019–9038 (2013).

98. Stoumpos, C. C., Mao, L., Malliakas, C. D. & Kanatzidis, M. G. Structure–Band Gap Relationships in Hexagonal Polytypes and Low-Dimensional Structures of Hybrid Tin Iodide Perovskites. *Inorg. Chem.* **56,** 56–73 (2017).

99. Noel, N. K. *et al.* Lead-free organic–inorganic tin halide perovskites for photovoltaic applications. *Energy Environ. Sci.* **7,** 3061–3068 (2014).

100. Liao, W. *et al.* Lead-Free Inverted Planar Formamidinium Tin Triiodide Perovskite Solar Cells Achieving Power Conversion Efficiencies up to 6.22%. *Adv. Mater.* **28,** 9333–9340 (2016).

101. Pering, S. R. *et al.* Azetidinium lead iodide for perovskite solar cells. *J. Mater. Chem. A* **5,** 20658–20665 (2017).

102. Shockley, W. & Queisser, H. J. Detailed balance limit of efficiency of p-n junction solar cells. *J. Appl. Phys.* **32,** 510–519 (1961).

103. Kontos, A. G. *et al.* Structural Stability, Vibrational Properties, and Photoluminescence in CsSnI3 Perovskite upon the Addition of SnF2. *Inorg. Chem.* **56,** 84–91 (2017).

104. Anaya, M. *et al.* Optical analysis of CH3NH3SnxPb1−xI3 absorbers: a roadmap for perovskite-on-perovskite tandem solar cells. *J. Mater. Chem. A* **4,** 11214–11221 (2016).

105. Shao, S. *et al.* Highly Reproducible Sn-Based Hybrid Perovskite Solar Cells with 9% Efficiency. *Adv. Energy Mater.* **8,** 1702019 (2018).

106. Leijtens, T., Prasanna, R., Gold-Parker, A., Toney, M. F. & McGehee, M. D. Mechanism of Tin Oxidation and Stabilization by Lead Substitution in Tin Halide Perovskites. *ACS Energy Lett.* **Just Accep,** (2017).

107. Hao, F. *et al.* Solvent-Mediated Crystallization of CH3NH3SnI3 Films for Heterojunction Depleted Perovskite Solar Cells. *J. Am. Chem. Soc.* **137,** 11445–11452 (2015).

108. Shum, K. & Tsatskina, A. Stabilizing tin-based perovskites. *Nat. Publ. Gr.* **1,** 1–2 (2016).

109. Lee, S. J. *et al.* Fabrication of Efficient Formamidinium Tin Iodide Perovskite Solar Cells through SnF2-Pyrazine Complex. *J. Am. Chem. Soc.* **138,** 3974–3977

(2016).

110. Liao, Y. *et al.* Highly Oriented Low-Dimensional Tin Halide Perovskites with Enhanced Stability and Photovoltaic Performance. *J. Am. Chem. Soc.* **139,** 6693–6699 (2017).

111. Lanzetta, L., Marin-Beloqui, J. M., Sanchez-Molina, I., Ding, D. & Haque, S. A. Two-Dimensional Organic Tin Halide Perovskites with Tunable Visible Emission and Their Use in Light-Emitting Devices. *ACS Energy Lett.* **2,** 1662–1668 (2017).

112. Babayigit, A. *et al.* Assessing the toxicity of Pb-and Sn-based perovskite solar cells in model organism Danio rerio. *Sci. Rep.* **6,** (2016).

113. Benmessaoud, I. R. *et al.* Health hazards of methylammonium lead iodide based perovskites: cytotoxicity studies. *Toxicol. Res.* **5,** 407–419 (2016).

114. Tsui, K. Y., Onishi, N. & Berger, R. F. Tolerance Factors Revisited: Geometrically Designing the Ideal Environment for Perovskite Dopants. *J. Phys. Chem. C* **120,** 23293–23298 (2016).

115. Hoye, R. L. Z. *et al.* Strongly Enhanced Photovoltaic Performance and Defect Physics of Air-Stable Bismuth Oxyiodide (BiOI). *Adv. Mater.* **29,** 1702176 (2017).

116. Pazoki, M. *et al.* Bismuth Iodide Perovskite Materials for Solar Cell Applications: Electronic Structure, Optical Transitions, and Directional Charge Transport. *J. Phys. Chem. C* **120,** 29039–29046 (2016).

117. Yang, B. *et al.* Lead-Free, Air-Stable All-Inorganic Cesium Bismuth Halide Perovskite Nanocrystals. *Angew. Chemie - Int. Ed.* **56,** 12471–12475 (2017).

118. Park, B. W. *et al.* Bismuth Based Hybrid Perovskites A3Bi2I9 (A: Methylammonium or Cesium) for Solar Cell Application. *Adv. Mater.* **27,** 6806–6813 (2015).

119. Kieslich, G., Sun, S. & Cheetham, A. K. An extended Tolerance Factor approach for organic–inorganic perovskites. *Chem. Sci.* **6,** 3430–3433 (2015).

120. Oxford English Dictionary. Semiconductor. *Oxford Univ. Press* (2017). at <https://en.oxforddictionaries.com/definition/semiconductor>

121. Yu, P. & Cardona, M. *Fundamentals of Semiconductors Physics and Materials Properties*. (Springer-Verlag, 2010).

122. Kittel, C. *Introduction to Solid State Physics*. (John Wiley & Sons, 1996).

123. Fox, M. *Optical Properties of Solids*. (Oxford University Press, 2010).

124. Chirvony, V. S. *et al.* Delayed Luminescence in Lead Halide Perovskite Nanocrystals. *J. Phys. Chem. C* **121,** 13381–13390 (2017).

125. Yang, Y. *et al.* Comparison of Recombination Dynamics in CH3NH3PbBr3 and CH3NH3PbI3 Perovskite Films: Influence of Exciton Binding Energy. *J. Phys. Chem. Lett.* **6,** 4688–4692 (2015).

126. Hutter, E. M. *et al.* Direct–indirect character of the bandgap in methylammonium lead iodide perovskite. *Nat. Mater.* **16,** 115–120 (2016).

127. Loudon, R. *The quantum theory of light*. (Oxford University Press, 2000).

128. Mandel, L. & Wolf, E. *Optical coherence and quantum optics*. (Cambridge University Press, 1995).

129. Fox, M. (Anthony M. *Quantum optics : an introduction*. (Oxford University Press, 2006).

130. Shah, J. *Ultrafast Spectroscopy of Semiconductors and Semiconductor Nanostructures*. (Springer-Verlag, 1999).

131. Oudar, J. L., Hulin, D., Migus, A., Antonetti, A. & Alexandre, F. Subpicosecond Spectral Hole Burning Due to Nonthermalized Photoexcited Carriers in GaAs. *Phys. Rev. Lett.* **55,** 2074–2077 (1985).

132. Hunsche, S., Heesel, H., Ewertz, A., Kurz, H. & Collet, J. H. Spectral-hole burning and carrier thermalization in GaAs at room temperature. *Phys. Rev. B* **48,** 17 818 – 17 826 (1993).

133. Elsaesser, T., Shah, J. & Lugli, P. Initial Thermalization of Photoexcited Carriers in GaAs Studied by Femtosecond Luminescence Spectroscopy. *Phys. Rev. Lett.* **66,** 1757 – 1760 (1991).

134. Sen, D. The uncertainty relations in quantum mechanics. *Curr. Sci.* **107,** 203–218 (2014).

135. Richter, J. M. *et al.* Ultrafast carrier thermalization in lead iodide perovskite

probed with two-dimensional electronic spectroscopy. *Nat. Commun.* **8,** 376 (2017).

136. Alfano, R. . *Semiconductors Probed by Ultrafast Laser Spectroscopy Volume I*. (Elsevier Science, 1984).

137. Price, M. B. *et al.* Hot-carrier cooling and photoinduced refractive index changes in organic–inorganic lead halide perovskites. *Nat. Commun.* **6,** (2015).

138. Chen, K., Barker, A. J., Morgan, F. L. C., Halpert, J. E. & Hodgkiss, J. M. Effect of carrier thermalization dynamics on light emission and amplification in organometal halide perovskites. *J. Phys. Chem. Lett.* **6,** 153–158 (2015).

139. Wright, A. D. *et al.* Electron–phonon coupling in hybrid lead halide perovskites. *Nat. Commun.* **7,** (2016).

140. Sendner, M. *et al.* Optical phonons in methylammonium lead halide perovskites and implications for charge transport. *Mater. Horiz* **3,** 613–620 (2016).

141. Yang, Y. *et al.* Observation of a hot-phonon bottleneck in lead-iodide perovskites. *Nat. Photonics* **10,** 53–59 (2015).

142. Rosenwaks, Y. *et al.* Hot-carrier cooling in GaAs: Quantum wells versus bulk. *Phys. Rev. B* **48,** 14675–14678 (1993).

143. Shah, J. Photoexcited hot carriers: From cw to 6 fs in 20 years. *Solid State Electron.* **32,** 1051–1056 (1989).

144. Zemskii, V. I., Zakharchenya, B. P. & Mirlin, D. . Polarization of hot photoluminescence in semiconductors of the GaAs type. *Zh. Eksp. Teor. Fiz.* **24,** 96–99 (1976).

145. Mirlin, D. N. & Reshina, I. . Anisotropy of the polarization of hot photoluminescence in gallium arsenide crystals. *Zh. Eksp. Teor. Fiz.* **73,** 859–864 (1977).

146. Varshni, Y. P. Band to Band Radiative Recombination in Groups IV, VI, and III V Semiconductors (I). *Phys. status solidi* **19,** 459–514 (1967).

147. Herz, L. M. Charge-Carrier Dynamics in Organic-Inorganic Metal Halide Perovskites. *Annu. Rev. Phys. Chem.* **67,** 65–89 (2016).

148. Shockley, W. & Read, W. T. Statistics of the Recombinations of Holes and

Electrons. *Phys. Rev.* **87,** 835–842 (1952).

149. Nelson, J. *The physics of solar cells*. (Imperial College Press, 2003).

150. Van Zeghbroeck, B. *Principles of Semiconductor Devices*. (University of Colorado, 2007).

151. Milot, R. L., Eperon, G. E., Snaith, H. J., Johnston, M. B. & Herz, L. M. Temperature-Dependent Charge-Carrier Dynamics in CH3NH3PbI3 Perovskite Thin Films. *Adv. Funct. Mater.* **25,** 6218–6227 (2015).

152. Richter, J. M. J. M. *et al.* Enhancing photoluminescence yields in lead halide perovskites by photon recycling and light out-coupling. *Nat. Commun.* **7,** 13941 (2016).

153. Johnston, M. B. & Herz, L. M. Hybrid Perovskites for Photovoltaics: Charge-Carrier Recombination, Diffusion, and Radiative Efficiencies. *Acc. Chem. Res.* **49,** 146–154 (2016).

154. Grundmann, M. *The Physics of Semiconductors*. (Springer International Publishing AG Switzerland, 2016).

155. Yakunin, S. *et al.* Low-threshold amplified spontaneous emission and lasing from colloidal nanocrystals of caesium lead halide perovskites. *Nat. Commun.* **6,** 8056 (2015).

156. Fang, H. H. *et al.* Exciton Recombination in Formamidinium Lead Triiodide: Nanocrystals versus Thin Films. *Small* **13,** 1700673 (2017).

157. Jellicoe, T. C. *et al.* Synthesis and Optical Properties of Lead-Free Cesium Tin Halide Perovskite Nanocrystals. *J. Am. Chem. Soc.* **138,** 2941–2944 (2016).

158. Wang, L. *et al.* Scalable Ligand-Mediated Transport Synthesis of Organic-Inorganic Hybrid Perovskite Nanocrystals with Resolved Electronic Structure and Ultrafast Dynamics. *ACS Nano* **11,** 2689–2696 (2017).

159. Hu, F. *et al.* Slow Auger Recombination of Charged Excitons in Nonblinking Perovskite Nanocrystals without Spectral Diffusion. *Nano Lett.* **16,** 6425–6430 (2016).

160. Manser, J. S. & Kamat, P. V. Band filling with free charge carriers in organometal halide perovskites. *Nat. Photonics* **8,** 737–743 (2014).

161. Lieten, R. R. *et al.* Photoluminescence of bulk germanium. *Phys. Rev. B - Condens. Matter Mater. Phys.* **86,** 035204 (2012).

162. Sum, T. C. *et al.* Spectral Features and Charge Dynamics of Lead Halide Perovskites: Origins and Interpretations. *Acc. Chem. Res.* **49,** 294–302 (2016).

163. Li, M. *et al.* Slow cooling and highly efficient extraction of hot carriers in colloidal perovskite nanocrystals. *Nat. Commun.* **8,** 14350 (2017).

164. de Mello, J. C., Wittmann, H. F. & Friend, R. H. An improved experimental determination of external photoluminescence quantum efficiency. *Adv. Mater.* **9,** 230–232 (1997).

165. Miller, O. D., Yablonovitch, E. & Kurtz, S. R. Strong internal and external luminescence as solar cells approach the Shockley-Queisser limit. *IEEE J. Photovoltaics* **2,** 303–311 (2012).

166. Fujiwara, H. & Wiley InterScience (Online service). *Spectroscopic ellipsometry : principles and applications*. (John Wiley & Sons, 2007).

167. Knowles, K. M. Herapathite - The first man-made polarizer. *Philos. Mag. Lett.* **89,** 745–755 (2009).

168. Jamali, M. *et al.* Photoresponsive transparent conductive metal with a photobleaching nose. *Adv. Mater.* **23,** 4243–4247 (2011).

169. Hagler, T. W., Pakbaz, K., Voss, K. F. & Heeger, A. J. Enhanced order and electronic delocalization in conjugated polymers oriented by gel processing in polyethylene. *Phys. Rev. B* **44,** 8652–8666 (1991).

170. Wendroff, J. H. *et al.* Polarized photoluminescence of liquid crystalline polymers with isolated arylenevinylene segments in the main chain. *Adv. Mater.* **7,** 923–925 (1995).

171. Grell, M. & Bradley, D. D. C. Polarized luminescence from oriented molecular materials. *Adv. Mater.* **11,** 895–905 (1999).

172. Domen, K., Horino, K., Kuramata, A. & Tanahashi, T. Analysis of polarization anisotropy along the c axis in the photoluminescence of wurtzite GaN. *Appl. Phys. Lett.* **71,** 1996 (1997).

173. Nakamura, S. *et al.* Superbright green InGaN single-quantum-well-structure

light-emitting diodes. *Jpn. J. Appl. Phys.* **34,** L1332–L1335 (1995).

174. Ponce, F. A. & Bour, D. P. Nitride-based semiconductors for blue and green light-emitting devices. *Nature* **386,** 351–359 (1997).

175. Strite, S. GaN, AlN, and InN: A review. *J. Vac. Sci. Technol. B Microelectron. Nanom. Struct.* **10,** 1237 (1992).

176. Shen, H. *et al.* Biaxial and uniaxial stress in gallium arsenide on silicon: A linear polarized photoluminescence study. *J. Appl. Phys.* **68,** 369–371 (1990).

177. Sun, Y. J., Brandt, O., Ramsteiner, M., Grahn, H. T. & Ploog, K. H. Polarization anisotropy of the photoluminescence of M-plane (In,Ga)N/GaN multiple quantum wells. *Appl. Phys. Lett.* **82,** 3850–3852 (2003).

178. Cao, L. *et al.* Engineering light absorption in semiconductor nanowire devices. *Nat. Mater.* **8,** 643–647 (2009).

179. Persano, A. *et al.* Polarization anisotropy of individual core/shell GaAs/AlGaAs nanowires by photocurrent spectroscopy. *Appl. Phys. Lett.* **98,** 153106 (2011).

180. Staleva, H. *et al.* Coupling to light, and transport and dissipation of energy in silver nanowires. *Phys. Chem. Chem. Phys.* **11,** 5889 (2009).

181. Seo, M. A. *et al.* Understanding ultrafast carrier dynamics in single quasi-one-dimensional Si nanowires. *Appl. Phys. Lett.* **100,** 071104 (2012).

182. Hashimoto, Y., Murakami, Y., Maruyama, S. & Kono, J. Anisotropic decay dynamics of photoexcited aligned carbon nanotube bundles. *Phys. Rev. B - Condens. Matter Mater. Phys.* **75,** 245408 (2007).

183. Parkinson, P. *et al.* Chromophores in molecular nanorings: When is a ring a ring? *J. Phys. Chem. Lett.* **5,** 4356–4361 (2014).

184. Schalk, O. & Hockett, P. Rotational dephasing of symmetric top molecules: Analytic expressions and applications. *Chem. Phys. Lett.* **517,** 237–241 (2011).

185. Sheng, C.-X., Tong, M., Singh, S. & Vardeny, Z. V. Experimental determination of the charge/neutral branching ratio η in the photoexcitation of π-conjugated polymers by broadband ultrafast spec. *Phys. Rev. B* **75,** 085206 (2007).

186. Vardeny, Z. V. & Frolov, S. *Ultrafast Optical Probes of Excited States in Conducting Polymers*. *Ultrafast Process. Spectrosc.* (Springer US, 1996).

187. Westenhoff, S. *et al.* Exciton migration in a polythiophene: Probing the spatial and energy domain by line-dipole Förster-type energy transfer. *J. Chem. Phys.* **122,** 094903 (2005).

188. Iakoubovskii, K., Hertogen, P. W. & Adriaenssens, G. J. Photoinduced anisotropy and polarization memory of the photoluminescence in germanium sulfide glasses. *J. Non. Cryst. Solids* **240,** 237–241 (1998).

189. Pastrnak, J. & Vedam, K. Optical anisotropy of silicon single crystals. *Phys. Rev. B* **3,** 2567–2571 (1971).

190. Yu, P. Y. & Cardona, M. Spatial dispersion in the dielectric constant of GaAs. *Solid State Commun.* **9,** 1421–1424 (1971).

191. Burnett, J., Levine, Z. & Shirley, E. Intrinsic birefringence in calcium fluoride and barium fluoride. *Phys. Rev. B* **64,** 241102 (2001).

192. Meier, F. & Zakharchenya, B. *Optical Orientation*. (North-Holland Physics Publishing, 1984).

193. Portella, M. T., Bigot, J. -Y., Schoenlein, R. W., Cunningham, J. E. & Shank, C. V. k-space carrier dynamics in GaAs. *Appl. Phys. Lett.* **60,** 2123–2125 (1992).

194. Oudar, J. L. *et al.* Femtosecond Orientational Relaxation of Photoexcited Carriers in GaAs. *Phys. Rev. Lett.* **53,** 2060–2060 (1984).

195. Bhattacharjee. Polarization of hot-electron photoluminescence in GaAs-type semiconductors for recombination on a shallow acceptor. *Phys. Rev. B. Condens. Matter* **34,** 8550–8554 (1986).

196. Zakharchenya, B. P., Mirlin, D. N., Perel', V. I. & Reshina, I. I. Spectrum and polarization of hot-electron photoluminescence in semiconductors. *Sov. Phys. Uspekhi* **25,** 143–166 (1982).

197. Giovanni, D. *et al.* Highly Spin-Polarized Carrier Dynamics and Ultralarge Photoinduced Magnetization in CH3NH3PbI3 Perovskite Thin Films. *Nano Lett.* **15,** 1553–1558 (2015).

198. Sheng, C. *et al.* Exciton versus Free Carrier Photogeneration in Organometal Trihalide Perovskites Probed by Broadband Ultrafast Polarization Memory Dynamics. *Phys. Rev. Lett.* **114,** 116601 (2015).

199. Zhai, Y., Sheng, C. X., Zhang, C. & Vardeny, Z. V. Ultrafast Spectroscopy of Photoexcitations in Organometal Trihalide Perovskites. *Adv. Funct. Mater.* **26,** 1617–1627 (2016).

200. Fraas, L. *History of Solar Cell Development*. *Low-Cost Sol. Electr. Power* (Springer International Publishing, 2014).

201. Green, M. A. Photovoltaics: Coming of Age. *Photovolt. Spec. Conf. 1990., Conf. Rec. Twenty First IEEE* **1,** 1–8 vol.1 (1990).

202. Hook, J. . & Hall, H. . *Solid State Physics*. (John Wiley & Sons, 1994).

203. Schubert, E. F. *Light-Emitting Diodes*. (2006).

204. Denbaars, S. P. *et al.* Development of gallium-nitride-based light-emitting diodes (LEDs) and laser diodes for energy-efficient lighting and displays. *Acta Mater.* **61,** (2013).

205. Rupprecht, H., Woodall, J. M., Konnerth, K. & Pettit, D. G. EFFICIENT ELECTROLUMINESCENCE FROM GaAs DIODES AT 300°K. *Appl. Phys. Lett.* **9,** 221–223 (1966).

206. Palik, E. D. *Handbook of Optical Constants of Solids*. (Academic Press, Orlando, 1985).

207. Sinzinger, S. & Jahns, J. *Microoptics*. (John Wiley & Sons, 2006).

208. Koh, T. W., Spechler, J. A., Lee, K. M., Arnold, C. B. & Rand, B. P. Enhanced Outcoupling in Organic Light-Emitting Diodes via a High-Index Contrast Scattering Layer. *ACS Photonics* **2,** 1366–1372 (2015).

209. Dupont, E., Liu, H. C., Buchanan, M., Chiu, S. & Gao, M. Efficient GaAs light-emitting diodes by photon recycling. *Appl. Phys. Lett.* **76,** 4 (2000).

210. Dumke, W. P. Spontaneous radiative recombination in semiconductors. *Phys. Rev.* **105,** 139–144 (1957).

211. Eperon, G. E., Burlakov, V. M., Docampo, P., Goriely, A. & Snaith, H. J. Morphological control for high performance, solution-processed planar heterojunction perovskite solar cells. *Adv. Funct. Mater.* **24,** 151–157 (2014).

212. Zhang, W. *et al.* Ultrasmooth organic–inorganic perovskite thin-film formation and crystallization for efficient planar heterojunction solar cells. *Nat. Commun.* **6,**

6142 (2015).

213. Davis, N. J. L. K. *et al.* Photon Reabsorption in Mixed $CsPbCl_3$:$CsPbI_3$ Perovskite Nanocrystal Films for Light-Emitting Diodes. *J. Phys. Chem. C. Nanomater. Interfaces* **121,** 3790–3796 (2017).

214. Li, G. *et al.* Highly Efficient Perovskite Nanocrystal Light-Emitting Diodes Enabled by a Universal Crosslinking Method. *Adv. Mater.* **28,** 3528–3534 (2016).

215. Philippe, B. *et al.* Chemical Distribution of Multiple Cation (Rb+, Cs+, MA+, and FA+) Perovskite Materials by Photoelectron Spectroscopy. *Chem. Mater.* **29,** 3589–3596 (2017).

216. Watt, I. M. *The principles and practice of electron microscopy*. (Cambridge University Press, 1997).

217. Goldstein, J. I. & Yakowitz, H. *Practical scanning electron microscopy: electron and ion microprobe analysis*. (Plenum Press, 1979).

218. Smith, E. & Dent, G. *Modern Raman Sectroscopy - A Practical Approach*. (J. Wiley, 2005).

219. Maes, G. Handbook of Raman Spectroscopy. From the Research Laboratory to the Process Line. *Spectrochim. Acta Part A Mol. Biomol. Spectrosc.* **59,** 211 (2003).

220. Senanayak, S. P. *et al.* Understanding charge transport in lead iodide perovskite thin-film field-effect transistors. *Sci. Adv.* **3,** e1601935 (2017).

221. Woolfson, M. M. *An introduction to X-ray crystallography*. (Cambridge University Press, 1997).

222. Lee, M. *X-ray diffraction for materials research: from fundamentals to applications*. (Apple Academic Press, 2016).

223. Seeck, O. H. & Murphy, B. *X-Ray Diffraction: Modern Experimental Techniques. J. Chem. Inf. Model.* **53,** (Pan Stanford Publishing, 2015).

224. *Agilent 8453 UV-visible Spectroscopy System, Service Manual*. (Agilent Technologies, 2000).

225. Owen, T. *Fundamentals of UV-visible spectroscopy*. (Hewlett-Packard, 1996).

226. Wahl, M. Time-Correlated Single Photon Counting. *PicoQuant GmbH Tech.*

Note (2014).

227. O'Connor, D. V. & Phillips, D. *Time-Correlated Single Photon Counting*. *Time-Correlated Single Phot. Count.* (1984).

228. ANDOR. ANDOR Intensified CDD Cameras, the technology behind ICCDs. *ANDOR Learn. Cent.* at <http://www.andor.com/learning-academy/intensified-ccd-cameras-the-technology-behind-iccds>

229. Gomez, F. V. Intensified cameras handle demanding applications. *Laser Focus World* **30,** (1994).

230. Frenkel, A., Sartor, M. A. & Wlodawski, M. S. Photon-noise-limited operation of intensified CCD cameras. *Appl. Opt.* **36,** (1997).

231. Manzoni, C. & Cerullo, G. Design criteria for ultrafast optical parametric amplifiers. *J. Opt.* **18,** 103501 (2016).

232. Cerullo, G. *et al.* in *Ultrafast Phenom. Xi* **63,** 49–53 (Springer, Berlin, Heidelberg, 1998).

233. Cirmi, G. *et al.* Few-optical-cycle pulses in the near-infrared from a noncollinear optical parametric amplifier. *Opt. Lett.* **32,** 2396–8 (2007).

234. Bowman Pilkington, S., Roberson, S. D. & Pellegrino, P. M. Analysis of continuum generation in bulk materials with a femtosecond Ti:Sapph laser. in (Fountain, A. W.) 98240Z (2016).

235. Sai Santosh Kumar, R. *Nonlinear Interactions of femtosecond pulses with transparent media:Third order nonlinear optical phenomenon in glasses, crystals and organic molecules*. (LAP Lambert Academic Publishing, 2011).

236. Brida, D. *et al.* Few-optical-cycle pulses tunable from the visible to the mid-infrared by optical parametric amplifiers. *J. Opt.* **12,** 013001 (2010).

237. Wilson, M. Ultrafast Triplet Generation in Organic Semiconductors. (2012).

238. Motta, C. *et al.* Revealing the role of organic cations in hybrid halide perovskites CH3NH3PbI3. *Nat. Commun.* **6,** (2014).

239. Zhu, X.-Y. & Podzorov, V. Charge Carriers in Hybrid Organic–Inorganic Lead Halide Perovskites Might Be Protected as Large Polarons. *J. Phys. Chem. Lett.* **6,** 4758–4761 (2015).

240. Miyata, K. *et al.* Large polarons in lead halide perovskites. *Sci. Adv.* **3,** e1701217 (2017).

241. Wu, X. *et al.* Light-induced picosecond rotational disordering of the inorganic sublattice in hybrid perovskites. *Sci. Adv.* **3,** e1602388 (2017).

242. Zhu, H. *et al.* Screening in crystalline liquids protects energetic carriers in hybrid perovskites. *Science.* **353,** 1409–1413 (2016).

243. Kim, M., Im, J., Freeman, A. J., Ihm, J. & Jin, H. Switchable S = 1/2 and J = 1/2 Rashba bands in ferroelectric halide perovskites. *Proc. Natl. Acad. Sci.* **111,** 6900–6904 (2014).

244. Kepenekian, M. & Even, J. Rashba and Dresselhaus Couplings in Halide Perovskites: Accomplishments and Opportunities for Spintronics and Spin-Orbitronics. *J. Phys. Chem. Lett.* **8,** 3362–3370 (2017).

245. Isarov, M. *et al.* Rashba effect in a single colloidal CsPbBr3 perovskite nanocrystal detected by magneto-optical measurements. *Nano Lett.* **17,** 5020–5026 (2017).

246. Azarhoosh, P., McKechnie, S., Frost, J. M., Walsh, A. & Van Schilfgaarde, M. Research Update: Relativistic origin of slow electron-hole recombination in hybrid halide perovskite solar cells. *APL Mater.* **4,** (2016).

247. Chen, Q. *et al.* The optoelectronic role of chlorine in CH3NH3PbI3(Cl)-based perovskite solar cells. *Nat. Commun.* **6,** 7269 (2015).

248. Tan, H.-S., Piletic, I. R. & Fayer, M. D. Polarization selective spectroscopy experiments: methodology and pitfalls. *J. Opt. Soc. Am. B* **22,** 2009 (2005).

249. Kawai, H., Giorgi, G., Marini, A. & Yamashita, K. The mechanism of slow hot-hole cooling in lead-iodide perovskite: First-principles calculation on carrier lifetime from electron-phonon interaction. *Nano Lett.* **15,** 3103–3108 (2015).

250. Mattoni, A., Filippetti, A., Saba, M. I. & Delugas, P. Methylammonium Rotational Dynamics in Lead Halide Perovskite by Classical Molecular Dynamics: The Role of Temperature. *J. Phys. Chem. C* **119,** 17421–17428 (2015).

251. Filippetti, A., Mattoni, A., Caddeo, C., Saba, M. I. & Delugas, P. Low electron-

polar optical phonon scattering as a fundamental aspect of carrier mobility in methylammonium lead halide CH 3 NH 3 PbI 3 perovskites. *Phys. Chem. Chem. Phys.* **18,** 15352–15362 (2016).

252. Rivett, J. P. H. J. P. H., Richter, J. M. J. M., Price, M. B. M. B., Credgington, D. & Deschler, F. Carrier-phonon interactions in hybrid halide perovskites probed with ultrafast anisotropy studies. in *Proc. SPIE - Int. Soc. Opt. Eng.* (Bakulin, A. A., Lovrincic, R. & Banerji, N.) **9923,** 99231E (2016).

253. Winfield, J. M., Donley, C. L. & Kim, J. S. Anisotropic optical constants of electroluminescent conjugated polymer thin films determined by variable-angle spectroscopic ellipsometry. *J. Appl. Phys.* **102,** 063505 (2007).

254. Ramsdale, C. M. & Greenham, N. C. Ellipsometric determination of anisotropic optical constants in electroluminescent conjugated polymers. *Adv. Mater.* **14,** 212–215 (2002).

255. Chang, M. H., Hoffmann, M., Anderson, H. L. & Herz, L. M. Dynamics of excited-state conformational relaxation and electronic delocalization in conjugated porphyrin oligomers. *J. Am. Chem. Soc.* **130,** 10171–10178 (2008).

256. Chang, M. H., Frampton, M. J., Anderson, H. L. & Herz, L. M. Intermolecular interaction effects on the ultrafast depolarization of the optical emission from conjugated polymers. *Phys. Rev. Lett.* **98,** 027402 (2007).

257. Quarti, C., Mosconi, E. & De Angelis, F. Structural and electronic properties of organo-halide hybrid perovskites from ab initio molecular dynamics. *Phys. Chem. Chem. Phys.* **17,** 9394–9409 (2015).

258. Frost, J. M., Whalley, L. D. & Walsh, A. Slow Cooling of Hot Polarons in Halide Perovskite Solar Cells. *ACS Energy Lett.* **2,** 2647–2652 (2017).

259. Correa-Baena, J. P. *et al.* Unbroken Perovskite: Interplay of Morphology, Electro-optical Properties, and Ionic Movement. *Adv. Mater.* **28,** 5031–5037 (2016).

260. Tauc, J., Grigorovici, R. & Vancu, A. Optical Properties and Electronic Structure of Amorphous Germanium. *Phys. status solidi* **15,** 627–637 (1966).

261. Crothers, T. W. *et al.* Photon Re-Absorption Masks Intrinsic Bimolecular Charge-Carrier Recombination in CH3NH3PbI3 Perovskite. *Nano Lett.*

acs.nanolett.7b02834 (2017).

262. Wright, A. D. *et al.* Band-Tail Recombination in Hybrid Lead Iodide Perovskite. *Adv. Funct. Mater.* **27,** 1700860 (2017).

263. Saba, M. *et al.* Correlated electron–hole plasma in organometal perovskites. *Nat. Commun.* **5,** 5049 (2014).

264. Cadelano, M. *et al.* in *Perovskite Mater. - Synth. Characterisation, Prop. Appl.* (InTech, 2016). doi:10.5772/61282

265. Rehman, W. *et al.* Photovoltaic mixed-cation lead mixed-halide perovskites: links between crystallinity, photo-stability and electronic properties. *Energy Environ. Sci.* **10,** 361–369 (2017).

266. Staub, F., Kirchartz, T., Bittkau, K. & Rau, U. Manipulating the Net Radiative Recombination Rate in Lead Halide Perovskite Films by Modification of Light Outcoupling. *J. Phys. Chem. Lett.* **8,** 5084–5090 (2017).

267. Anusca, I. *et al.* Dielectric Response: Answer to Many Questions in the Methylammonium Lead Halide Solar Cell Absorbers. *Adv. Energy Mater.* **7,** 1700600 (2017).

268. Capitani, F. *et al.* High-pressure behavior of methylammonium lead iodide (MAPbI3) hybrid perovskite. *J. Appl. Phys.* **119,** 185901 (2016).

269. Sadhanala, A. *et al.* Preparation of Single-Phase Films of CH3NH3Pb(I(1–x)Br(x))3 with Sharp Optical Band Edges. *J. Phys. Chem. Lett.* **5,** 2501–2505 (2014).

270. Quarti, C. *et al.* The raman spectrum of the CH3NH3PbI3 hybrid perovskite: Interplay of theory and experiment. *J. Phys. Chem. Lett.* **5,** 279–284 (2014).

271. Yadav, P. *et al.* The Role of Rubidium in Multiple-Cation-Based High-Efficiency Perovskite Solar Cells. *Adv. Mater.* 1701077 (2017).

272. Cho, H. *et al.* Overcoming the electroluminescence efficiency limitations of perovskite light-emitting diodes. *Science.* **350,** 1222–1225 (2015).

273. Kim, Y. H. *et al.* Multicolored organic/inorganic hybrid perovskite light-emitting diodes. *Adv. Mater.* **27,** 1248–1254 (2015).

274. Xiao, Z. *et al.* Efficient perovskite light-emitting diodes featuring nanometre-

sized crystallites. *Nat. Photonics* **11,** 108–115 (2017).

275. Zhang, S. *et al.* Efficient Red Perovskite Light-Emitting Diodes Based on Solution-Processed Multiple Quantum Wells. *Adv. Mater.* **29,** 1606600 (2017).

276. Zhang, L. *et al.* Ultra-bright and highly efficient inorganic based perovskite light-emitting diodes. *Nat. Commun.* **8,** 15640 (2017).

277. Bekenstein, Y., Koscher, B. A., Eaton, S. W., Yang, P. & Alivisatos, A. P. Highly Luminescent Colloidal Nanoplates of Perovskite Cesium Lead Halide and Their Oriented Assemblies. *J. Am. Chem. Soc.* **137,** 16008–16011 (2015).

278. Tsai, H. *et al.* High-efficiency two-dimensional Ruddlesden–Popper perovskite solar cells. *Nature* **536,** 312–316 (2016).